Title
Collisionless Energy and Momentum Coupling of a High-Beta Expansion to an Ambient Plasma

Author
Bonde, Jeffrey

Publication Date
2016

Peer reviewed|Thesis/dissertation

UNIVERSITY OF CALIFORNIA
Los Angeles

Collisionless Energy and Momentum Coupling of a High-Beta Expansion to an Ambient Plasma

A dissertation submitted in partial satisfaction of the
requirements for the degree Doctor of Philosophy
in Physics

by

Jeffrey David Bonde

2016

ABSTRACT OF THE DISSERTATION

Collisionless Energy and Momentum Coupling of a
High-Beta Expansion to an Ambient Plasma

by

Jeffrey David Bonde
Doctor of Philosophy in Physics
University of California, Los Angeles, 2016
Professor Walter N. Gekelman, Chair

Magnetized plasma expansions from explosive phenomena often have characteristically large ratios of kinetic ram pressure to the ambient magnetic field pressure, $\beta \gg 1$. In the presence of a tenuous, ambient plasma, collisions are incapable of transferring much energy due to the high relative velocities. These expansions, however, generate large magnetic field variations, $\Delta B/B \sim 1$, in the form of a diamagnetic cavity as well as potentially large electric fields.

A high-β expansion was created using a laser-produced plasma that expanded, $v_{exp} = 1.28 \times 10^7$ cm/s, $\beta \sim 10^6$, into a uniform, magnetized background plasma. The processes that are capable of transferring energy and momentum from the high-β expansion to the ambient plasma without collisions were explored. The combination of a magnetic probe and a novel emissive probe yielded measurements of the total electromagnetic field in three-dimensions. These constituted the first measurements of the total electric field in such an environment. The electrostatic field structure comprised the predicted inward field of a diamagnetic cavity as well as previously unobserved features including an outward field associated with a magnetic field compression and

an intense electrostatic pulse preceding the LPP. All these components were stronger than the largest observed induced electric field from Faraday's law. Direct measurements of argon ion velocities moving through these fields were made with a planar, laser-induced fluorescence diagnostic which showed ions being pulled inward against the expansion direction. Orbit solvers show that the characteristic velocity observed, $v_r = -3 \times 10^5$ cm/s, is consistent with the measured fields. The inward electrostatic field exhibited a linear variation with the magnetic field while the outward field and pulse exhibited at most a weak dependence. No significant differences in the fields were observed between helium and argon background plasmas. A qualitative model to describe the evolution of the high-β expansion in the context of weak coupling was developed. The model and the experimental field structure yielded important scaling relations for similar expansions and a qualitative extrapolation to the strong-coupling case.

The dissertation of Jeffrey David Bonde is approved.

Vassilis Angelopoulos

Troy A. Carter

Christoph Niemann

Stephen Vincena

Walter N. Gekelman, Committee Chair

University of California, Los Angeles

2016

To those who gave me respite when the world seemed to loom and time exposed its bleak face:

"Und es sei nochmals gesagt, wir wohnen [in unserem Bau] als ziemlich ahnungslose und ziemlich bequem gewordene Gäste, wir wollen nichts mehr wissen von den ungeheuren Menschenopfern, über welchen unsere Grundmauern errichtet sind, nichts von den leidvollen Erfahrungen, deren Erben wir sind, und nichts von der Weltgeschichte, welche unseren Bau errichtet oder geduldet hat, welche uns trägt und duldet…welche aber einmal unseren Bau wieder stürzen und verschlingen wird, wie sie alles wieder stürzt und verschlingt, was sie hat wachsen lassen."

-Hermann Hesse, *Das Glasperlenspiel*

"Dans ses écrits, un sage Italien
Dit que le mieux est l'ennemi du bien ;
Non qu'on ne puisse augmenter en prudence,
En bonté d'âme, en talents, en science ;
Cherchons le mieux sur ces chapitres-là ;
Partout ailleurs évitons la chimère,
Dans son état, heureux qui peut se plaire."

-Voltaire, "La Bégueule"

But mostly, to Jay. You gave me courage and dreams.

TABLE OF CONTENTS

List of Figures

List of Tables

Glossary of Symbols

Quantity	Definition	Notes
τ, t'	Normalized time variables	*
$\tilde{R}, R'$	Normalized radial positions	*
n	Density of particles	~
m	Mass of particle	~
Z	Charge state	~
$\langle Z \rangle$	Average charge of a distribution of ions	
T	Temperature	
v_T	Thermal velocity	~
V	Flow velocity	*,x
c_s, C_s	$= \sqrt{\gamma T_e / m_i}$, Sound speed	*
V_A	Alvén speed	
ω_c	$= ZeB/m$, Cyclotron frequency	~
ν_{ci}	$= \omega_c / 2\pi$	~
ω_p	$= \sqrt{Z^2 e^2 n / m\epsilon_0}$, Plasma frequency	~
ν_p	$= \omega_p / 2\pi$	~
τ_{ei}	Electron-ion collision time	
ρ_m	$= \sum_\alpha m_\alpha n_\alpha$, Mass density	
ρ_c	$= \sum_\alpha Z_\alpha e n_\alpha$, Charge density	
β_{th}	$= 2\mu_0 p_e / B_0^2 = 2\mu_0 n_e T_e / B_0^2$, Thermal beta	
M_s	$= V / C_s$, Sonic Mach number	

Quantity	Definition	Notes
M_A	$= V/V_A$, Alfvén Mach number	
ϕ	Electrostatic Potential	
B	Magnetic field	*,x
E_{st}	The irrotational component of the electric field, $\nabla \times \boldsymbol{E}_{st} = 0$ or $\boldsymbol{E}_{st} = -\nabla\phi$. Referred to as the electrostatic field.	x
E_{ind}	The solenoidal component of the electric field, $\nabla \cdot \boldsymbol{E}_{ind} = 0$ or $\boldsymbol{E}_{ind} = -\partial_t \boldsymbol{A}$. Referred to as the induced electric field.	x
E_{pol}	Translational polarization field. It is irrotational but due to the translational motion of a polarizable mass through a magnetic field, not expansion.	x
J	Current	x
j	Particle flux	
p	Pressure	
η	Classical Spitzer resistivity	
ω_0	Resonance frequency of an atomic transition	
λ_0	Resonance wavelength of an atomic transition	
σ	Atomic transition cross-section	
E_L	Laser energy pulse	
I_L	Laser intensity	
δt	Laser pulse length	
λ	Wavelength	
ν	$= c/\lambda$, Wave Frequency	
n_{cr}	$= (2\pi\nu)^2 m_e \epsilon_0 / Z^2 e^2$, Critical density of laser	

Quantity	Definition	Notes
E_{tot}	Total energy in the LPP	
N	Total number of particles in the LPP	
V_n	Velocity of LPP normal to the target surface	*,x
V_z	Velocity of LPP along the magnetic field	*,x
V_r	Velocity of LPP lateral to the target surface	*,x
V_m	$\boldsymbol{V}_m = \sum_\alpha m_\alpha n_\alpha \boldsymbol{V}_\alpha / \sum_\alpha m_\alpha n_\alpha$, Mass-weighted velocity	*,x
v_{dia}	The apparent speed of the diamagnetic cavity	
R	Radius of LPP	*
Z_0	Initial size of LPP normal to the target surface	
ϵ	$= Z_0/R_0$, Eccentricity of ellipsoidal seed plasma	
t_0	Expansion hydrodynamic time	
t_h	Generalized hydrodynamic time	
τ_D	$\partial_t R(\tau_D) = 0$, Time to peak diamagnetism	
t_m	Generalized magnetohydrodynamic time.	
t_T/ν_T	Thermal equilibration time/rate	
ρ	$= V/\omega_c$, directed Larmor radius	~
R_B	$R_0\beta^{1/3}$, Diamagnetic radius	
R_D	Radius of diamagnetic cavity at $t = \tau_D$. In weak-coupling or vacuum conditions, $R_B = R_D$.	
R_m	$= \left(\frac{3}{4\pi}\frac{m_{di}N_{di}}{m_{ai}n_{ai}}\right)^{1/3}$, Equal mass radius.	
R_q	$= \left(\frac{3}{4\pi}\frac{Z_dN_{di}}{Z_an_{ai}}\right)^{1/3}$, Equal charge radius.	

Quantity	Definition	Notes
β	$= \left(\frac{R_B}{R_0}\right)^3$, Dynamic beta of the LPP expansion, ratio of initial kinetic ram pressure to magnetic pressure.	
	α in the above definitions denotes a particle species.	
$*$	A subscript '0' attached to this quantity indicates it is taken as the initial value as opposed to being time-dependent.	
x	Vectorized quantity denoted as bold face	
~	When necessary to distinguish between these values for LPP particles and ambient particles, superscripts or subscripts 'd' for debris and 'a' for ambient are added.	

Acknowledgements

I would like to thank:

My advisor, Prof. Walter Gekelman for keeping me grounded during this project, for not mincing words when my own words and ideas strayed, and for his vast and helpful insights and advice into life and the workings of the greater plasma physics community.

Dr. Stephen Vincena for his patience in listening to my perhaps unconventional ideas, for enduring my easily excited nature when discussing physics, and for his guidance with the multitude of technologies that make the LAPD and this project function harmoniously.

Professors Troy Carter, Christoph Niemann, and Vassilis Angelopoulos for being patient committee members.

Lucky Zoltan for imparting some of his vast knowledge of and skills with vacuum systems to me.

Marvin Drandell for being able and willing to help me build what I needed for these experiments and make crucial, ad hoc changes to the 3D probe drive. Also for tolerating my use of the mill.

Dr. Patrick Pribyl for his guidance with electronics in general but mostly with those for the emissive probe.

Drs. Shreekrishna Tripathi and Bart Van Compernolle for helping tame the LAPD and their extensive and insightful physics discussions.

My fellow graduate students, for making my graduate years all the more educational and working in the office all the more enjoyable.

The US Department of Energy which funded this project.

Vita

2010 B.S. (Nuclear Science and Engineering),

B.S. (Physics), Massachusetts Institute of Technology.

2010-2016 Graduate Student Researcher, Department of Physics,

University of California, Los Angeles.

Publications

Martin, M.J., Bonde, J., Gekelman, W., and Pribyl, P., "A resistively heated CeB6 emissive probe", *Review of Scientific Instruments* **86** (5), 53507 (2015)

Bonde, J., Vincena, S., and Gekelman, W., "Electrostatic structure of a magnetized laser-produced plasma", *Physical Review E*, **92** (5), 51102 (2015)

Chapter 1 – Introduction

1.1—Introductory Remarks

Laser-produced plasma experiments have been conducted as long as there have been lasers powerful enough to ablate materials [1]. After the basic properties of these laser-produced plasmas (LPP) were characterized, focus shifted to their ability to generate energetic particle beams [2,3], fusion schemes revolving around inertial confinement [4], and pulsed laser evaporation techniques [5]. Basic plasma physics experiments have continued on at various, smaller scale facilities. On the Large Plasma Device (LaPD) at UCLA, experiments have been conducted over two decades to study the various features of magnetized LPP expansions. Some of the latest results of experiments at the LAPD show that collisionless shock conditions can be reached when the LPP is embedded in an ambient plasma [6].

A laser-induced fluorescence (LIF) diagnostic already available for use in the LaPD allows one to experimentally characterize the coupling between such a magnetized LPP expansion and an ambient argon plasma. Preliminary investigations with the LIF as well as spontaneous emission diagnostics suggested that indeed the LPP had a detectable effect on background argon ions for which the collision mean-free path was too large to explain. This prompted a series of experiments trying to explain these observations and whether they have a broader context.

This experimental dissertation is focused on the mechanisms of collisionless coupling. The parameters are such that they directly relate to a weak-coupling limit but provide a clue as to how the shock structures observed in [6] form in the strong-coupling limit. In this context, strong-coupling versus weak-coupling distinguishes whether the mechanism for energy and momentum

transfer depends on conditions of the ambient plasma or not. Thus, strong-coupling occurs when the amount of energy and momentum transferred from the high-β expansion affects how it is transferred, that is to say feedback plays a dominant role. Weak coupling on the other hand is largely independent of the characteristics of the ambient plasma. The results in the present, weak-coupling case show that the laminar electromagnetic fields of a high β expansion are strong enough to inject energy and drive flows in the ambient plasma. The fields responsible for the collisionless coupling are due to the global structure of the diamagnetic cavity that forms.

There are a number of different contexts in which diamagnetic cavities may form since plasmas are inherently diamagnetic and so not all necessarily share the same underlying physical processes. Within the context of the LPP experiments, the cavities form because of the very high β characteristics of the expanding plasma. Historically, β has been reserved by plasma physicists studying equilibrium conditions as the ratio of the thermal energy density to the magnetic field energy density. In models of magnetized LPP expansions, β is a dynamic parameter that can be defined as the ratio of (a) the *initial* electron thermal energy density to the magnetic energy density or (b) the ion kinetic energy density to the magnetic energy density. In the context of high-β expansions, there is very little difference between these two quantities as thermal energy is converted to kinetic energy on a time scale (hydrodynamic time) much shorter than the magnetic interaction time scale (cavity formation time). Confusing overlap of the two concepts of equilibrium versus dynamic parameter appear throughout the literature of magnetized LPP experiments as investigators try to explain features of a dynamic high-β expansion with low-β equilibrium models. Dense expansions of matter into a more tenuous environment are never truly in an equilibrium state. In this dissertation, the β characterizing the diamagnetic cavity and by extension the collisionless coupling will only ever mean the dynamic parameter associated with

the kinetic energy of the expansion (definition (b) above). When it is necessary to distinguish the two, the ratio of the thermal pressure and the magnetic pressure, which is a time-dependent quantity and not a characteristic parameter of an LPP, will be denoted by β_{th}.

For LPPs, β is easily in the range $10^3 - 10^8$. The relatively low magnetic fields in space mean that many explosive phenomena may easily fall into this similar range of β or, more likely, far above it. The basic model presented in Chapter 2 for the magnetized LPP, however, suggests only a lower bound on β for its applicability. This provides a broad physical context in which magnetized LPPs lie that make them extremely useful for simulating processes of astrophysical relevance such as collisionless coupling in a controlled laboratory environment.

1.2—Motivations

Strong outflows of plasmas are ubiquitous in the universe; appearing on a large range of spatial and temporal scales. An astrophysical example is an eruption from young stellar objects (YSO) [7]. The last few decades of observations of synchrotron radiation have shown that relatively strong magnetic fields ($B_0 \sim 1$ mG) exist in the immediate vicinity of and far extended from these sources [8]. These fields are relatively strong in that they are orders of magnitude larger than expected from considering simple dipole fields in vacuum and imply the presence of a magnetic interaction. Further, since typical outflow speeds are $100 - 1000$ km/s, the mean-free-paths of momentum loss to electrons of $\lambda_{mfp} = 10^8 - 10^{12}$ km or about 1 A.U. to 1/10$^{\text{th}}$ of a light-year with momentum loss to ions being even less. An explosive origin for these strong outflows would certainly qualify as a relevant, high-β expansion. Experiments on magnetized LPPs could therefore provide some insight as to how these astrophysical expansions form their jets and interact with their environment especially without significant collisional effects.

Plasma explosions are far from limited to astrophysical phenomena. In the 1960s, thermonuclear devices were detonated [9] high in the atmosphere with far reaching repercussions to communication equipment (satellites, radio towers, etc.) and even generated artificial radiation belts [10] in the magnetosphere. From data available for these experiments, the values of β were around $\beta \sim 10^{15}$. In the 1980s, chemical releases from the AMPTE [11] and CRRES [12] missions looked at dense particle transport at the magnetopause and in the magnetotail. The AMPTE release that occurred on March 21, 1985 had $\beta \sim 10^{7}$, or near that of a typical magnetized LPP experiment.

1.3—Brief Outline of Dissertation

The content of this thesis will proceed as follows. A simple and convenient model of such a very high β expansion will be presented from which properties of the diamagnetic cavity formation may be deduced as well as how collisionless momentum and energy between the expansion and an ambient plasma will occur. The experimental setup will be described which includes a somewhat standard setup for a magnetized LPP. Focus will be placed on the diagnostics which were necessary to characterize the coupling mechanism: the LIF diagnostic and a novel emissive probe for high density electric field measurements. The electromagnetic field structures and their evolution will be presented and discussed with the magnetic field, induced electric field, and electrostatic field appearing separately and in sequence. This is to allow a coherent picture of each to develop within the context of the general LPP expansion while limiting unnecessary and confusing cross-references between dynamics of the different fields. The LIF data will be presented after the fields followed by a simple particle tracer that shows the clear connection between all the experimental data. Discussion and extensions of the results to more varied conditions precede concluding remarks.

Chapter 2—The High-β Expansion Model

2.1—Introduction

There are many stages to the life of an LPP from the first particle being ionized to it becoming so diffuse as to be indistinguishable from its initially more tenuous environment. During each stage, certain physical processes will have a dominant effect on the evolution and eventual form of the LPP. Fortunately, many of them relax on time scales much faster than those of interest to this experiment. The primary assumption employed is that after many of these processes have relaxed, the bulk of the energy content is in the ion kinetic energy. The dominant processes that determine this ion energy content are connected to thermalization, isotropization, and expansive cooling of the plasma. These have characteristic relaxation time scales on the order of a generalized hydrodynamic time, t_h. If the electromagnetic fields evolve on some characteristic time scale, t_m, of the magnetic structure during which the collisionless coupling occurs, the high-β assumption is essentially that $t_m \gg t_h$. In this limit, the minutiae of the early stages of the LPP may be described by simple, bulk characteristics. As we will see, $\beta \sim (t_m/t_h)^3$. Thus the high-β model is most applicable for those expansions for which $\beta > 10^3$.

2.2—Laser-Produced Plasma Formation and Geometry

When sufficiently intense light is incident on a neutral atom, the electric field can rip off valence electrons which are then free to move in the light field. The field then energizes the electron in a process called inverse bremsstrahlung. This energy, on a relatively slower time scale, diffuses to the other particles in the system as the electrons start colliding with neutrals, ions, and other electrons. With sufficient particle density, a plasma forms in the region where the light first

started ionizing neutrals. For ns-long pulses incident on solid targets, the collisions will tend to thermalize and isotropize the plasma. The bulk parameters of this "seed" plasma can be described by semi-empirical formulae where a scaling relation is derived from theoretical arguments. The constants involved in the formulae are determined experimentally and vary significantly among target material conditions and class of light pulse. Those relevant to this experiment will be given in the Experimental Setup chapter. When the light source is removed, the roughly uniform, Maxwellian plasma is expands into its more tenuous environment.

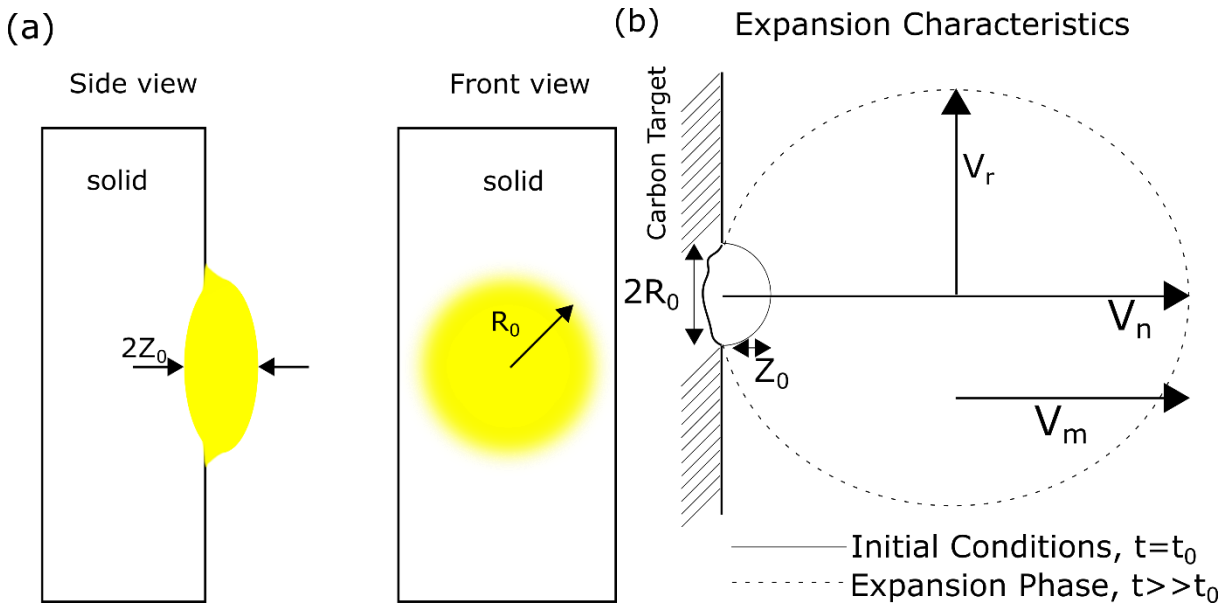

Figure 2.1: (a) The simplified geometry of the "seed' LPP on the surface of a thick, planar target. (b) Expansion geometry emphasizing the 3 essential velocities resulting from a laser-solid interaction. V_n and V_r are the peak velocities in the target-normal coordinate system and V_m is the center of mass velocity.

The initial shape of this plasma is determined by the physical size of the light pulse and how the plasma constituents reach equilibrium with the incident light pulse; the latter being affected by how far the laser can penetrate the solid and how dense the plasma becomes. Ignoring most of the fine structure, the simplest shape it can take is that of an oblate spheroid embedded on

the surface of the target. The asymmetry of the initial plasma and its subsequent evolution lead to the adoption of a cylindrical geometry (r, ϕ, z) with the $z-$direction being the target-normal. A cartoon of the initial plasma is shown in Fig. 2.1a. The minor radius of the spheroid is Z_0 aligned with the normal of the solid target surface and the major radius R_0 is the characteristic size along the tangent of the target surface.

After the light pulse shuts off, the pressure gradient of the much faster electrons trying to escape the ions forms an electric field. This electric field mediates the exchange of energy between the electrons and the ions until the ions can keep up with the electron fluid motion. The ions are left with velocities on the order of the initial sound speed while the electron energy is mostly depleted, having been transferred to the ions. This is the model put forth by Puell [13] for the LPP expansion properties and largely consistent with that groups' early experiments.

As Puell [13] notes, the model is essentially equivalent to the fluid expansion model of Nemchinov [14] for which an initial geometry such as that of Fig. 2.1a leads to an expansion geometry like that of Fig. 2.1b. The example calculations of this model are given in Appendix A, but the general description is as above with the following qualitative and quantitative aspects. The smallest dimension in the initial shape becomes the largest dimension in the final expansion geometry. The time scale over which this inversion occurs is the particular hydrodynamic time scale $t_0 = R_0/C_s (= t_h)$. For an initially oblate spheroid this results in a prolate spheroid expansion where the slow velocity is very close to the speed of sound, i.e. $t_0 \approx R_0/V_{r0}$. The ratio of V_{z0}/V_{r0} is highly dependent on the ratio R_0/Z_0 and the former increases rapidly with the latter. Inclusion of a solid surface in such a model is a non-trivial task but it is clear that any expansion off of the target will have a shifting center of mass. The Nemchinov model is with respect to the center of mass of the gas so that $V_n \approx V_{z0} + V_m$. These are the basic assumptions of the state of the LPP

which will be used as a reference point and to analyze the interaction between its constituents, the magnetic field, and an ambient plasma.

2.3—Diamagnetic Cavity

The interaction of the high-β expansion with the ambient magnetic field, hereafter denoted $\boldsymbol{B}_0$, for $t \sim t_0$ can largely be ignored as the thermal and kinetic pressures are generally far higher than that of the magnetic pressure. As the LPP expands, its thermal and kinetic energy densities drop rapidly so that eventually, the presence of $\boldsymbol{B}_0$ dominates the dynamics of the expansion. This occurs through the formation of a diamagnetic cavity.

The highly conductive, expanding plasma expels $\boldsymbol{B}_0$ from its interior and in doing so generates its own electromagnetic fields to maintain consistency with Maxwell's equations. These are the fields that are to be considered in the context of collisionless coupling between the LPP and the ions in the ambient plasma. Generation of these fields comes at the expense of the stored energy in the LPP, which for $t \gg t_0$ is in the kinetic energy of the ions. The fraction of the initial LPP energy taken up by magnetic flux removal increases with the volume of the LPP until the ion kinetic energy is expended by this process. Thus, in addition to the characteristic scale quantities of the unmagnetized expansion model, there is the time to peak diamagnetism, τ_D. The electromagnetic fields generated by the interaction of the LPP with $\boldsymbol{B}_0$ exist on this characteristic time scale which will also characteristize the collisionless coupling. Since the magnetic fields do no work on either the LPP or ambient material and the fields form coincidentally with the deceleration, understanding the mechanism of LPP-ambient interaction requires a full knowledge of the total electric field and how it forms.

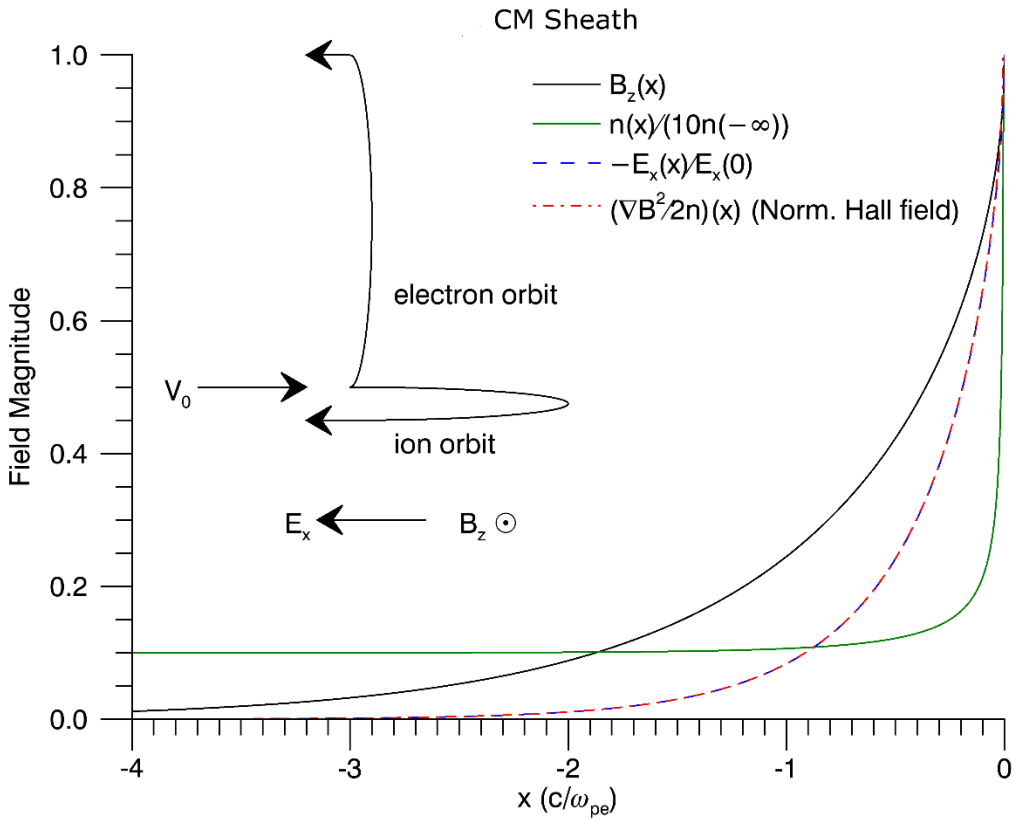

Figure 2.2: Diagram of the particle motion within a magnetic sheath separating a plasma expanding into a magnetic field. Profiles of the magnetic field, electrostatic field, density, and Hall field are as calculated by Rosenbluth [15]. The Hall field and electrostatic field are essentially identical.

The mechanism for the formation of these diamagnetic cavities from ion kinetic pressures has been encountered and elucidated numerous times through the history of plasma physics. From a particle point of view, the mechanism is quite simple and it is shown diagrammatically in Fig. 2.2. Cold ions and electrons start out moving into the sheath region, across the magnetic field with a velocity $\boldsymbol{V}_0 = \boldsymbol{V} - \boldsymbol{B}_0(\boldsymbol{V} \cdot \boldsymbol{B}_0)/B_0^2$. Since the electrons are far lighter, their trajectories are more perturbed by the magnetic field than those of the ions. This causes a space-charge field to form (opposite to the one that accelerated the ions to begin with) between the electrons and less-

magnetized ions. The orientation of this electrostatic field is such that the ions are slowed and the electrons are sped up. The electrons being more affected by the magnetic field, end up with a large portion of this energy moving in the direction perpendicular to both $\boldsymbol{B}_0$ and $\boldsymbol{V}_0$. This difference in the electron and ion motion in the direction of $\boldsymbol{V}_0 \times \boldsymbol{B}_0$ constitutes the "diamagnetic current" that expels $\boldsymbol{B}_0$. Concurrently, the expulsion produces an induced electric field from Faraday's Law which is also in the direction of $\boldsymbol{V}_0 \times \boldsymbol{B}_0$ and antiparallel to the diamagnetic current consistent with energy moving from the particles to the fields. The relative bending of the electron and ion trajectories within the combined electrostatic and magnetic field is well-approximated by $\boldsymbol{E} \times \boldsymbol{B}$ motion of the electrons alone so that the diamagnetic current is effectively equivalent to a Hall current. Finite electron temperature leads additional diamagnetism from ∇p_e drifts. Cooling of the expansion, however, means this mechanism quickly diminishes in strength relative to $\boldsymbol{E} \times \boldsymbol{B}$. The induced electric field then allows electrons to drift across the magnetic field with the ions. This model, in the collisionless limit, results in electron skin-depth scale sheaths between a vacuum magnetic field and an essentially unmagnetized plasma expanding against it.

The original derivation was partially heuristic in nature and applied to magnetic storms in Earth's magnetosphere in 1940 [16] with an improved explanation developed in 1952 [17]. The first analytic and self-consistent solution was derived by Rosenbluth in 1954 [15] within the context of pinch machines for fusion. His analytic solution was used to generate the field profiles in Fig. 2.2. An independent derivation (Rosenbluth's work was classified under Project Matterhorn) was arrived at by Dungey [18] as a model for the Earth's magnetopause. The differences between the applications of this sheath, even though all of the aforementioned descriptions are identical, has led to it being called in the stereotypically prosaic fashion of physicists as various combinations of the four names: Chapman-,Ferraro-,Rosenbluth-, Dungey-

sheath. When referring specifically to the particle picture and fields of Fig. 2.2, it will hereafter be referred to as the cold, magnetosonic (CM) sheath owing to its close relationship to the derivation of cold, magnetosonic solitons and shocks. Note that it is also identical to the more popular Harris model of magnetic sheaths [19] if one accounts for reflected particles and takes the limit of zero temperature.

The earliest applications of this sheath to high-β expansions with which this study is concerned was by Raizer [20] on the Russian side of plasma physics and Colgate [21] on the American side. Both were clearly aiming specifically at high altitude nuclear explosions although it is clear that the latter either misunderstood the mechanics of the sheath or did not consider that the sheath exists in a frame with an expanding plasma. Unfortunately, the analytic model only works for cold, collisionless plasmas in one spatial dimension. Nevertheless, it serves as a guide for the heuristics of the more tenable fluid approach.

In a single fluid picture, the electric fields are described by Ohm's law. Neglecting the electron inertial terms and ion thermal terms, Ohm's law is

$$\boldsymbol{E} = \eta \boldsymbol{J} - \boldsymbol{V} \times \boldsymbol{B} + \frac{\boldsymbol{J}}{e n_e} \times \boldsymbol{B} - \frac{\nabla p_e}{e n_e}, \tag{2.1}$$

where η is the classical Spitzer resistivity, $\boldsymbol{J}$ is the total current, p_e the electron pressure, n_e the electron density, $\boldsymbol{B}$ the total magnetic field, and $\boldsymbol{V}$ represents the mass-weighted velocity which will be taken as essentially that of the ions. For an initially hot plasma, the first term of the RHS is quite small. It will become important later, especially for $t > \tau_D$, but it is not necessary for a general description of the electric field and its contribution must be treated more cautiously than it is worth owing to its strong time dependence and sensitivity on T_e. For very similar reasons, the pressure term is also large initially but its magnitude falls with time as t^{-p}, $p \in [2,3]$ as most of

the electron thermal energy is transferred to the ions as kinetic energy [1]. The diamagnetic cavity results in a "re-thermalization" of the electrons [22] late in time and the resistive term plays an intimate role, but as will be shown by the data, the pressure term plays even less of a role than the resistive term. Thus the Lorentz and Hall fields represent the primary terms constituting the electric field.

Using the geometry of Fig. 2.1 and the CM sheath of Fig. 2.2, the magnitude of these terms can be directly related to the bulk characteristics of the expanding LPP. The CM sheath shows that as the ions move through the electromagnetic field, the motion is essentially ballistic along their initial trajectories. In the cylindrical geometry of Fig. 2.1 with the magnetic field, $\boldsymbol{B}_0 = B_0\boldsymbol{e}_z$, along the surface normal, $\boldsymbol{V}(t) \approx V_r\boldsymbol{e}_r + V_n\boldsymbol{e}_z$. Similarly with the current generated by the difference between electron and ion motion, $\boldsymbol{J} \approx J_\phi\boldsymbol{e}_\phi$. This means that the Lorentz term is primarily in the azimuthal direction and the Hall term is likewise mostly in the radial direction. This geometry means that respectively, the Lorentz term and the Hall term are the induced electric field and the electrostatic field. That is, if one writes

$$\boldsymbol{E} = -\nabla\phi - \partial_t\boldsymbol{A},$$

then in the Coulomb gauge, one has

$$\boldsymbol{E}_{\mathrm{st}} = -\nabla\phi = \frac{\boldsymbol{J}}{en_e} \times \boldsymbol{B} \text{ and } \boldsymbol{E}_{ind} = -\partial_t\boldsymbol{A} = -\boldsymbol{V} \times \boldsymbol{B}$$

just as in the CM sheath. There is also the correspondence to the CM sheath that the electrostatic field is responsible for slowing down the LPP by removing energy from the ions. The induced electric field stretches the electron orbit and their drift motion so that they move across the

magnetic field at the same speed as the ions. To relate the electric fields to the plasma motion, take the plasma momentum equation, assuming a cold plasma,

$$\rho_m d_t \boldsymbol{V} = \rho_c \boldsymbol{E} + \boldsymbol{J} \times \boldsymbol{B},$$

where ρ_m is the mass density ρ_c is the charge density. Using the above expressions for the total electric field to eliminate $\boldsymbol{J} \times \boldsymbol{B}$,

$$\rho_m d_t \boldsymbol{V} = Z_d e n_i \boldsymbol{E} + e n_e \boldsymbol{V} \times \boldsymbol{B} \approx Z_d e n_i \boldsymbol{E}_{st},$$

where n_i is the ion density and the approximation is due to quasi-neutrality, $Z_d n_i \approx n_e$. If we take $R(t)$ as a dynamic, characteristic radius of the LPP across the magnetic field, the velocity can be replaced by $V_r = \partial_t R$ and likewise the acceleration is $\partial_t^2 R(t)$. The corresponding characteristic magnitudes of the induced electric fields and electrostatic fields can then be written as

$$\boldsymbol{E}_{st} = \frac{m_{di}}{Z_d e} \partial_t^2 R \text{ and } \boldsymbol{E}_{ind} = -\partial_t R B_z.$$

where m_{di} is the mass of an ion in the LPP, Z_d its charge, and $\rho_m \approx m_{di} n_i$. These forms represent the dominant components of the electric field and reflect the fields necessary to extract the energy from the ions ($\boldsymbol{E}_{st}$) and to keep the diamagnetic cavity and LPP expanding across $\boldsymbol{B}_0$ ($\boldsymbol{E}_{ind}$) and which are both characterized in terms of one dynamic parameter, $R(t)$. This a very common method of analysis in fluid expansions and a convenient model for $R(t)$ comes from the fluid model of gaseous bubble dynamics.

Analysis of gaseous bubbles goes back to the mid-19th century but was given its standard form by Rayleigh in 1917 [23] and eventually leading to what is now known as the Rayleigh-Plesset equation. It finds use every day in the analysis of steam bubbles, cavitation in aquatic propulsion, and contained explosions. The main assumption of the model, which will hereafter be

referred to as the Rayleigh model, is that the velocity field can be written in a self-similar manner normalized to the characteristic dimension $R(t)$, specifically,

$$V_r(r,t) = V_r(t) f\left(\frac{r}{R(t)}\right) \text{ and } V_r(t) = \partial_t R$$

as was used above for the electric fields. This is the relationship that is used in Nemchinov 14] and in the Appendices with $f(x) = x$. Note that this is simply the free expansion limit found in LPP simulations [24] and, from the continuity equation, is necessary to get the relationship $n_e \sim t^{-3}$ which is well-established by unmagnetized LPP expansion experiments. Rayleigh's next step is to simply consider the dynamic energy balance.

To simplify the matter, the initial condition at $t = t_0$ will be that the thermal energy of the electrons has already been expended to accelerate the ions. This is a good approximation since $t \approx t_0$ is of little consequence to the diamagnetic cavity for high-β expansions. Energy balance for a spherical expulsion of the magnetic field gives

$$E_{tot} = \frac{C}{2} N_{di} m_{di} (\partial_t R)^2 + D \frac{4\pi (R^3 - R_0^3)}{3} \frac{B_z^2}{2\mu_0},$$

where N_{di} is the total number of ions in the expansion, B_z is the magnitude of the magnetic field at $r = R(t)$, and C and D are constant coefficients characterizing the energy profile in the LPP. For the classical superconductor, $B_z = 3B_0/2$, and for a cylindrically symmetric expansion with $f(x) = x$, $C = 2/5$. The exact value of D is difficult to pin down for a realistic sheath—the planar CM sheath with full expulsion, $D \approx 1$, is the largest possible value. The simple substitution of magnetic pressure for fluid pressure in Rayleigh's fluid model, which results in a parabolic pressure profile, leads to $D = 1/2$. With the further assumptions that $E_{tot}, B_z =$const, the problem leads to a differential equation in $R(t)$. The problem of energy balance is often approached without

including R_0, for example in [25], but singularities abound when treating R dynamically that are very unrealistic and lose a lot of their physical significance. Furthermore, similarity theory [26] suggests that taking such an inherent, dimensional parameter to 0 when what is meant is $R/R_0 \gg 1$ often leads to erroneous results.

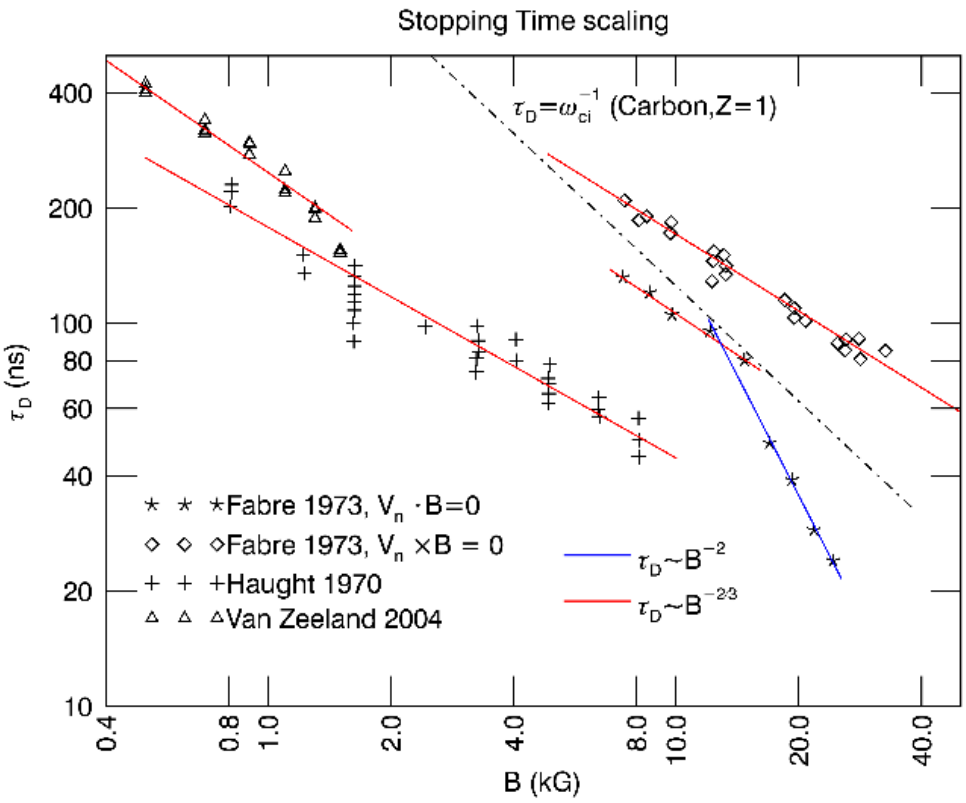

Figure 2.3: Variation of τ_D with magnetic field from [27], [28], and [29]. All experiments used carbon targets and the curve $\tau_D \omega_{ci} = 1$ is overlayed using $Z = 1$.

The problem is non-dimensionalized using the variables $\tau \equiv t/t_0$ and $\tilde{R} \equiv r/R_0$ and kinetic beta

$$\beta \equiv \frac{\frac{3C}{2}\frac{N_{di}m_{di}V_{r0}^2}{4\pi R_0^3}}{D\frac{B_z^2}{2\mu_0}} = \frac{\text{initial directed radial energy density}}{\text{magnetic field energy density}}.$$

The resulting differential equation in Rayleigh's model is,

$$d_\tau \tilde{R} = \sqrt{1 - \frac{1}{\beta}(\tilde{R}^3 - 1)}. \tag{2.2}$$

Note that for $\beta \gg 1$, the further transformations $\tau \to \beta^{1/3}\tau$ and $\tilde{R} \to \beta^{1/3}\tilde{R}$ remove the dependence on the parameter so that the solution in such normalized variables is independent of all physical parameters.

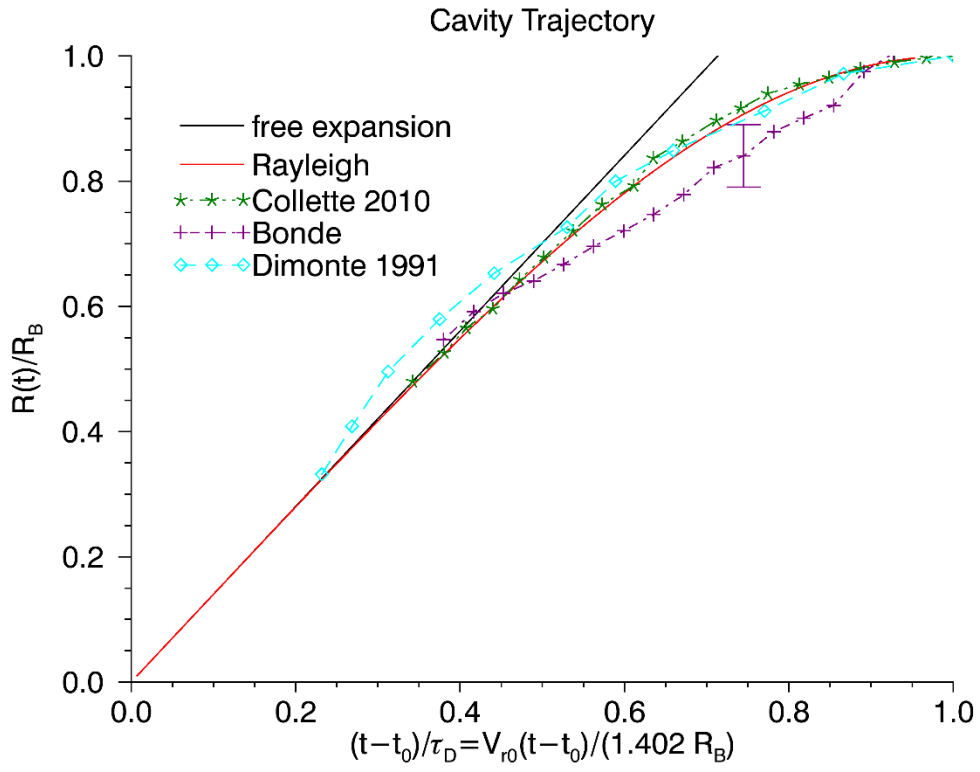

Figure 2.4: Solution to the differential equation for $R(t)$ in normalized, dimensionless variables (Rayleigh). Also shown is the free expansion line and trajectories across the magnetic field from 3 experiments. References in the text.

In the limit that $\beta \gg 1$, β has a simple meaning: if $\tilde{R}^3 = \beta$ then $t = \tau_D$, peak diamagnetism has been reached, and the LPP stops expanding across the magnetic field. The characteristic dimension associated with the characteristic time τ_D is $R_B \equiv \beta^{1/3} R_0$. Most relevant experiments have $\beta > 10^3$. If one takes $1/(1+\beta) \to 0$, the differential equation can be integrated exactly up to time $t = \tau_D$ for which

$$\tau_D = t_0 + \frac{t_0}{3}\beta^{1/3}\frac{\Gamma\left(\frac{1}{3}\right)\Gamma\left(\frac{1}{2}\right)}{\Gamma\left(\frac{5}{6}\right)} \approx 1.402\frac{R_B}{V_{r0}} \sim \frac{1}{V_{r0}^{1/3}B_0^{2/3}}.$$

The variation with magnetic field represented by this equation has been widely confirmed with the broadest variations in B given by Fabre [27], Haught [28], and Van Zeeland [29] shown in Fig. 2.3. Fabre did both cross-field and parallel expansion but noted coupling of the laser in the parallel expansion was noticeably reduced. This is the cause of the offset between their two curves for τ_D. The discrepancy Fabre noted where $\tau_D \sim B_0^{-2}$ occurred for $\tau_D \to t_0$ and was attributed to the extreme losses along the rather intense magnetic fields. In their unusual scaling case, for which best guesses have $\beta < 10^4$, the high β expansion assumption is probably not valid.

The solution to the equation for $R(t)$ and $\beta \gg 1$ is shown in solid red Fig. 2.4. The axis have been normalized such that the solution curve is independent of β. Also shown is the free expansion model in solid black and 3 sets of experimental data. Of the 5 interdependent quantities, t_0, V_{r0}, R_0, τ_D, and R_B, two of the first three must be known and one of the last two in order to properly normalize the variables and the curve. Since very few magnetized LPP experiments have framed their data in terms of these variables, very few data sets are complete and reliable enough to extract the curve. The data of Dimonte [30] (Fig. 3a therein), Collette [31] (Fig. 3.13a therein), and Bonde (this dissertation's magnetic field data) are all complete enough to get the curve. They

show that despite the low level of detail of this model, the curve $R(t)$ is quite representative of a variety of plasma experiments which used different target materials (C, CH2, Al), different laser energies (1 J, $100 - 200$ J) and magnetic fields (several hundred Gauss, several Tesla).

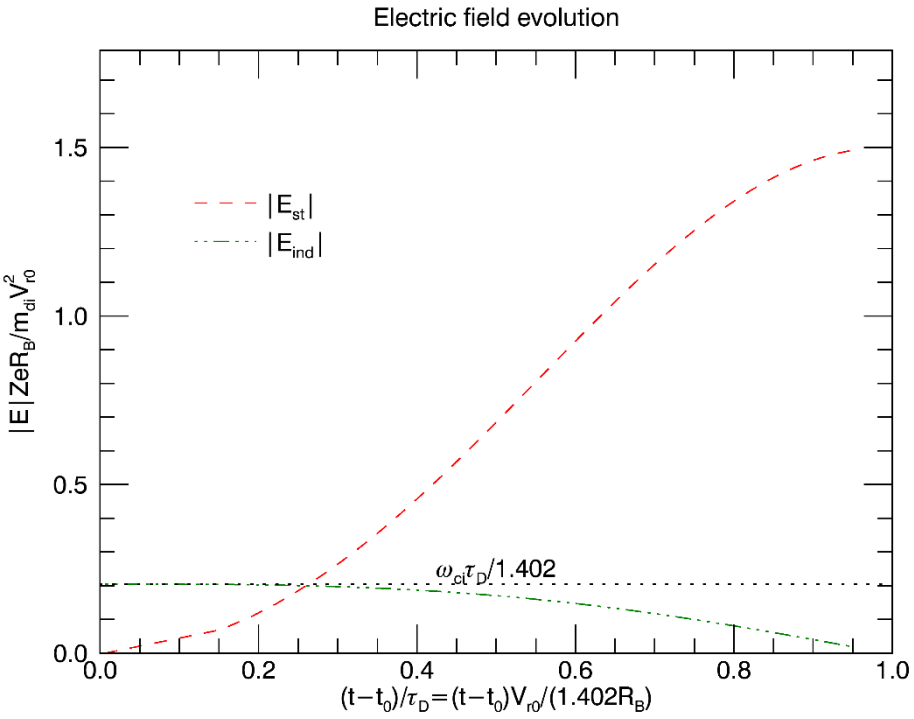

Figure 2.5: Characteristic electric field strengths over time for $\omega_{ci}^{d}\tau_D = 0.3$.

With the differential equation for $\tilde{R}$, the characteristic magnitudes of the components of the electric fields become

$$|\boldsymbol{E}_{ind}| = \partial_t R\, B \approx \frac{m_{di}V_{r0}^2}{Z_d e R_B}\left(\frac{\omega_{ci}^{d}\tau_D}{1.402}\right) d_{\tilde{t}}\tilde{R}, \tag{2.3}$$

and

$$|\boldsymbol{E}_{st}| = \frac{m_{di}}{Z_d e}|\partial_t^2 R| = \frac{3}{2}\frac{m_{di}V_{r0}^2}{Z_d e R_B}\frac{\tilde{R}^2}{\beta^{2/3}}, \tag{2.4}$$

where ω_{ci}^{d} is the cyclotron frequency for an ion in the LPP in a magnetic field B at $r = R(t)$. It should be remembered that within the context of particles moving through the CM sheath, the ions do not actually move in close orbits in the lab frame and their energy changes significantly on the passage through the sheath. The requirement for such orbit motion would be $\omega_{ci}^{d}\tau_D \gg 1$. As seen in Fig. 2.3, that has rarely been the case. From these relations, it is clear that the induced field monotonically decreases in strength up to $t = \tau_D$ when the diamagnetic cavity stagnates and $\boldsymbol{E}_{ind}$ goes to 0. The electrostatic field on the other hand is initially zero and grows as the surface area of the LPP. The relative size of their peak values is determined entirely by the parameter $\omega_{ci}^{d}\tau_D \sim B_0^{1/3}V_{r0}^{2/3}$ while their variation over time, determined by $\beta \sim V_{r0}^{2/3}B_0^{-2/3}$, is shown in Fig. 2.5 for a parameter of $\omega_{ci}^{d}\tau_D = 0.3$.

Characterizing the coupling between the diamagnetic cavity and an ambient plasma is just a matter of observing that the ambient ions will also see the fields of the diamagnetic cavity. In the weak coupling limit, the ambient ion response will be exactly the same as the LPP ions but as if they are entering the sheath region with 0 velocity. This would be like injecting particles at $x = 0$ in the CM model of Fig. 2.2. The ambient ions will be accelerated in the direction opposite that of the diamagnetic current by $\boldsymbol{E}_{ind}$ and *toward* the center of the LPP via $\boldsymbol{E}_{st}$; the ratio of these accelerations being set largely by $\omega_{ci}^{d}\tau_D$. The time dependence of $\boldsymbol{E}_{st}$ and $\boldsymbol{E}_{ind}$ as well as the fact that the number of ions affected goes as t^3 ensures that the electrostatic field is never negligible and, for typical magnetized LPP parameters, it will have the greater effect on the ambient ions.

When the presence of the ambient plasma cannot be neglected in the strong-coupling limit, more parameters appear. In the case of a cold, stationary background plasma of density, n_a, charge,

Z_a, and ion mass, m_{ai}, the two that appear most frequently are the equal mass radius, R_m, defined as

$$R_m^3 \equiv \frac{3}{4\pi}\frac{m_{di}N_{di}}{m_{ai}n_{ai}}$$

and the equal charge radius, R_q, defined similarly as

$$R_q^3 \equiv \frac{3}{4\pi}\frac{Z_d N_{di}}{Z_a n_{ai}}.$$

They will appear later in the non-dimensionalized forms: $(R_m/R_0)^3$ and $\left(R_q/R_0\right)^3$ or $(R_m/R_B)^3 = M_A^{-2}$ and $\left(R_q/R_B\right)^3$. In the latter forms, they take the simple interpretations of the mass density ratio and charge density ratio between the LPP and ambient plasma at peak diamagnetism. As far as the analysis of their affect on the LPP and coupling, their relationship to the electromagnetic fields has not been clearly set by experiments but their appearance is almost assured. The simplest way to see how they might influence the LPP-ambient coupling is to note that any term that is affected by mass density will have the ratio R/R_m and similarly for the charge density, R/R_q. Such is the case for the Lorentz term and the Hall term, respectively, in Ohm's law.

Chapter 3-Experiment and Diagnostics

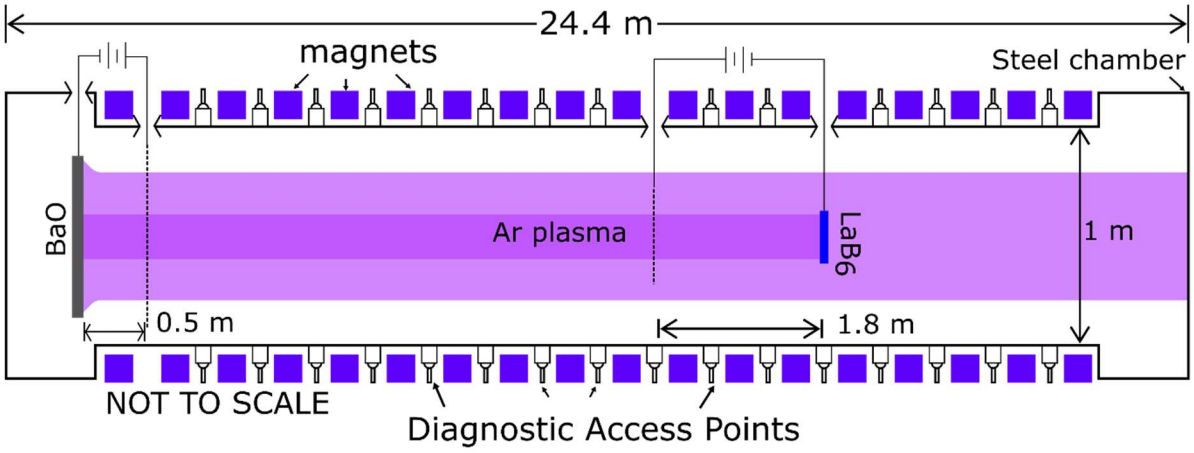

Figure 3.1: Cartoon of LAPD's vacuum chamber with primary and secondary cathode plasma sources.

Table 3.1: Standard Discharge and basic plasma parameters. Ion terms are for a singly-ionized argon plasma.

Quantity	**BaO**	**LaB_6**
n_e (10^{12} cm^{-3})	1-2	4-8
T_e (eV)	5-10	10-15
B_0 (G)	200-1000+	200-1000+
Plasma radius (cm)	30	5
$\beta_{th} \equiv 2\mu_0 n_e T_e / B_0^2$	0.0002-0.004	0.004-0.05
ω_{pe}/ω_{ce}	4-16	10-40
$v_{th,i} = \sqrt{T_i/m_i}$ (10^5 cm/s)	1	~ 2
$c_s = \sqrt{T_e/m_i}$ (10^5 cm/s)	3.5-5	5-6
$\omega_{ci} = ZeB_0/m_i$ (10^4 rad/s)	5-24	5-24

3.1 – Large Plasma Device

The experiments are conducted in the Large Plasma Device (LAPD) at UCLA [32]. The LAPD is a 24.4-m long cylindrical vacuum vessel of 1-m diameter. The vessel is fitted with a magnet system that provides a very uniform background magnetic field aligned with the cylinder's

axis. At one end of the device is an electrically isolated cathode-anode pair. The cathode is nickel-based with a diameter of about 60 cm and coated with a layer of barium oxide [33] which when heated to $\sim 900^\circ$ C is a strong thermionic emitter. At a repetition rate of 1 Hz, the cathode is biased relative to a semi-transparent mesh anode to form a high-current discharge in which energetic electrons, or primaries, travel down the magnetic field lines and ionize the neutral gas. This creates a quiescent ($\delta n/n \sim 5\%$) plasma with net-zero current that typically lasts a few milliseconds and is used as the ambient plasma in this experiment. The relative geometry of the machine is shown in Fig. 3.1. Typical parameters of this discharge are shown in Table 3.1.

Recently, newer thermionic cathode designs made of sintered lanthanum hexaboride (LaB_6) have been developed to produce higher density and higher temperature plasmas, since LaB_6 is a better emitter of primary electrons than BaO. In this experiment, a carbon target is placed within the ambient plasma which blocks field-aligned primaries. This results in an unwanted depression in density downstream of the BaO cathode. For the parallel expansion case, a 10-cm radius LaB_6 cathode was inserted to inject primaries from the other direction (see Figure 3.1). This reduced the density gradient in the immediate vicinity of the carbon target. Additionally, the primaries from the LaB_6 provided an increased population of metastable argon ions for use with the laser-induced fluorescence (LIF) diagnostic which will be described later in this chapter. For the cross-field expansion case, the depression does not interfere with the expansion.

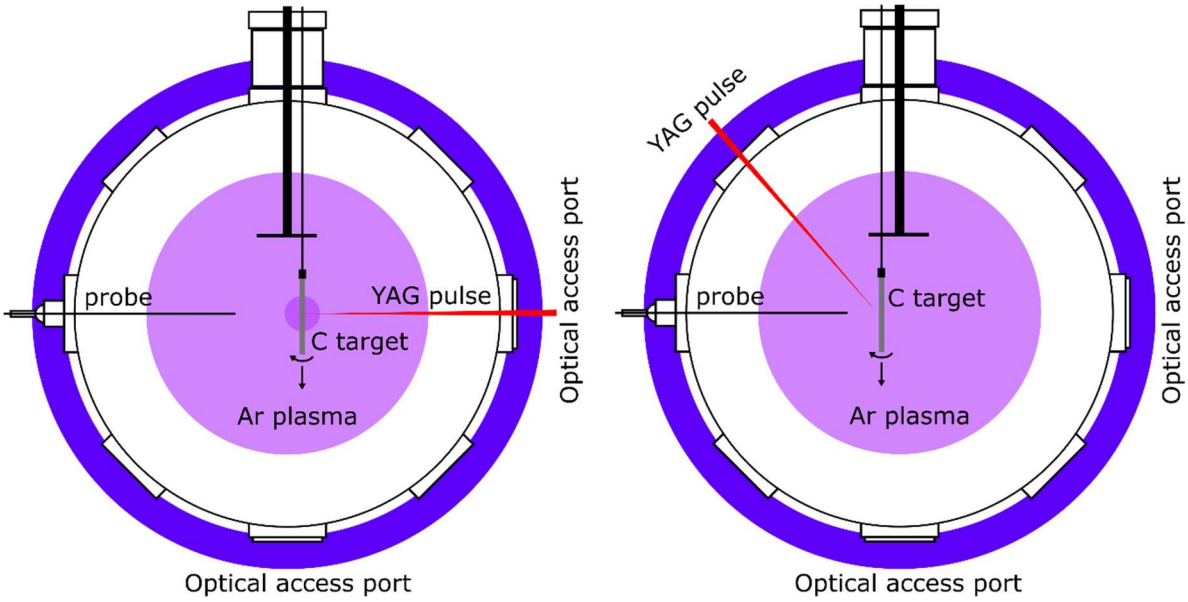

Figure 3.2: Cartoon cross-sections of the LaPD for the parallel expansion geometry (left) and the cross-field expansion geometry (right) of the LPP experiments.

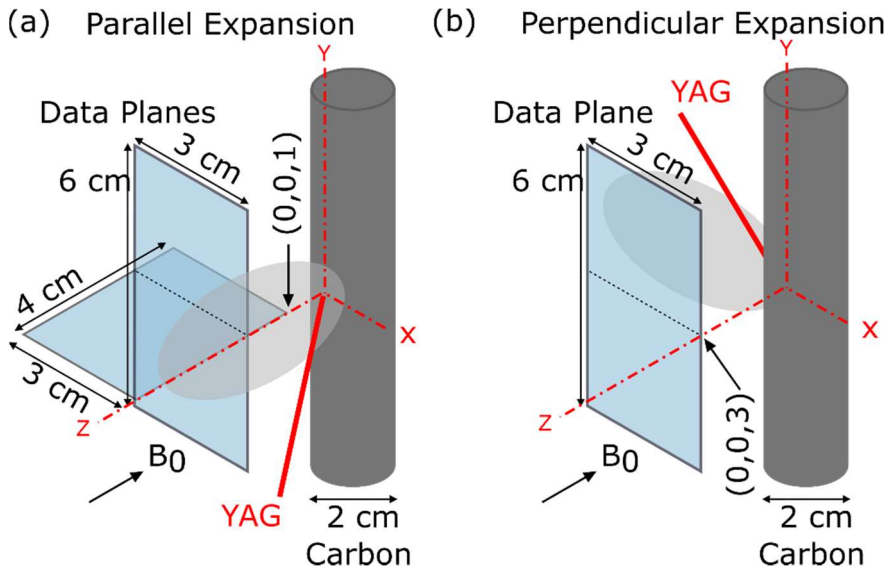

Figure 3.3: Target region geometry in relation to magnetic field and typical probe data planes.

3.2 – Laser-Produced Plasma

The LPP in this experiment is generated with a Nd:YAG, flashlamp-pumped laser with pulse characteristics given in Table 3.2. The beam is focused onto the surface of a cylindrical carbon target (⌀1.96 cm) with a typical spot size $R_0 = 250\ \mu$m. The small spot size ($< 1/2°$) means that the curved nature of the surface will not play a significant role and each shot can be treated as if it is emerging from a planar target. Two beam-target geometries are used: one for the parallel LPP and one the cross-field LPP expansions. Both geometries are shown in Fig. 3.2. Not shown in this figure is that the carbon target is slightly offset from the $x - y$ plane of the probe and machine cross-section by about 3 centimeters as shown in Fig. 3.3. The LPP is produced at the same 1 Hz cadence of the LAPD discharges. The repeated striking of the laser upon the target surface leaves a pit in the surface. Frequent movement of the target is required to present a fresh surface for the laser and prevent the pit geometry from affecting the LPP dynamics.

Table 3.2: Basic laser parameters.

Laser Parameter	Value (unit)
E_L	$1\ J$
δt (pulse length)	8 ns
R_0 (focal radius)	$250\ \mu$m
I_L	6.37×10^{10} W/cm^2
λ	1064 nm
$\nu = c/\lambda$	281.8 THz
n_{cr} (critical density)	9.84×10^{20} cm^{-3}

The cylindrical geometry of the target allows for simple rotation of the target every few laser pulses and translation in the $\hat{y}$-direction after a 360° rotation. This gives a finite lifetime for a target which necessitates frequent changing of spent targets. For optimization of reproducibility in LPP experiments, this frequency must be minimized. Previous experiments with this LPP setup

have determined that bulk characteristics are not significantly modified if a few pulses land on the same point on the surface of the target. To extend the period between target exchanges, 5 shots with the laser are fired at the same position before the target is rotated to present a fresh surface.

Some of the basic properties of the LPP plasma generated by the laser pulses in the manner described above were determined in earlier experiments with a similar setup [34]. The quantities that are important to the characterization of the expansion and dynamics are the ablation velocities (normal and tangential to the target surface), the total number of particles ablated, the initial temperature of the plasma, and the average charge state of the ablated ions. These values often have large error bars (as high as 50%) due the difficulty of probing such a small geometry where R_0 is far smaller than most physical probes. The accepted scaling relations for the normal ablation velocity, V_n, and the total number of ions ablated, N_i, are [35,36,37]

$$V_n \sim I_L^{0.2}, \quad N_i \sim I_L^{0.6}$$

for lasers where inverse bremsstrahlung is the dominant mechanism of energy deposition. This is generally true for laser intensities below 10^{14} W/cm^2 [38]. In the case of a graphite target, these relations become [35,36]

$$V_n = 2.25 \times 10^7 \left(\frac{I_L}{10^{12}}\right)^{0.2} \text{ (cm/s)}$$

and

$$N_i = 1.34 \times 10^{16} \left(\frac{I_L}{10^{12}}\right)^{0.6}.$$

For the laser intensity in Table 3.2, the resulting value of V_n is 1.3×10^7 cm/s which also gives a hydrodynamic time of $t_0 = 1.93$ ns. Puell [13], presents a theoretical argument for the relationship

between the expansion velocity and the temperature arguing essentially that the local speed of expansion is equal to the sound speed, $c_s = \sqrt{\alpha\langle Z\rangle T_e/m_i}$, where $\langle Z\rangle$ is the average ionization state and α is a parameter that characterizes the equilibration of ion and electron temperatures. This is also consistent with the Nemchinov model. For a polytropic plasma with $\gamma = 5/3$ for the electrons, the above equation for V_n would give for carbon at $t = t_0$

$$T_e = \frac{541}{\alpha\bar{Z}}\left(\frac{I_L}{10^{12}}\right)^{0.4} \text{ eV}$$

and

$$\alpha = \begin{cases} \dfrac{\langle Z\rangle + 1}{\langle Z\rangle}, & T_i = T_e \\ 1, & T_i = 0 \end{cases}.$$

The exponents in the literature are slightly different for different theoretical models and often carry with them errors on the order of a few to 10 percent. This combined with the temperature dependence in the quantity $\alpha\langle Z\rangle$ led Puell [39] to an experimental temperature scaling of

$$T_e = 162\left(\frac{I_L}{10^{12}}\right)^{0.44} \text{ eV}$$

where better agreement between their experiment and theory was given for $T_e = T_i$ and thus $\alpha = (\langle Z\rangle + 1)/\langle Z\rangle$. This is partially justified by looking at the expected ion-electron collision time and comparing it to other characteristic times of the initial LPP.

The estimated parameters based on the experimental scaling relations above are given in Table 3.3. For the densities and derived quantities, a spherical model is assumed based on arguments of [13] and references therein. They also conveniently lend themselves nicely to the Nemchinov model of fluid expansion discussed in Appendix A. In the initial state of the LPP, the

characteristic time for the equilibration of the electron and carbon ion temperatures through Coulomb collisions can be expressed as

$$t_T \equiv \frac{1}{\nu_T} = \frac{10}{\langle Z \rangle Z^2} \text{ ns}$$

The initial expansion will proceed on the hydrodynamic time scale. Thus if $\langle Z \rangle > 1$, all the charge states with $Z \geq 2$ will essentially equilibrate by the time the laser has shut off and the expansion phase begins. The estimate of T_e suggests that the LPP will not have a very large population of $Z = 1$ ions—even with potentially large uncertainties in T_e—due to carbon $Z = 1$ ionization energy being only 11.26 eV. To get the average charge state in the plasma, which is needed for the electron density and various other plasma parameters that will arise, a model for the ionization states is required. For this, a simple Saha equilibrium is applied to the seed plasma. Corona models have been applied [13] which are considerably more complicated and dependent on more parameters than a Saha equilibrium. The high densities on the other hand ensure a crude estimation by a Saha equilibrium is adequate [40].

The Saha equation gives us a way to relate $\{n^z\}, n_e, T_e, n_t$, where n_t is the density of all carbon atoms and ions and $\{n^z\}$ are the concentrations of ions of charge Z. Specifically, after T_e and any other one quantity are specified, the remainder can be calculated. In its simple form, it is

$$n^{z+1} = \frac{n^z}{n_e} \frac{G^{z+1}}{G^z} \left(\frac{\sqrt{2\pi m_e T_e}}{h} \right)^3 e^{-\frac{E_{z+1} - E_z}{T_e}}$$

where $E_{z+1} - E_z$ is the energy to ionization from charge state z to $z + 1$ and G^z is the partition function of charge state Z. The calculation is made simpler if the further assumption that

Table 3.3: Estimated parameters of the LPP parameters initially at $t = t_0$ and near peak diamagnetism $t = 240$ ns for $B_0 = 750$ G. AMPTE parameters estimated from Bernhardt 1987 [11] for the March 21, 1985 barium release. Normalization parameters are initial hydrodynamic parameters, t_0, R_0, and V_n.

LPP Parameter	**Value ($t = t_0$)**	**Value ($t = 240\ ns$)**	**AMPTE (03.21.1985)#**
T_e	48 eV	~ 0.5 eV *	0.7 eV
N_i	2×10^{15}	$1 - 2 \times 10^{15}$	7.4×10^{24}
$\langle Z \rangle$	4.6	~ 2	1
n_i	3.1×10^{19} cm^{-3}	3.8×10^{13} cm^{-3}#	1.0×10^{8} cm^{-3}
n_e	1.4×10^{20} cm^{-3}	7.7×10^{13} cm^{-3}#	1.0×10^{8} cm^{-3}
$\ln \Lambda_{ei}$	4.1	6.3	13.3
$\nu_{pe} t_0$	1.3×10^{4}	150	9.0×10^{7}
$\nu_{ei} t_0$	9.5×10^{3}	2.7	6.6×10^{3}
$\nu_{pi} t_0$	3.0×10^{3}	0.42	1.8×10^{5}
$\nu_T t_0$	19	9.9×10^{-4}	5.3×10^{-2}
$\nu_{ce} t_0$	4.0	---	220
$\nu_{ci} t_0$	8.3×10^{-4}	---	8.9×10^{-13}
v_{Te}/V_{r0}	22	3.2	269
c_s/V_{r0}	0.46	5.5×10^{-2}	0.69
v_{Ti}/V_{r0}	0.15		0.54
v_A/V_{r0}	6.5×10^{-5}	5.9×10^{-2}	1.2×10^{-3}
$c/\omega_{pe} R_0$	1.8×10^{-5}	2.4	4.1×10^{-4}
$c/\omega_{pi} R_0$	0.12	880	0.21
$v_{T_e}/R_0 \omega_{ce}$	0.88	0.12	0.28
R_B/R_0	85		170
$Z\rho_d = v_n/\omega_{ci} (Z = 1)$	870		160
$\beta = \left(\frac{R_B}{R_0}\right)^3$	6×10^{5}		$\sim 10^{7}$
$\omega_{ci} \tau_D$	0.3		~ 1
$\left(\frac{R_q}{R_0}\right)^3$	$\sim 2 \times 10^{7}$		$\sim 10^{11}$
$\left(\frac{R_m}{R_0}\right)^3 = \frac{1}{M_A^2}\left(\frac{R_B}{R_0}\right)^3$	6×10^{5}		$\sim 10^{11}$

* = approximate volume average for $v_{Te} \sim V_{r0}$
\# = estimated from available data applying a spherical expansion model

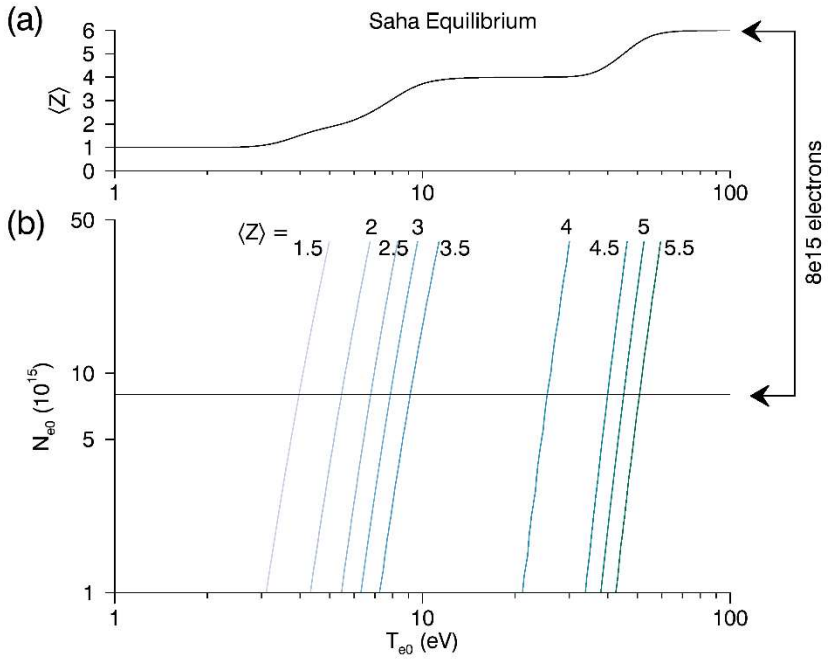

Figure 3.4: Saha equilibrium as a function of LPP characteristics. (a) Charge state as a function of T_e for $N_{e0} = 8 \times 10^{15}$ electrons. (b) Charge state for variable T_e and N_{e0}.

$G^z \approx G^{z+1}$. This is a good approximation provided the temperature is high enough relative to the energy of excited states or if the populations of excited states are ignored altogether, which is commonly done for ionization to $Z = 5{,}6$ where the ionization energy jumps owing to the strong binding of the $n = 1$ electrons. For the present parameters, this only leads to a minor overestimate the energy coupled to the LPP. As shown in Appendix A, the most highly ionized particles recombine early in the expansion phase so their exact populations should not make much of a difference to the diamagnetic cavity. A calculation of the resulting average charge state as a function of the total number of electrons and the electron temperature is shown in Fig. 3.4b.

The range of parameters in Fig. 3.4b were chosen to show the effect of large uncertainties near the estimated experimental parameters. The average charge state quickly approaches $\langle Z \rangle = 4$

as the temperature increases and reaches a plateau for a wide range in T_e. It is also apparent that the total number of particles ablated plays little role in the average charge state over 2 orders of magnitude. The curve for the estimated number of electrons is in Fig. 3.4a to show more clearly the variation with temperature. Using the parameters from empirical scaling relations, one gets that the average charge state of the LPP should be $\langle Z \rangle \sim 4.5$ with the charge state distribution of Table 3.4. Similar calculations by [13,41] show $\langle Z \rangle \geq 4$. A further validation of these estimates can be seen from the energy balance between the laser pulse and the LPP.

Table 3.4: Estimated distribution of charge states from a Saha Equilibrium with $T_e = 48$ eV with a total number of 2×10^{15} ions in a spherical volume of radius $R_0 = 0.025$ cm.

Charge State, $\boldsymbol{Z}$	1	2	3	4	5	6
$\frac{N_z}{N_t}$	10^{-10}	10^{-7}	10^{-4}	0.43	0.49	0.073

The energy absorbed by the solid is primarily stored in the ionization potentials of the charges and the thermal distribution of particles. The energy content using the distribution of Table 3.4 is

$$E_{tot} = \frac{3}{2} N_i (\langle Z \rangle + 1) T_e + \sum_{z=1}^{6} N_z E_z = 130 \text{ mJ} + 134 \text{ mJ} = 0.264 \text{ J}$$

where the second last expression shows the separate contributions from the thermal energy and the ionization potential. The main loss mechanism accounting for the difference between E_{tot} and E_{laser} is the amount of energy lost from reflection of the laser light and radiation escaping the surface of the incipient plasma during the heating phase. If the assumption is made that all 2×10^{15} ions expand with the speed $V_{r0} = 1.3 \times 10^7$ cm/s, the energy in the expansion would be 334

mJ. This is comparable to the total energy of ionization if all the ions had $Z = 6$. The corresponding temperature for a fully ionized carbon plasma is in excess of 100 eV by Saha equilibrium and even higher if a more detailed model were applied. If we account for the geometric effect wherein the ion velocities scale spatially with the more realistic velocity profile $V_i(r) \sim r$, the energy in the expansion is 40% lower (200 mJ) or well within the range consistent with initial $T_e > 40$ eV.

The model for the expansion with recombination in Appendix A uses the above parameters to show that the variation of temperature changes from $T_e \sim t^{-2}$ to $T_e \sim t^{-1}$. The ionization in the later stage is "frozen-in" at $\langle Z \rangle \approx 2$ with a temperature on the order of $T_e \sim 1$ eV during the times relevant to the LPP expansion in the magnetic field. These are the values that were used to compile the parameters in Table 3.3 for $t = \tau_D$.

3.3 – Imaging Diagnostic

The first diagnostic for a qualitative description of the expansion is visible light imaging. This is accomplished with a fast exposure ($\Delta t_{exp} \geq 3$ ns), CCD camera imaging through one of the optical access ports shown in Fig. 3.2. The phosphor screen has a roughly uniform transmission with quantum efficiencies on the order of 30% through the range 280-1000 nm. All wavelengths are in standard air wavelengths. Three filter settings are used:

1) Unfiltered – (in the CCD range)

2) wideband filtered – A 10-nm HWHM filter is used centered at 460 nm.

3) narrowband filtered – An interference filter of HWHM 1-nm center about 461 nm.

The unfiltered imaging tracks the "total" emission of the plasma which is dominated by the LPP electrons and ions through free-free electrons transitions and radiative recombination and line emission cascade. Radiances of visible emission from a dense plasma with $T_e \sim h\nu_{vis}$ depend on the mechanism and the largest contributors are: bremsstrahlung, $P_b \sim n_e^2\sqrt{T_e}$; recombination,

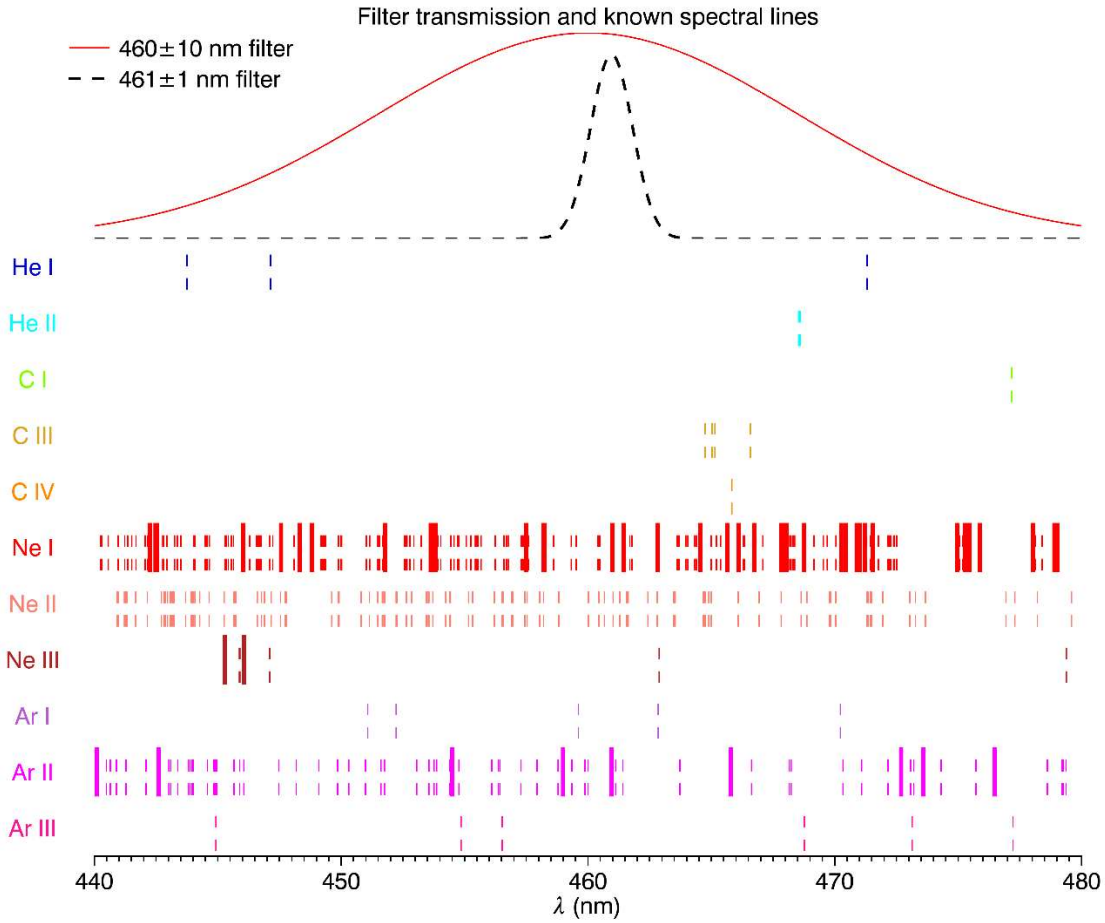

Figure 3.5: Filter transfer functions against NIST's accepted line transitions. Dashed lines are predicted, mostly highly excited state transitions, while solid lines indicate readily observable in gas discharge lamps.

$P_{recom} \sim n_e^2/\sqrt{T_e}$; and free-bound transitions, $P_{fb} \sim n_e^2/\sqrt{T_e}$ [13,42]. Thus, gradients in the unfiltered image are 4 times more sensitive to density gradients than temperature gradients in the

plasma. This allows an estimation of the parameter $\nabla \ln n_e$ from imaging. The 10-nm filter and 1-nm filter have optical transfer functions shown at the top of Fig. 3.5. Also shown are the NIST [43] emission lines that fall within the optical collection of these filters for the various possible charges in the LPP and in different LaPD gases. Solid lines correspond to lines well-characterized and observed in experiments and dashed correspond to those predicted to exist according to NIST's resources. From this graphic, it is clear the 10-nm filter may capture some line emission from the LPP and collects varying amounts of line emission from the different gases used to make plasma. The 10-nm filter is more sensitive to temperature variations of free-free within the LPP owing to the narrower range in which $T_e \sim h\nu_{filtered}$ and blocking much of the continuous emission. The 1-nm filter excludes most of the possible lines and is used to remove background signal and capture light from the Ar^+ 460.957 nm line used in the LIF diagnostic.

3.4—Field Diagnostics

3.4.1—Magnetic Flux Probe

The magnetic field data is collected with one of LAPD's standard magnetic flux probes. On approximately a 3 mm cube, two 5-turn coils are differentially wound for each of the three axes. The signals are then differentially amplified to reduce electrostatic pickup and yield a direct measure of $\partial_t \boldsymbol{B}$. Time integration of the signal, which is digitized at either 100 MHz or 1.25 GHz, gives $\boldsymbol{B}$. Although practical considerations of the frequency response cannot take full advantage of the 1.25 GHz digitization, the high digitization rate reduces aliasing errors with large $\partial_t B$ signals of the diamagnetic cavity.

In additional to the magnetic fields, the magnetic flux probe, with sufficient spatial resolution, can produce estimates of the induced electric field. For this, Faraday's law is used,

$$\nabla \times \boldsymbol{E} + \partial_t \boldsymbol{B} = 0$$

from which one gets, in the Coulomb gauge,

$$\boldsymbol{E}_{ind} = -\partial_t \boldsymbol{A}.$$

If no symmetry exists, this equation can only be solved for the induced electric field $\boldsymbol{E}_{ind}$ by first solving for the vector potential,

$$-\nabla^2 \boldsymbol{A} = \nabla \times \boldsymbol{B},$$

Which requires a Laplace solver or a Fourier inversion method. If cylindrical symmetry is present, the z component of the equation can be integrated from

$$\frac{1}{r}\partial_r(rE_\theta) = -\partial_t B_z$$

To get

$$E_\theta(r_1) - \frac{r_0}{r_1}E_\theta(r_0) = -\frac{1}{r_1}\int_{r_0}^{r_1} dr\, r\partial_t B_z.$$

Without a definite boundary condition, this problem would have to be solved for $r_1 \to \infty$ to capture not only local generation of E_{ind} but also signals radiating away the LPP source region. Across the ambient magnetic field, the primary modes that can travel across the field are Alfvén modes and magnetosonic modes, which are tied to perturbations in plasma density. By limiting the analysis to times smaller than the Alfvénic transit time to a distance r_1 from the LPP, the error in taking $E_\theta(r_1) \approx 0$ can be assumed small.

3.4.2—Emissive Probe

To measure the electrostatic field, a floating emissive probe is used. The basic idea of a floating probe, which has an infinite impedance to ground, is that a conductor placed in the plasma collects charge until the electric field at the surface is such that net current is zero,

$$\partial_t \rho_c = -\nabla \cdot \boldsymbol{J} \approx 0.$$

In the Coulomb gauge, this means the potential of the conductor reaches a constant value locally in time. For a simple conductor in a given plasma, this will occur in a time $\delta t \gg 1/\omega_{pi}$ (ion-sheath transit time). This is due to the response of the sheath that forms at the surface of the conductor. If the local plasma potential changes, the electrons quickly respond to the new field but net current is collected by the probe. The heavier ions must be given time to cancel the current. A very simplified analysis when the conductor can emit electrons leads to the following relationship between the plasma and the conductor potentials,

$$\phi_{probe} = \phi_{plasma} - T_e \ln \frac{j_e}{j_i + j_{emit}},$$

where j_e and j_i are the plasma electron and ion saturation fluxes to the conducting surface and j_{emit} is the emission flux. It is derived by assuming floating conditions for Boltzmann distributed electrons from the plasma and the presence of a Bohm pre-sheath. The slow response of the massive ions gives this sheath a capacitive response when operating at high frequencies and in high densities, the conductor surface can become coated with dielectric impurities and ruin the measurement.

For a thermionic emitter, the conductor is made hot enough to emit electrons. The higher the temperature, the less the equilibrium potential profile depends on the ion flux. Additionally,

the hot surface helps keep the probe clean and free of contaminants. If the probe is sufficiently emissive, the probe potential equilibrates on a time scale $\delta t < 1/\omega_{pi}$ to

$$\phi_{probe} = \phi_{plasma} - \alpha T_e,$$

where α is a constant approximately equal to 1 [44,45]. The temperature dependence can never truly be removed but α changes only with highly exotic, low-density electron conditions [46]. If the plasma temperature is sufficiently uniform or low, this effect is not reflected in the electric field calculated from the measurement. In the laser-produced plasma, the error amounts to about 1 V and the sign of α means that the electric field will tend to be underestimated.

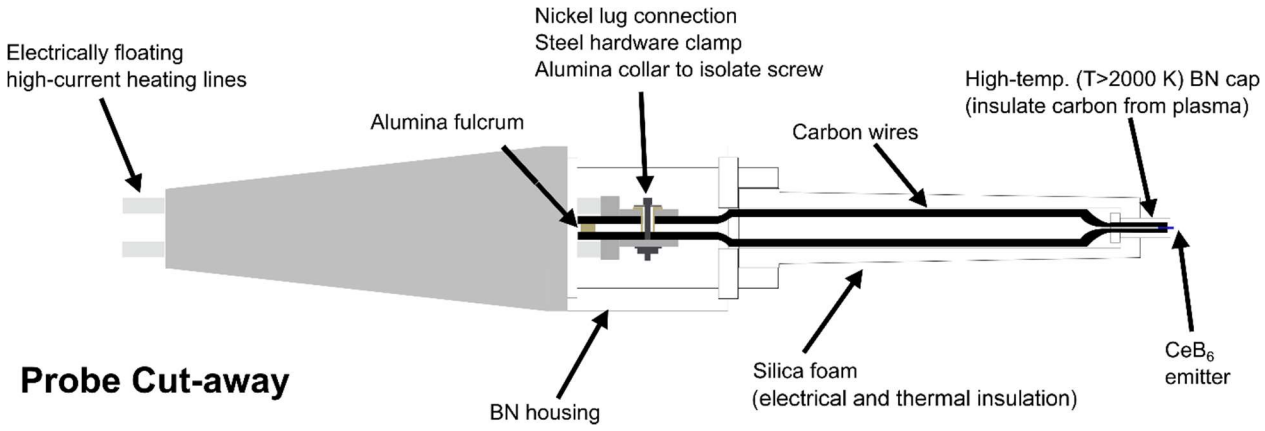

Figure 3.6: Design of emissive probe.

Figure 3.7: Picture of emissive probe and the relative size of the measuring probe tip and the support structure.

The emissive probe used in this experiment is a resistively heated emissive probe utilizing CeB_6 as the thermionic emitter—electrochemically similar to the LaB_6 plasma source in LAPD. A cross section of the emissive probe is shown in Fig. 3.6 and a picture showing the size of the probe relative to a dime is shown in Fig. 3.7. The operating densities of emissive probes are determined by their ability to survive the temperatures needed to emit electron fluxes much higher than the ion collection flux from the plasma. For typical tungsten wire probes (the standard emissive probe design), this is absolutely limited by the melting of the tungsten which would occur around $n_e \sim 10^{13}$ cm^{-3} [47]. In practice, however, the probe support structures fail much sooner at densities on the order of $\sim 10^{12}$ cm^{-3}. The probe used in this experiment has be used and shown to work in plasmas as dense and hot as $\sim 10^{13}$ cm^{-3} and 10 eV [48].

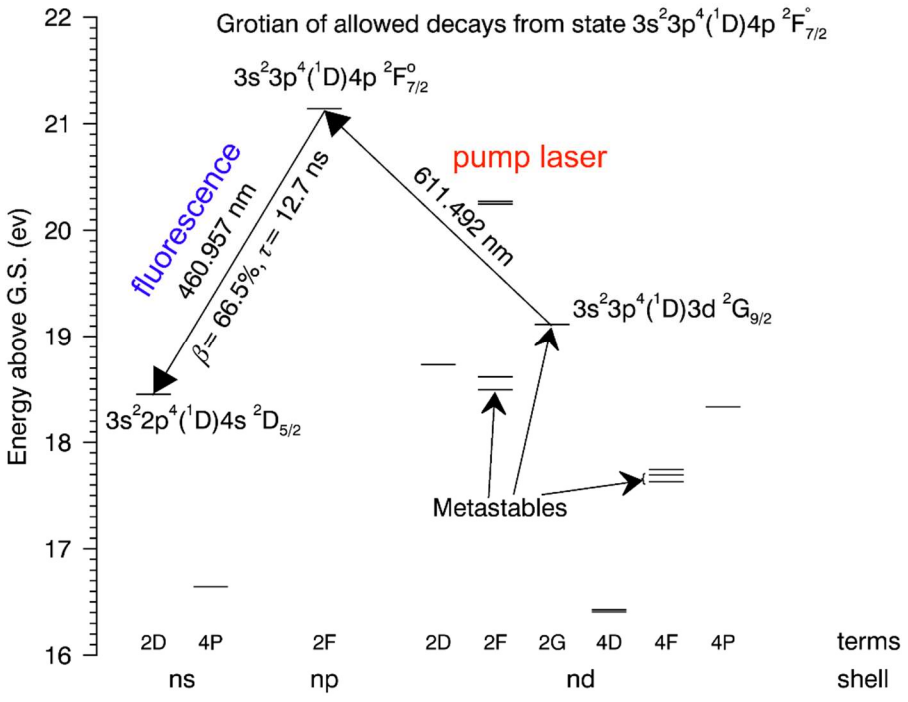

Figure 3.8: Partial Grotian diagram showing relation of relevant states to the fluorescing state. The LIF scheme used in the experiments consists of the 3 levels connected by solid lines.

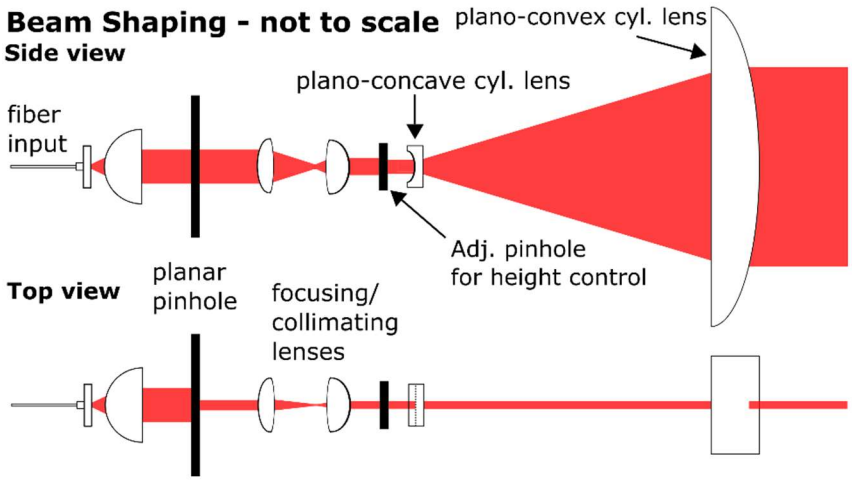

Figure 3.9: Shaping of the planar LIF diagnostic. Fiber brings in output from dye laser. Target region typically located 1 m from final lens.

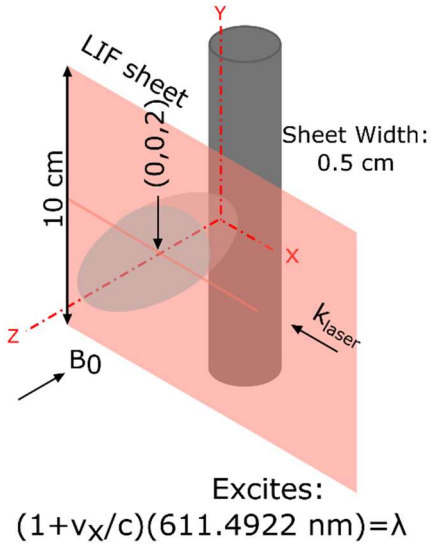

Figure 3.10: Geometry of LIF sheet as it enters the target region.

3.5—Laser-Induced Fluorescence

To directly probe the response of the ambient plasma to the electric fields, an LIF diagnostic in an argon plasma is used. The technique is a standard 3-level scheme, depicted with

solid lines in Fig. 3.8, that excites a high-lying metastable of the argon ion, Ar^{+m} to an upper level, Ar^{+*} with a narrow $\delta\lambda \leq 0.5$ pm (400 MHz bandwidth) dye laser near the transition of 611.4922 nm. The dye laser's light is fed into the LAPD through a fiber and a series of shaping lenses to the target region. The Ar^{+*} state has a lifetime of 10 ns and it decays with a branching ratio of 66.5% through emission of a 460.957 nm photon to the final state. A partial Grotian diagram showing the LIF scheme among the other possible decays from the Ar^{+*} state are shown in Fig. 3.9. Also shown are a few of the other high-lying metastables that also exist in argon. With a tunable input laser, the scheme can be used to probe the distribution of ions in velocity space.

A particle in motion relative to the laser wave vector, $\boldsymbol{k}$, does not see the frequency and wavelength of the laser itself, rather they are Doppler shifted. In the non-relativistic limit, the condition for excitation is

$$\omega - \boldsymbol{v} \cdot \boldsymbol{k} = \omega_0$$

or

$$\frac{v}{c} = \frac{\lambda - \lambda_0}{\lambda_0}$$

where $\omega_0 = c2\pi/\lambda_0$ refers to the transition in the ion's rest frame and the sign convention is chosen such that positive velocity is moving into the laser beam: $v = v_x > 0$ means $\boldsymbol{v} \cdot \boldsymbol{k} < 0$. With the dye laser's maximum resolution, the smallest measurable velocity is 2.5×10^4 cm/s, which is smaller than the ion thermal velocity and a small fraction of the sound speed. This is also the typical scale at which the diagnostic is able to detect net drifts in the ion population. Time resolution is provided by the fast camera previously mentioned. The lifetime of the transition ($\tau \sim$ 10 ns) and pulse length of the dye laser ($\Delta t_{dye} \sim 10$ ns) means that optimal light gathering is in

the range $20 - 40$ ns. Spatial resolution of the LIF signal is provided by the shaping lenses (setup shown in Fig. 3.9) which produce a planar beam of light aimed near the carbon target as in Fig. 3.10 with height and width $\delta y \sim 10$ cm and $\delta z \sim 0.5$ cm, respectively. A mirror placed 2.1 m away in the z-direction reflects the signal through a window leading out of the machine. The CCD camera is used with the 460 nm filter and 2.5x magnifying lens to capture the signal with resolution $\Delta x = \Delta y = 480$ μm.

The argon metastables are long-lived due to there being no allowed dipole transitions between them and any lower-lying levels in the Ar^+ electronic structure. They are populated by 2 primary reactions

$$e + Ar \rightarrow Ar^{+m} + 2e$$

$$e + Ar^+ \rightarrow e + Ar^{+*} \rightarrow e + Ar^{+m}$$

where the excited state in the second reaction could even by multiple ionization. It was determined by Goeckner [49] that the first reaction is the dominant one in tenuous, discharge-produced plasmas and further that the metastables are lost by collisions with the neutrals. In the LaPD, the neutral collision time is on the order of 200 μs for a neutral argon density of 6×10^{12} cm-3 and ion speed of 2×10^5 cm/s.

Since the metastable lies far above the neutral ground state ($\Delta E > 32$ eV), there are strict conditions for the plasma in order to ensure enough metastables are created in the first place. Using a secondary emission diagnostic, Hagstrum [50] determined the total population of metastables created by electron beams with given energies while Varga [51], using an improved technique, was able to extract a detailed cross section for metastable creation. These are shown in Fig. 3.11.

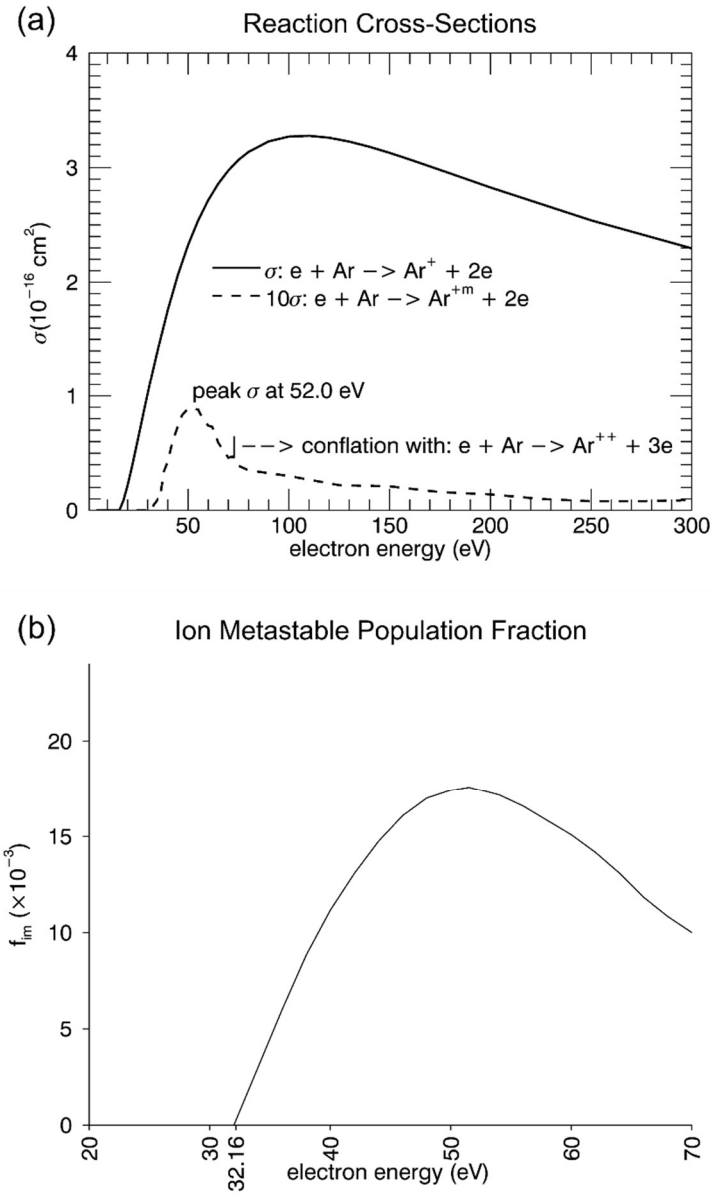

Figure 3.11: (a) measured [51] cross-section for creation of Ar^{+m} (dashed) relative to ionization cross-section (solid) and (b) the resulting population from of metastables according to [50].

Note that the technique used to obtain these data does not distinguish between the metastable states of Ar^+ so that the total 1% metastable population is in fact split among the 7 high-lying metastables; 4 of which are connected to the excited state in the LIF scheme (see Fig. 3.8). Also, the data becomes conflated with the process of doubly ionizing in a single step ($E > 65 - 75$ eV).

That is, electrons above this energy will start creating Ar^{++} in competition with creating Ar^{+m}. Since the primary electrons are not a pure beam and do not keep their full discharge energy as they propagate down the magnetic field, the discharge must be tailored to achieve the maximum metastable population at a given point in the plasma which should correspond to the highest population of $E \sim 50$ eV electrons. This is another reason why the LaB_6 cathode was needed in the parallel expansion case as the target blocks these crucial primaries. In addition discharge voltages are more limited with the BaO source due to sputtering. With the 10-cm LaB_6 cathode and its anode located 3.9 m and 2.1 m, respectively, from the target region, discharges on the order of 150 V optimized the LIF signal in the target region.

Timing control of the lasers and CCD imaging was provided by a new cRIO-based FPGA in communication with Stanford delay generators. The system, as an update to the stepping motor drivers from previous experiments, coordinated the triggering of the LPP and LIF laser pulses, the camera imaging, and target motion. Shot to shot timing jitter was $\leq$1 ns.

Chapter 4-Main Results

4.1—Laminar Fields

The model of a high-β expansion as presented in §2.3 yields convenient expressions for the electric fields in an LPP. This gives the rather counterintuitive expectation that whereas a collisional interaction would couple energy and momentum in the flow direction, the collisionless interaction, at least in a weak coupling regime, pulls in ions against the direction of the flow across the magnetic field. The data presented in this chapter are first used to justify the main assumptions made in the model of §2.3, namely that the electron pressure and resistivity are small contributors to the electric fields in the expansion phase. This provides a basis upon which the magnetic field data can be interpreted and connected to the structures observed in the measured electric fields.

The data are framed in the context of the contributions to and evolution of the total laminar $\boldsymbol{E}$. In terms of fluid variables, $\boldsymbol{E}$ is calculated from the generalized Ohm's law [52, pg. 91]

$$\boldsymbol{E} = \frac{\partial_t \boldsymbol{J}}{\omega_{pe}^2 \epsilon_0} + \frac{\nabla \cdot (\boldsymbol{V}\boldsymbol{J} + \boldsymbol{J}\boldsymbol{V})}{\omega_{pe}^2 \epsilon_0} - \boldsymbol{V} \times \boldsymbol{B} + \frac{\boldsymbol{J} \times \boldsymbol{B}}{e n_e} - \frac{\nabla p_e}{e n_e} + \eta \boldsymbol{J} \tag{4.1}$$

where terms of order m_e/m_i have been ignored. The first two terms are generally ignored if spatial and temporal scales are large compared to the electron motion and will be neglected here. Treating the terms as different electric field contributions, the inductive components of the electric field are connected to the magnetic field evolution through Faraday's law

$$\partial_t \boldsymbol{B} = -\nabla \times \boldsymbol{E} = \frac{\eta}{\mu_0} \nabla^2 \boldsymbol{B} + \nabla \times (\boldsymbol{V} \times \boldsymbol{B}) \tag{4.2}$$

where temperature gradients are neglected and electrostatic terms do not contribute.

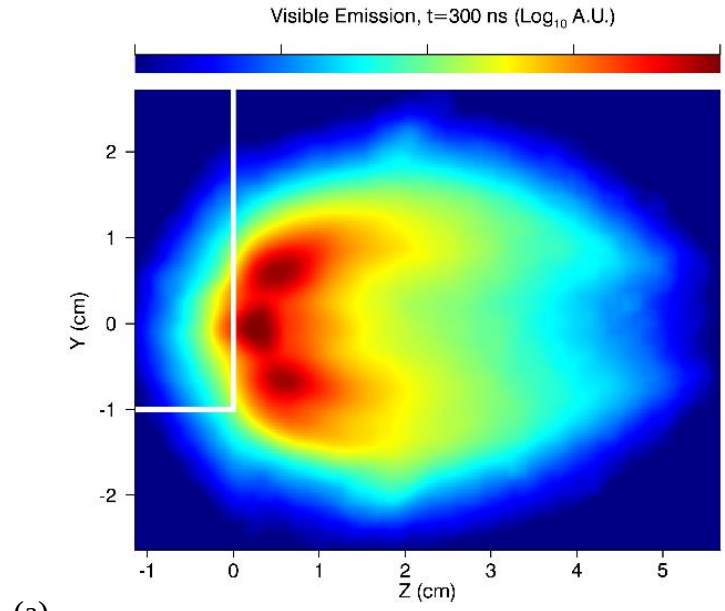

(a)

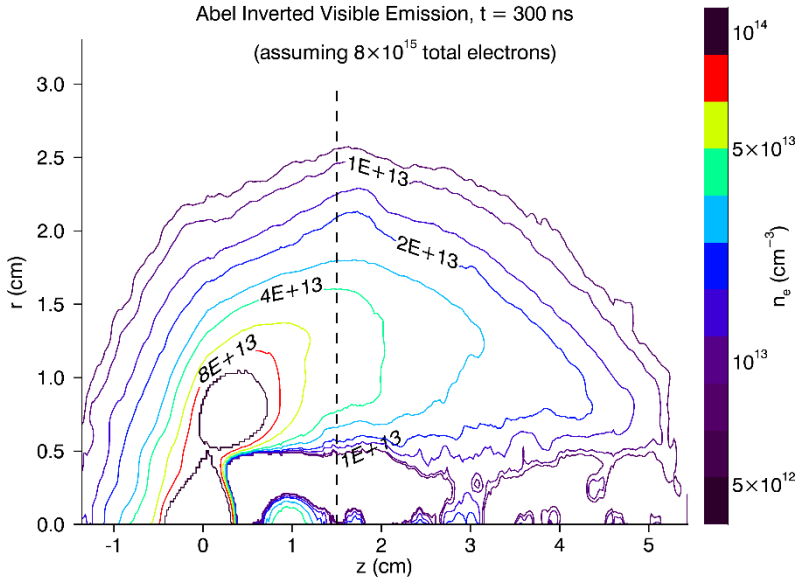

(b)

Figure 4.1: (a) False color image LPP at t=300 ns with position of carbon target outlined in white. (b) Abel-inverted electron density which has been normalized to a total number of 8×10^{15} electrons. The dashed line corresponds to Fig. 4.2.

4.2 - Imaging Data

4.2.1—Estimating n_e and $\nabla \ln n_e$

Direct measures of the electron density and temperature over the long time scales of high-β expansions are not trivial and have met with some limited success in experiments designed specifically to measure these quantities [22, 53]. The description here will rely mostly on the well-established models of hot, dense expansions (Appendix A). The imaging diagnostic allows a good qualitative description and a rough estimate of terms that require knowing n_e.

Images of the visible emission were taken with the CCD camera set at variable integration times. The variable integration was due the large difference in total emission power over time as the LPP cooled and its constituents recombined. An unfiltered, false color image of the LPP is shown in Fig. 4.1a with an integration time of 10 ns ending at $t = 300$ ns. Marked in white border is the target position within the image. The known size of the target gives the pixel resolution $\delta y = \delta z = 190$ μm. This time was chosen as the LPP appeared to have stagnated across the magnetic field. As it turned out, this time corresponds to shortly after peak diamagnetism, $\tau_D = 240$ ns, and the onset of collapse of the electromagnetic fields. In previous experiments on the diamagnetic cavity formation in a cross-field expansion, typical values of τ_D were about twice as long [54, 55]. Such a change in τ_D with change in angle between the target normal and the magnetic field has been observed previously [27]. There, it was explained as a change in the laser-solid interaction due to the incident angle of the laser beam and thus the initial conditions of the LPP. The important point of Fig. 4.1a is that the LPP emission exhibits very sharp gradients in emission intensity across $\boldsymbol{B}$. As explained in §3.3, the much stronger dependence of the visible emission on the local value

of n_e allows for a calculation of the density length scale and an estimate of the absolute electron density.

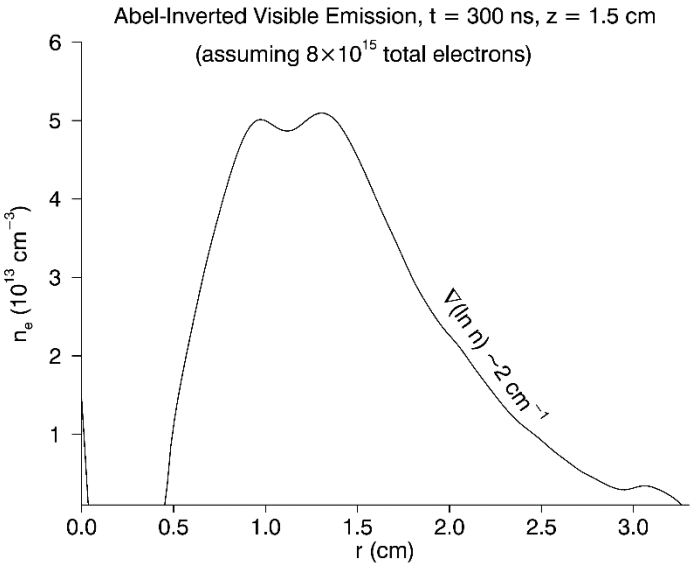

Figure 4.2: radial cross-section of the Abel-inverted visible emission at $z = 1.5$ cm.

If the $\nabla \ln T_e$ is assumed to be smaller than $\nabla \ln n_e$, then image is proportional to the line integration of n_e^2. Since the image in Fig. 4.1a is approximately cylindrically symmetric, the source function can be recovered by Abel inversion. Abel inversion is the formal process of mapping an image integrated over a Cartesian coordinate into its cylindrical coordinates. That is, for a source image of cylindrical symmetry, $I(y,z) = \int dx f(x,y,z) = \int dx f(r,z), 0 \leq r \leq \infty$, Abel inversion extracts $f(r,z)$. By normalizing the volume-integrated signal to 8×10^{15} electrons and accounting for the n_e^2 dependence of the visible emission (see §3.3), the contour plot of $n_e(r,z)$ in Fig. 4.1b is generated. This shows that near the edge of the LPP, $r = 2$ cm, the density is on the order of 4×10^{13} cm^{-3} and just inside, there is a density pile-up where the density may reach a value twice as high. These numbers are not to be taken as a highly accurate indicator of the electron

density but merely to show the order of magnitude absent an accurate absolute density calibration. A profile of Fig. 4.1b is shown in Fig. 4.2 near $z = 1.5$ cm to more clearly show the density variation. The density gradient, which is important for the contribution of the pressure term in Eq. 4.1, is independent of the absolute density.

As shown in Fig. 4.2, the length scale of the density variation, $(\nabla \ln n_e)^{-1}$, on the outer gradient is 0.5 cm. Following the contours in Fig. 4.1b, it exhibits a very slow variation in z as shown by the contours in Fig. 4.1b. The significant drop in density along $y = 0$ is due to a known issue in Abel inversion where the central axis is very sensitive to the initial value of the integration at the radial boundary. Though it is certainly possible that there is an interior gradient in density within the LPP, it is unclear if such a gradient is as strong as indicated in Fig. 4.2 without knowing the temperature and accounting for optical depth over the continuous visible emission. Since the volume of electrons near the axis is small, the sensitivity of the value from Abel inversion does not significantly affect the magnitude of n_e nor its gradient along the outer edge. The outer gradient is also unaffected by absorption since the tenuous ambient argon plasma is optically thin. The qualitative features of the evolution of the expansion are easier to see and better to compare in time through the 460 nm filter for which the integration time can be kept constant.

4.2.2—Time of Flight and Plasma Behavior

The 460 nm filter is centered near the same emission line as the 1 nm filter used for LIF but Fig. 3.5 indicates the possibility of seeing variation in structures corresponding to the response of ambient ions with different masses. The LPP was first imaged through the 460 nm filter in helium, neon, and argon background plasma and the images were compared. There was no significant variation in the structures or their emission intensities with the different ambient ions. The substantial differences in mass and number of lines within the filter's bandwidth lead

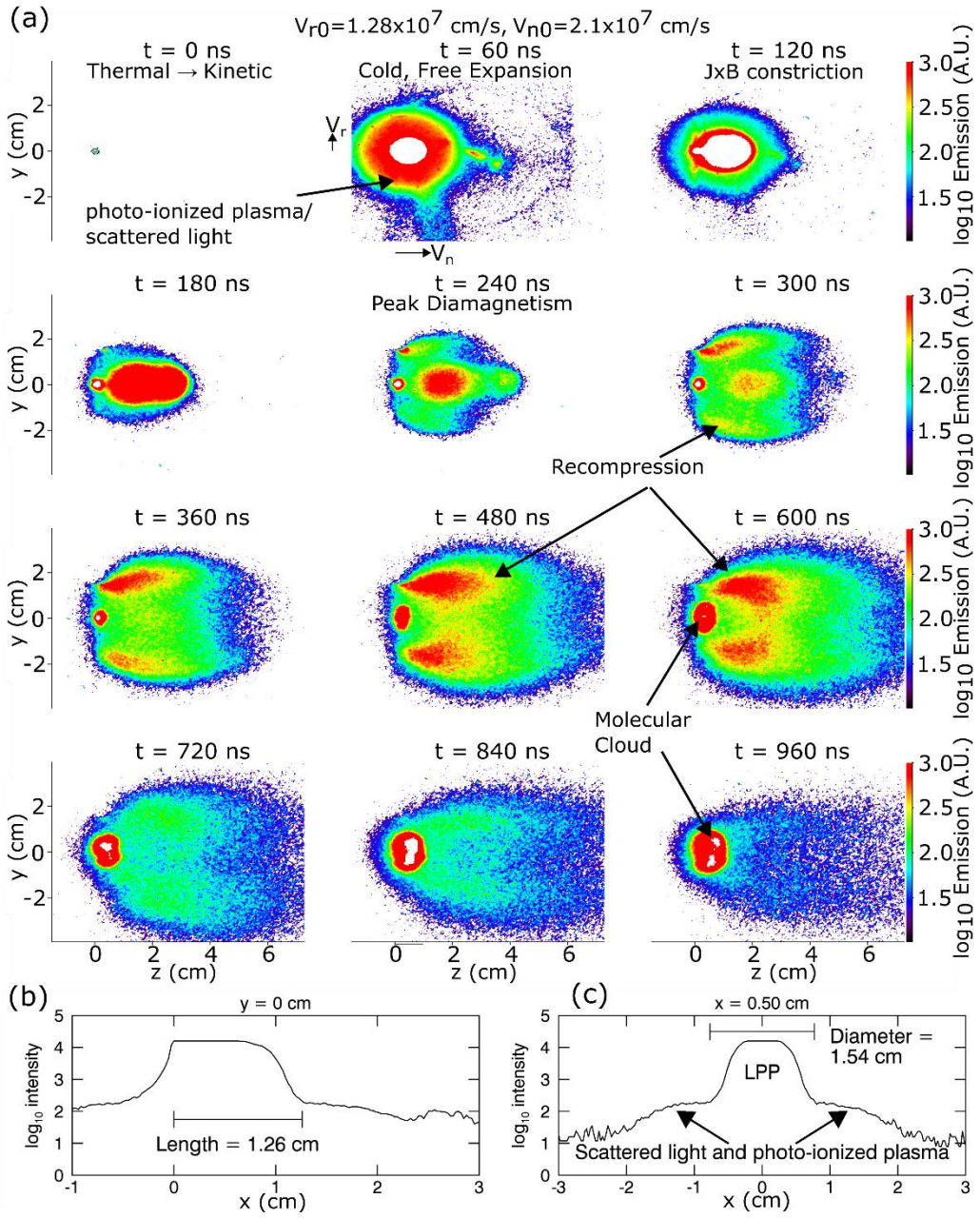

Figure 4.3: (a) False color imaging of the LPP through the 460±10 nm filter for various stages of the LPP evolution. White near $(y, z) = (0,0)$ and in the center of the LPP indicates saturated light intensity. Profiles of $t = 60$ ns emission for time of flight calibration of (b) V_{n0} and (c) V_{r0}.

immediately to the conclusion that the emission signal through the 10-nm HWHM filter is due primarily to carbon ions or continuous band emission. The likely sources of the emission are the C-III lines, continuum emission from recombination, or low-energy bremsstrahlung which are

more indicative of the LPP density and temperature such as in Fig. 4.1a but with more manageable signal intensities. With the integration time set at 30 ns, the evolution of the LPP emission through the 460 nm filter is shown in Fig. 4.3. The images are taken every 60 ns during the initial expansion and the indicated time set to the closing of the shutter and $t = 0$ ns is the end of the laser pulse. At $t = 60$ ns, the plasma has expanded enough to do time of flight measurements.

The saturated emission at $t = 60$ ns is due to the LPP while the bright halo around it is due to photo-ionized plasma and scattering of the intense light. There is an abrupt increase in the scale length variation of the emission between the saturated light of the LPP and the halo. This is shown more clearly in Fig. 4.3b&c. This change is taken as the LPP edge which yields velocities of $V_r = 1.28 \times 10^7$ cm/s across $\boldsymbol{B}$ and $V_n = 2.1 \times 10^7$ cm/s along $\boldsymbol{B}$. Since, $60 \text{ ns} = 0.25\tau_D$, the magnetic field has not removed significant momentum and energy from the LPP so that these time of flight measurements should be very close to the free expansion velocities or initial velocities, V_{r0} and V_{n0}. The value for V_{r0} is almost exactly that predicted in §3.2. For the ambient plasma density, V_{r0} is nominally Alfvénic, $M_A \sim 1$ while V_{n0} is initially super-Alfvénic.

At $0.5\tau_D \approx 120$ ns, the magnetic forces start to constrict the expansion as energy is lost to the electromagnetic fields. By $t = 240$ ns, the diamagnetic cavity is its largest cross-field extent and the half max of the emission stagnates as well. Compression effects start to appear at the LPP's cross-field boundary for $t > 300$ ns and the expansion becomes more like a jet expanding down the magnetic field.

The image for $t = 300$ ns shows diminished emission from the on-axis portion of the LPP and increased emission near the boundaries. This is what Fabre [27] described as the recompression stage of the evolution where the physical extent of the LPP across the field did not

significantly diminish but the LPP density appeared to collapse back on to the axis. For $t = 360, 480,$ and 600 ns, this process becomes even more pronounced within the LPP as the recompression region reaches the axis. This appears to occur the much slower rate of 5×10^6 cm/s. The recompression process itself may be a combination of a convective process and diffusive process so this recompression rate is not necessarily related to a flow speed of carbon ions within the LPP. In addition, Sudo [22] showed that the temperature distribution undergoes a similar reorganization where the internal thermal gradient begins to change direction for $t > \tau_D$. This "re-thermalization" that Sudo described is conflated with the particle convection described by Fabre as well as diffusive processes from finite electron resistivity to give the apparent inward motion of the plasma. The argument used to estimate the density gradient for $t < \tau_D$ does not apply late in time as it was predicated on a co-moving gradient in n_e and T_e, and for $t > 300$ ns, this is not guaranteed. Thus it is unclear how much of the movement of the light towards the interior in Fig. 4.3 for $t \geq 300$ ns is indeed particle motion or "re-thermalization" of the electrons.

During the recompression stage, a cloud appears about the laser focal point that expands at the even slower rate of $\sim 10^6$ cm/s but is not observed to get further than $z = 2$ cm which it reaches after 2 μs. By 1 μs, however, the LPP has recompressed across the field and diffused so much along the background magnetic field that much of the carbon may have already left the imaging region. This cloud that remains near the target is believed to be molecular components or carbon particulates in the debris which may just have a slow sound speed and were never significantly accelerated. Alternatively, they may be the part of the distribution of ions that were too slow and recombined within the high density region near the target. In any case, they seem to not have been a part of the main LPP-field interaction and are moving too slow to be of significant consequence to the evolution of the system.

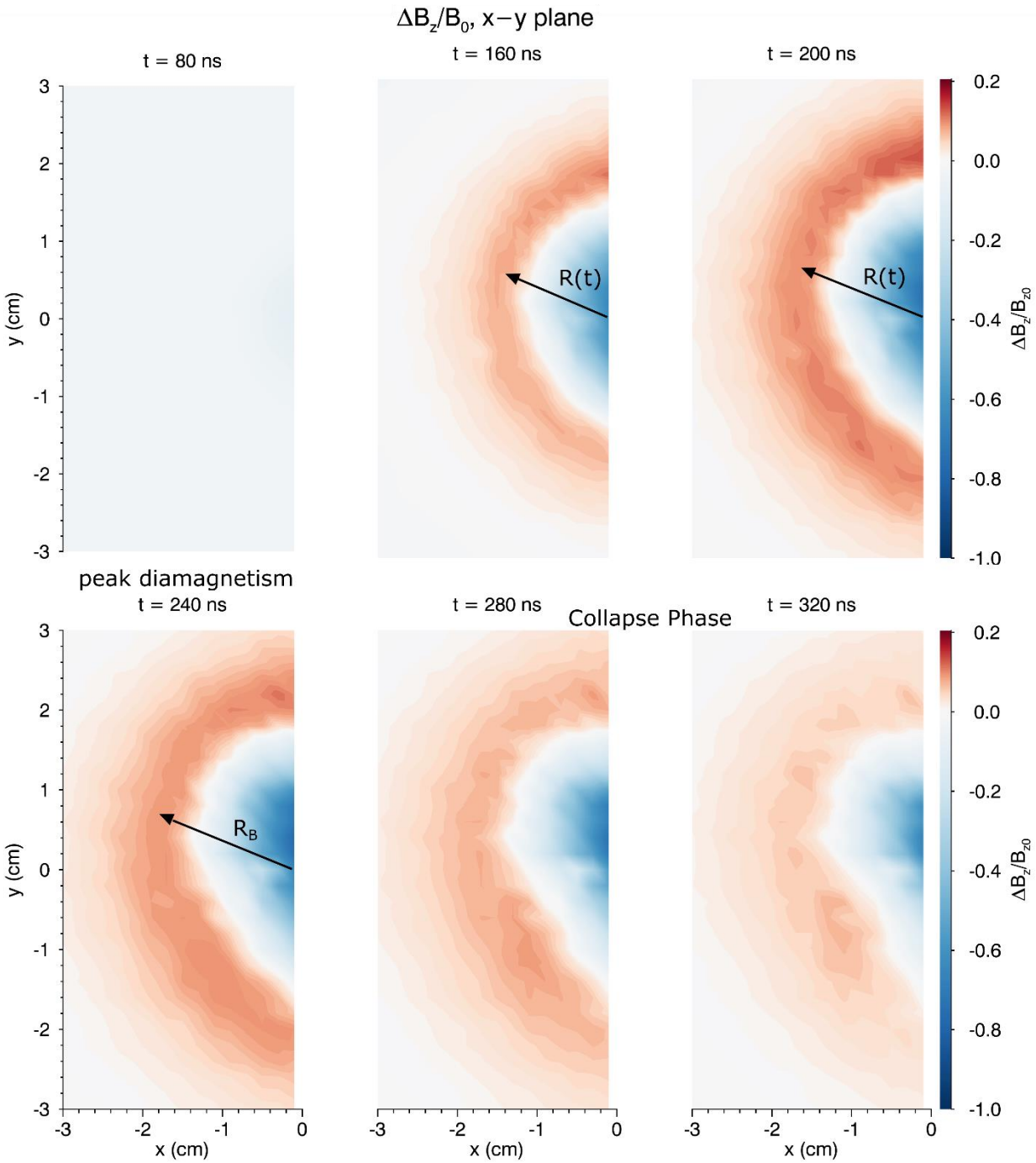

Figure 4.4: Magnetic field perturbation data relative to the ambient field strength taken in $x-y$ planes across the background magnetic field at $z = 2$ cm. Times distributed to capture characteristic features in the evolution of the expansion phases of the LPP including just prior to bulk LPP ions reaching the probe ($t = 80$ ns), peak diamagnetism ($t = \tau_D = 240$ ns), and just after onset of cavity collapse ($t = 320$ ns).

4.3—Magnetic Field Data

4.3.1—XY Data

Measurements at multiple positions were uncommon or of poor resolution in the earliest magnetic LPP experiments, but Collette [56] in a previous experiment in the LAPD presented volumetric data in three parallel $x-y$ planes for the case where $\boldsymbol{V}_n \cdot \boldsymbol{B} \approx 0$ as opposed to the present case of $\boldsymbol{V}_n \times \boldsymbol{B} \approx 0$. The addition of a linear motion of plasma across a uniform magnetic field results in an electrostatic field conflated with the induced electric field due to the motion of the diamagnetic cavity. This will be shown explicitly in §5.3. The advantages of re-examining this data for the present case include: (1) the global field evolution including the parallel boundary of the cavity through $t = \tau_D$ with the addition of a new probe drive that can extend further in z than that of [56], (2) measurement of the magnetic field at the locations at which the electrostatic field will be measured, (3) the benefit of the inherent cylindrical symmetry which also leads to a more accurate calculation of the induced electric field.

Shown in Fig. 4.4 are the data taken in the $x-y$ plane and offset 2 cm in z from the target. The magnetic field perturbations are normalized to the background magnetic field strength and the times shown are primarily to emphasize the main features of the expansion phase of the diamagnetic cavity. The first frame at $t = 80$ ns shows mostly an unperturbed magnetic field as only the fastest of the LPP ions, as measured by the time of flight velocity in §4.2.2, could have made it to the probe by this time. These ions have velocity vectors almost perfected aligned with the ambient magnetic field while the mechanism of §2.3 requires a mass flow across the magnetic field to produce the field expulsion. Nevertheless, there is a small magnetic field depression on axis of about 50 G ($\delta B/B_0 \sim 7\%$) with no accompanying compression of the field.

By $t = 160$ ns, the traditional picture of a diamagnetic cavity is appears. The field during all times does not reach full expulsion ($\max|\Delta B/B_0| \approx 80\%$) due to either the LPP not producing a strong enough current or the points of full expulsion occupy such a small volume near the center of the cavity that the speed of the expansion and size of the probe prevent its resolution. The cavity and compression expand together and each in a manner such that good cylindrical symmetry is maintained. The depth and height of the cavity and compression, once in view, do not exhibit a strong time dependence. Between 160 and 200 ns, for example, the peak in the magnetic field compression changes by less than 3% as a fraction of B_0 with a peak compression of 17%. The difference between 200 and 240 ns is even smaller indicating that the compression moves as a relatively stationary structure in time.

As peak diamagnetism is reached at 240 ns, it is clear the cavity has stopped expanding and it begins to develop a slight up-down asymmetry. This asymmetry persists as the cavity collapses for the late time evolution $t \geq 280$ ns but does not become worse with time. Instead, the compression begins to decrease in amplitude and the boundary of the cavity retreats to lower radii at a rate much slower than the expansion rate. Between 240 and 320 ns, the compression moves not more than 2 mm indicating a speed of collapse, $v_{col} < 5 \times 10^6$ cm/s $= 0.4 v_{exp}$. This suggests a temporal asymmetry between cavity formation and collapse that is consistent with the observed recompression in the filtered visible emission of Fig. 4.3. As argued in §2.2, the cavity itself may be propagating down the magnetic field. Data along the background magnetic field is necessary to see whether the cavity behavior just described is merely an effect of the cavity passing through the diagnostic plane or actual facets of the evolution.

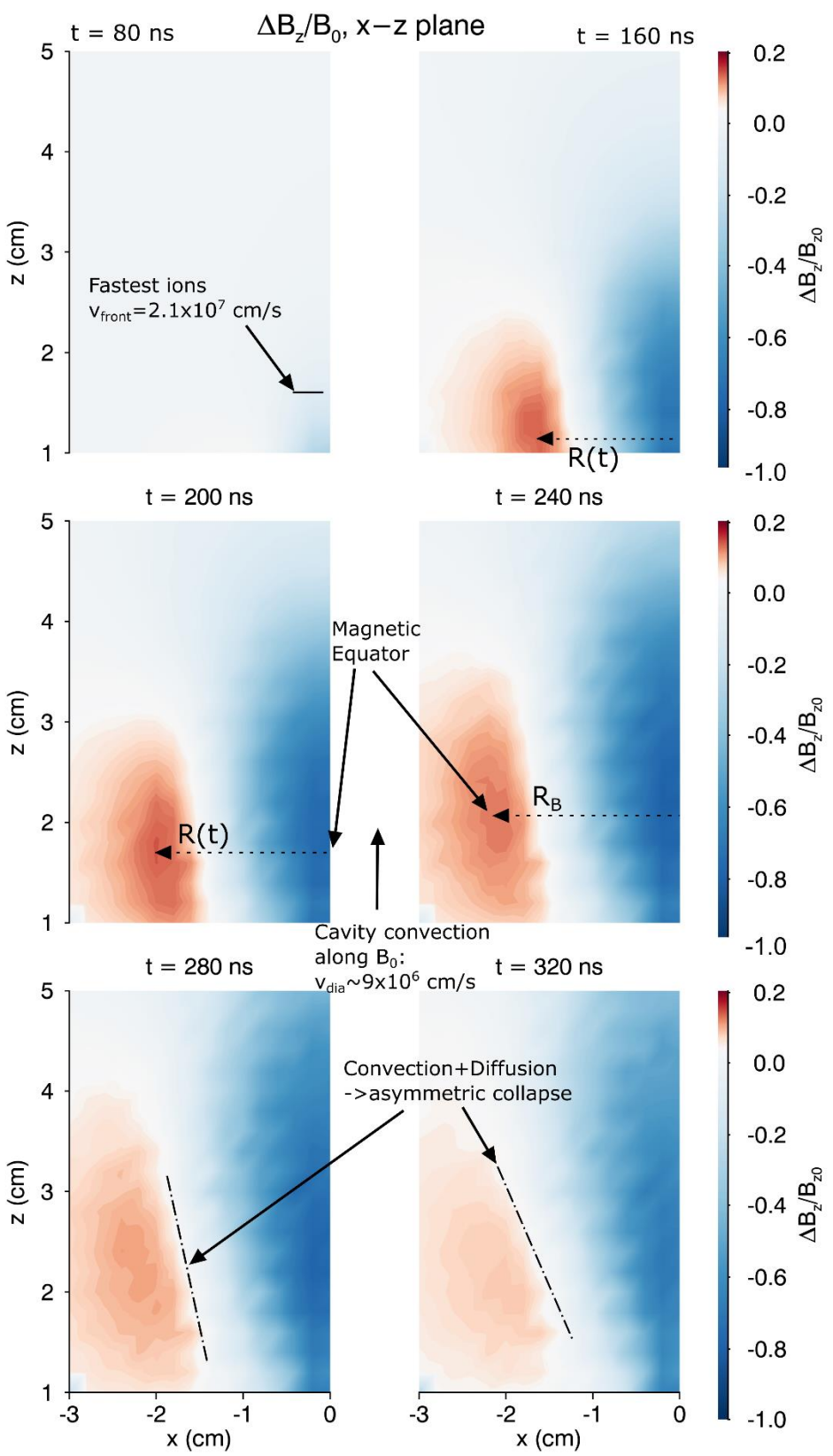

Figure 4.5: $\Delta B_z/B_0$ in $x-z$ planes at $y = 0$ cm. Conditions otherwise identical to Fig. 4.4.

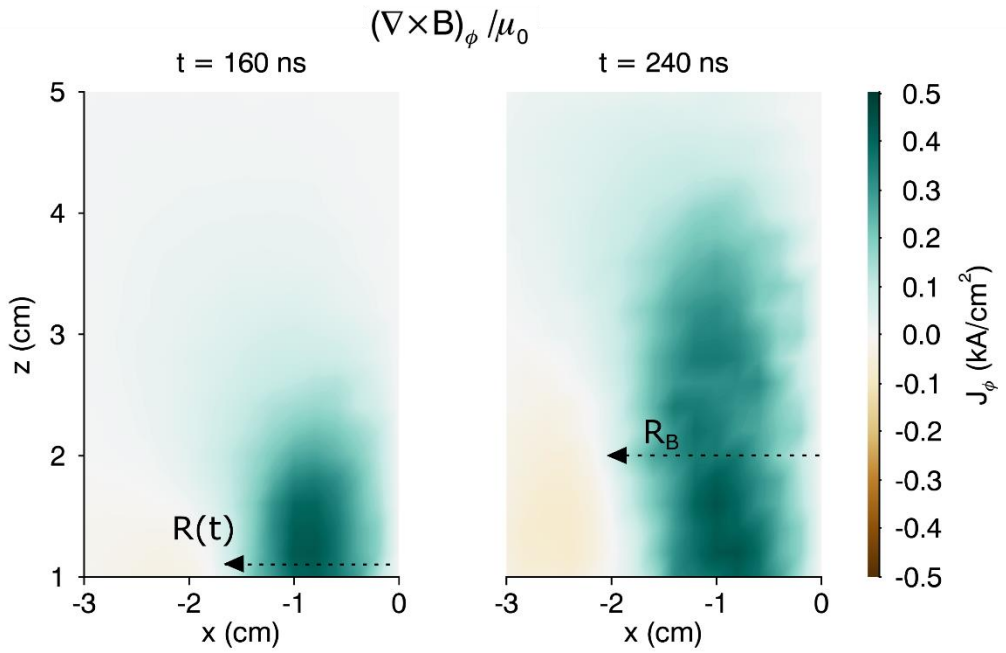

Figure 4.6: Azimuthal current $\mu_0 J_\phi = -\partial_r B_z$ of the diamagnetic cavity ($J_\phi > 0$) and compression ($J_\phi < 0$) as calculated by the x-z plane magnetic field data.

4.3.2—XZ Data

Figure 4.5 shows the $x - z$ plane measurements of the diamagnetic cavity. An obvious feature is the elongation of the cavity over time as it becomes more like a prolate spheroid as in Fig. 4.3. All the features described in Fig. 4.4 appear along with their clear variations along $\boldsymbol{B}_0$. The cavity follows the slight field expulsion that was noted at $t = 80$ ns in Fig. 4.4. The compression appears further behind in z from the front of the diamagnetic cavity and exhibits a "back end" where it decreases in amplitude as one moves closer to the target. This is most clear for $t \geq 200$ ns and suggests a symmetry axis along z. If the cavity were a spherical object being carried along with the mass flow of the expanding LPP, then the peak compression would indicate a magnetic equator or the symmetry plane of a dipole-like field. The equator here is the plane across the ambient magnetic field that contains the peak compression and also the center of the

diamagnetic cavity which co-moves with the LPP. The variation in z of the compression could simply be a $\sin^n \theta$ variation of the magnetic field in the frame of the diamagnetic cavity where n is some power to capture the sharpness of the variation. The example frequently applied to magnetized plasma explosions is that of a spherical, superconducting dipole which has $n = 1$ [21]. The increasing eccentricity of the cavity in time prevents any meaningful calculation or interpretation of such an index especially without an accurate positioning of the magnetic equator in time.

Figure 4.6 shows the color contours of the azimuthal current, J_ϕ calculated from $\mu_0 J_\phi = \partial_z B_r - \partial_r B_z$. At $t = \tau_D$, the radial boundary, $J_\phi = 0$ contour corresponding to peak magnetic compression, makes an almost straight line along $x = -2$ cm. Taking the z position of the peak compression as the location of the equatorial plane of the diamagnetic cavity during expansion, one can calculate the motion of the diamagnetic cavity in the direction of the background magnetic field. That is the velocity of the frame in which the diamagnetic cavity is approximately constant. This gives $v_{dia} \sim 9.0 \pm 1.0 \times 10^6$ cm/s. Note from the time of flight measurements that v_{dia} is within error equal to the initial difference between the normal and lateral velocities of the LPP coming off the target, $V_{n0} - V_{r0} = 8.2 \times 10^6$ cm/s. Additionally, $V_{n0}\tau_D = 5$ cm, which is the apparent extent of the diamagnetic cavity along the background magnetic field at $t = \tau_D$ in Fig. 4.5. This supports the model that the diamagnetic cavity can be treated as a structure that is tied to the center of mass of the LPP as it expands. Further, the geometry of an LPP expanding off a target means there is always a non-zero center of mass flow, $\boldsymbol{V}_m \neq 0$, so that the diamagnetic cavity should never be presumed to be stationary.

By tracking the diamagnetic equator in time, one can also calculate the function $R(t)$ which was important for the model in §2.3. The curve that is labelled 'Bonde' in Fig. 2.4 was

calculated by this method using the data from Fig. 4.5. The variables chosen to normalize the curve were R_0, V_{r0}, and R_B, the latter of which is shown in all $x-z$ data planes at $t=\tau_D$. The curve $R(t)$ in Fig. 2.4 seems almost to follow a curve uniformly offset from the ideal $R(t)$ determined by the Rayleigh model until the very end of the expansion. Note, however, that the expansion is very slow as it approaches peak diamagnetism and the 2 mm resolution of the probe gives a biased determination of the location of $R(t)$ toward the grid point with the smaller radius. Accounting for the 5% error from the 2 mm resolution in determining $R(t)$ and the normalization of R_B, the curves are essentially indistinguishable. The value quoted for β as 6×10^5 in §3.2 was determined from this curve.

4.3.3—Convective Collapse and Resistance

For $t>\tau_D$ there is a decoupling between the equator of the diamagnetic cavity and the compressed field. Specifically, two features appear: (1) the radial variation of the compression obtains a strong, asymmetric z dependence and (2) the compression ceases to propagate along z with the diamagnetic cavity. These indicate not only diamagnetic cavity collapse but also that the ambient magnetic field is diffusing back into the diamagnetic cavity. When the resistive term in Eq. 4.2 becomes significant, the motion of the plasma and that of the diamagnetic cavity need not coincide—they decouple. This does not mean the cavity ceases to convect along with the plasma but merely that the plasma motion and field motion are different. Without a direct measure of the motion of the ions and electrons within the LPP, there is no way to determine with certainty how much of the observed collapse is driven by convective collapse, or recompression of the plasma in the language of Fabre [27] or by diffusion. Equation 4.2 gives a method of qualitatively determining the importance of convection versus diffusion and even an estimation of T_e.

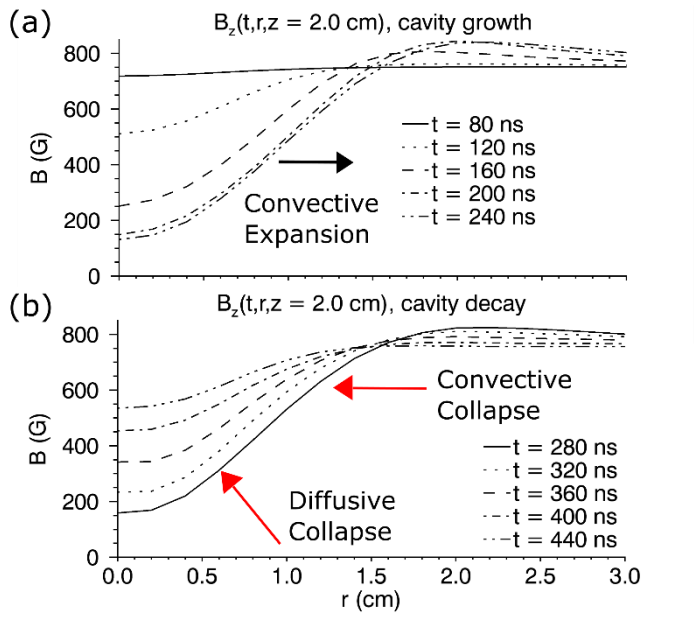

Figure 4.7: Magnetic field profiles versus time (a) during expansion and (b) during collapse.

Radial profiles of the magnetic field versus time at $z = 2$ cm are shown in Fig. 4.7. From Eq. 4.2, the primary difference between diffusion and convection in laminar fields is that field diffusion rates are proportional to profile curvature while field convection rates are proportional to $\nabla \boldsymbol{B}$ and $\boldsymbol{B}$. The profiles exhibit their largest curvatures on the axis of the expansion and at peak compression. The profile in between the two for $0.5 < r < 1.5$ is comparatively linear; diffusion only slowly affects these fields. That is, diffusion-dominated cavity collapse would tend to fill in the field from the bottom up on axis and leave the linear parts of the profile relatively unchanged. Convection-dominated collapse would cause a strong radially inward collapse of the profile. It is clear from a qualitative perspective that the cavity collapse is affected by both convection and diffusion. Without a measure of the LPP ions' velocities, the term $\boldsymbol{V} \times \boldsymbol{B}$ cannot be easily estimated in general. However, near peak diamagnetism, the LPP should be relatively stationary

across the magnetic field, $\boldsymbol{V} \times \boldsymbol{B} \approx 0$ so that an instantaneous estimate of the contribution from diffusion can be made and also the value of T_e corresponding to that diffusion.

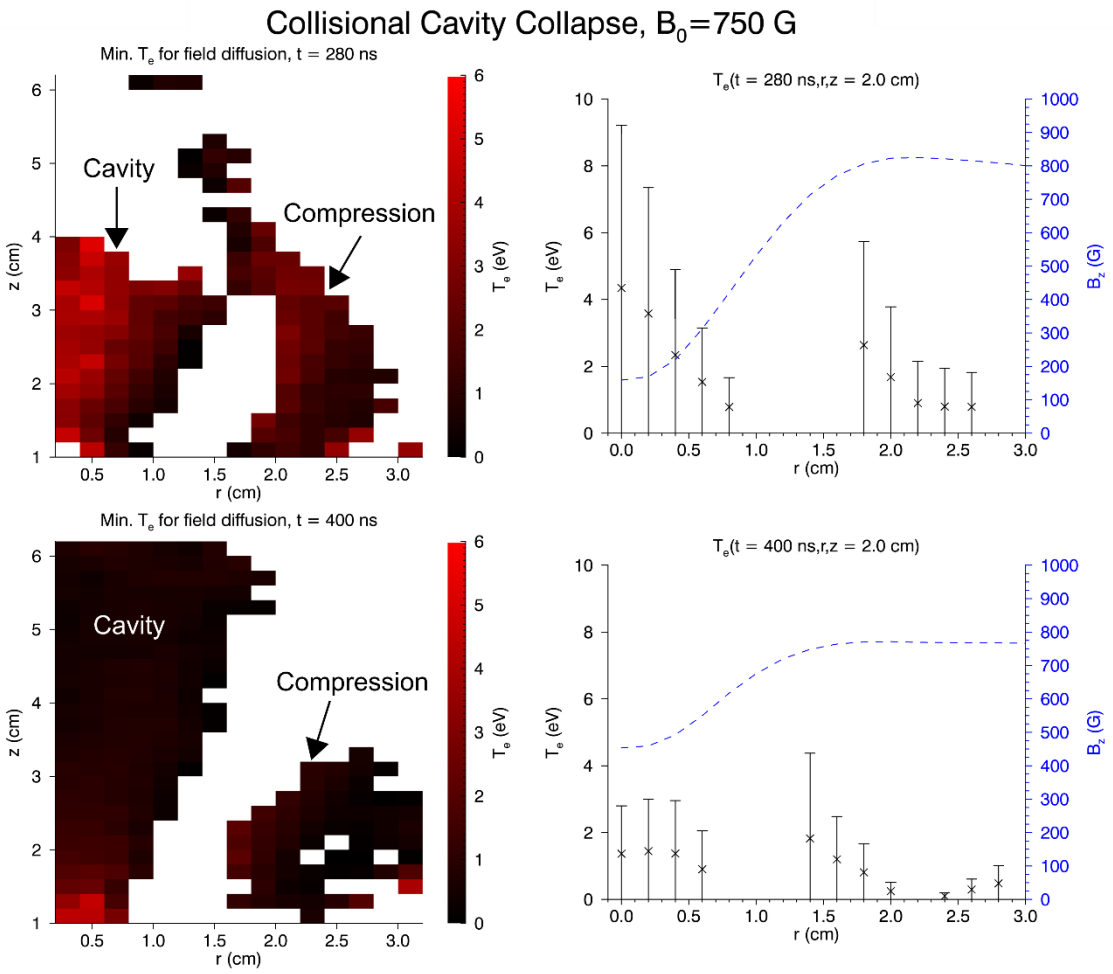

Figure 4.8: Estimated electron temperature variations in space and time using the magnetic field profiles of Fig. 4.5. White space indicates an insignificant $\partial_t B_z$ or clearly non-diffusive behavior; no T_e was calculated.

Figure 4.8 shows the estimated electron temperature assuming the magnetic field evolves entirely due to classical resistivity in the corresponding term of Eq. 4.2. If the rate of change of B_z was less than 3% of the cavity formation, no T_e was calculated as this represents an insignificant change in the magnetic field. Also points where $\partial_t B_z$ and $\nabla^2 B_z$ were of opposite signs were ignored. The time $t = 280$ ns corresponds close enough to peak diamagnetism to assume the

convection is not significant but far enough from peak diamagnetism to exhibit a change in the magnetic profile. Alongside the 2D image of the calculated temperature is a radial profile of the temperature at $z = 2$ cm and the corresponding magnetic field profile for reference. The points where the resistive contributions are expected to be largest—on axis and at peak compression—yield the largest estimated electron temperatures for the cavity and compression. Nevertheless, 5 eV is a fair upper bound on the instantaneous temperature of the LPP electrons in the cavity. Most of the diamagnetic cavity and compression regions indicate electrons of slightly lower temperature, $T_e \sim 1 - 3$ eV. This is still high compared to the model in Appendix A though far from unreasonable considering heating mechanisms outside of three-body recombination have been neglected. Sudo [22] found that several heating mechanisms, including compressional heating of electrons and resistive heating are likely important.

The same analysis is provided at a later time of $t = 400$ ns also in Fig. 8 to show any possible temporal evolution of T_e. The resulting T_e are lower, lying mostly in the range $0.2 - 2$. This would be too fast of a drop in temperature from 280 ns even if only three-body recombination heating is accounted for though the range is more consistent with the calculations of Appendix A. Collapse of the cavity by convection would artificially deflate this calculation of T_e. This implies that the values of T_e calculated at $t = 400$ ns are below the actual values. Conversely, these values of T_e are calculated from an equation that inflates the result and is very sensitive to errors in $\partial_t B_z$ when it is small. With this in mind, points in the magnetic field where it is approximately stationary in time—due to either stagnation at the radial boundary or balance between convection and diffusion at the parallel boundary—have an artificially high value of T_e . This behavior is more prevalent at $t = 280$ ns than at $t = 400$ ns since there are spatial regions in the former where field is still being expelled by convection of the LPP along the magnetic field. The values for T_e in these

regions should only stand as a rough approximation. Under the circumstances and barring a more accurate method of determining T_e, the electron temperature can reasonably be taken as 3 ± 2 eV near and after $t = \tau_D$.

4.3.4—Connection to Collisionless Coupling

The values do provide two valuable insights. First, the collapse of the diamagnetic cavity can be explained with a more classical picture of diffusion than has been reported in the past as anomalous resistivity [57, 58]. The results of anomalous diffusion of the cavity have all been claimed under the neglect of convective collapse and improper accounting of the temporal evolution of T_e and sensitivity to its magnitude. Specifically, the 3/2 power dependence in the resistivity of a quantity that varies as $t^{-\alpha}, \alpha > 1$ is a surprisingly strong dependence. All of these play some role in the evolution of the magnetic field and should never have been ruled out or neglected.

A second insight is that the combined data of §4.2.1, 4.3.2, and T_e gives an estimation of the contributions from the terms $\eta \boldsymbol{J}$ and $\nabla p_e / e n_e$ to $\boldsymbol{E}$ in Eq. 4.1. A characteristic current in the sheath region of the diamagnetic cavity is $J_\phi \sim 350$ A/cm^2 which appears when the magnetic field is at a strength of 550 G. The contribution of $\eta \boldsymbol{J}$ is primarily in the azimuthal direction, that is it takes away from the induced electric field, and for $T_e = 1$ and 5 eV, it is 43 V/cm and 3.8 V/cm, respectively. The latter value is effectively negligible compared to the $\boldsymbol{V} \times \boldsymbol{B}$ contribution which peaks at 110 V/cm for $t \ll \tau_D$. This would corroborate the neglect of a direct effect of resistivity in the Rayleigh model of the diamagnetic cavity. The value corresponding to 1 eV would amount to a significant change in the dynamics and is more consistent with the observed asymmetric decay of the diamagnetic cavity in time and space as it relaxes the magnetic field gradient as it competes

with convection. The true value of the contribution of $\eta \boldsymbol{J}$ to $\boldsymbol{E}$ would be placed at some intermediate value. Unfortunately, η is very sensitive to T_e, and no better determination of its value is presently available.

The pressure contribution, on the other hand, is less dependent on the value of T_e and amounts to only $2-10$ V/cm for $T_e = 1$ and 5 eV. The Hall term is approximately 240 V/cm assuming $n_e = 5 \times 10^{13}$ cm^{-3}. The value of n_e was taken from Fig. 4.1b but is also consistent with the LPP scaling laws and expansion model of Appendix A. The value for the Hall term is consistent with the Rayleigh model for the present parameters which gives $150-300$ V/cm depending on the electron density. Accounting for a 50% error bar in n_e still brings $\nabla p_e / e n_e$ nowhere near the value of the Hall term. This justifies the neglect of the pressure gradient in the Rayleigh model. It also corroborates the basic mechanism of diamagnetic cavity formation which is inherently different from that of an equilibrium plasma.

The traditional mechanism of diamagnetism in an equilibrium plasma for which the ∇p drift plays the dominant role and has thus been named *the* diamagnetic drift. In high-β expansions, this drift plays a vanishingly small role and $\boldsymbol{E} \times \boldsymbol{B}$ drives the current in the diamagnetic cavity. This is why it was important to point out the error that appears frequently in the literature that an equilibrium with $\beta_{th} = 1$ exists at the edge of the LPP. Such an equilibrium does not exist here.

Using the magnetic field and imaging data, it has been shown that the Ohm's law description of the magnetized LPP expansion is essentially

$$\boldsymbol{E}_{\text{ind}} + \boldsymbol{E}_{st} = -\boldsymbol{V} \times \boldsymbol{B} + \frac{\boldsymbol{J} \times \boldsymbol{B}}{e n_e}.$$

What remains then is the confirmation of this relationship by looking directly at the electric fields.

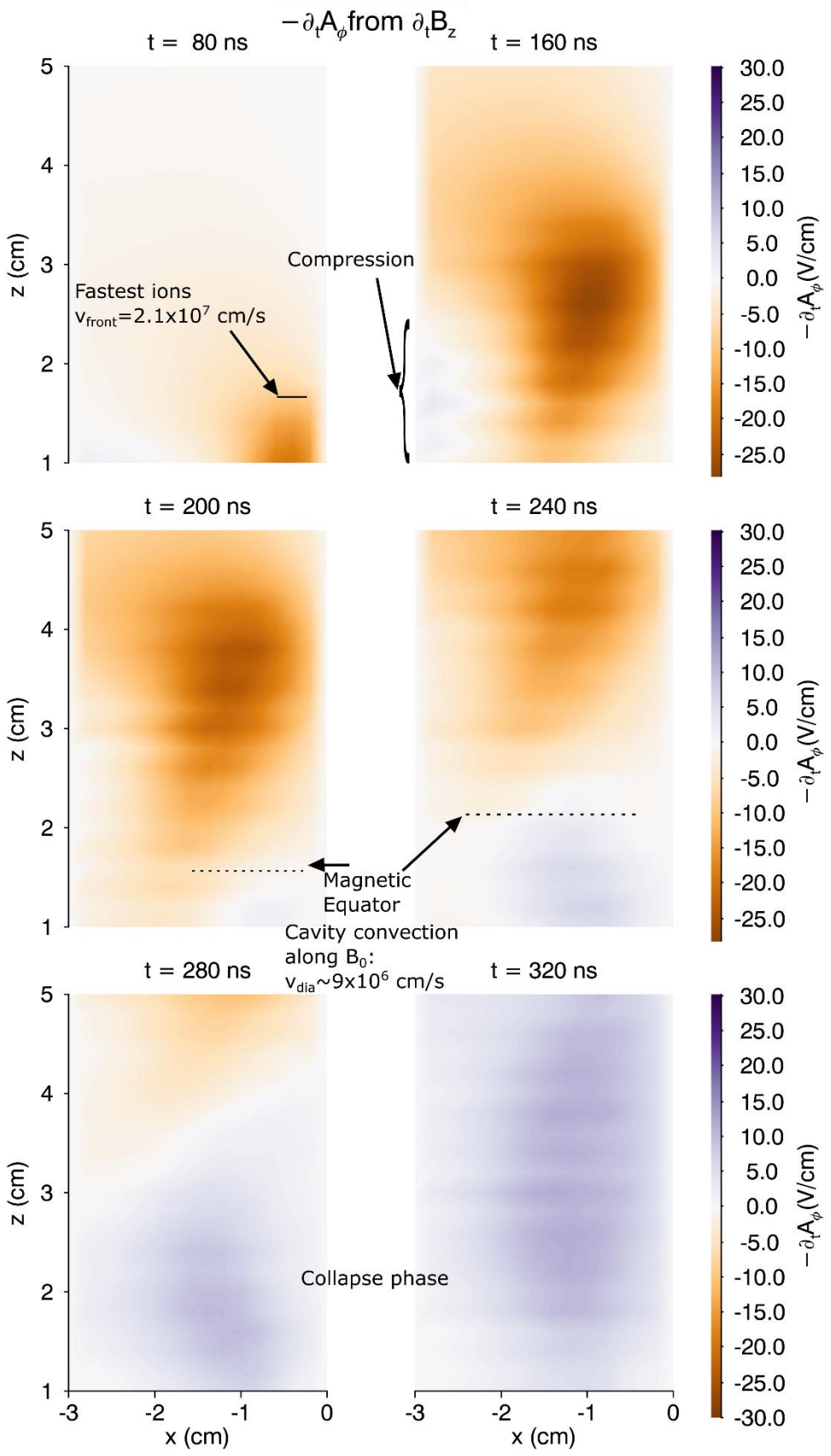

Figure 4.9:

Induced electric field in the azimuthal direction for the times and magnetic fields corresponding to Fig. 4.5.

4.4—Electric Fields

4.4.1—Induced Electric Field

With the approximations outlined in the experimental setup section, the induced electric field in the azimuthal direction was calculated using the radial profiles from the $x-z$ plane data of the magnetic field in Fig. 4.5. The induced electric field is shown in Fig. 4.9 in a manner identical to Fig. 4.5. Though the curl operator in cylindrical coordinates places a small shift in the location of the edge of the cavity, the orange coloring corresponds to field removal while purple is associated with the magnetic field compression. Since both the diamagnetic cavity formation and compression formation are the transfer of energy from particles to the field, $\boldsymbol{J}\cdot\boldsymbol{E}$ must be less than zero where magnetic field is being expelled or compress. The structure of the induced field in Fig. 4.9 and the azimuthal current in Fig. 4.6 both switch sign with the compression and expulsion of Fig. 4.5. This shows their calculation is consistent with the energy transfer process.

As the cavity expands and moves the field, the induced field strength diminishes from -30 V/cm at $t=160$ ns to -15 V/cm and -10 V/cm at $t=200$ ns and $t=240$ ns, respectively. The shape of the electric field is maintained as it flows along with the LPP mass. The magnetic equator of the diamagnetic cavity comes into view after $t=120$ ns but is not visible in Fig. 4.9 due to the radius of the cavity still expanding and expelling magnetic field. By $t=240$ ns, the radius of the equator has stagnated and can be seen very clearly by the boundary between orange and purple in that frame. If the cavity were simply moving with the LPP mass, the field profile would fill in behind the cavity causing the appearance of the reverse induced electric field. The field strength is slightly smaller behind the equator ($\approx +5$ V/cm) due to the cumulative diffusion of the field from $\eta\boldsymbol{J}$. This term acts against the convective expansion and complements the convective collapse. The

magnetic probe places this distinct reversal region at $z = 2.2$ cm. This is extremely close to the motion of the peak compression along z and that of the LPP, $(V_{n0} - V_{r0})\tau_D \approx v_{dia}\tau_D = 2.16$ cm. By $t = 280$ ns, the collapse phase is setting in but part of the diamagnetic cavity is still flowing along with the LPP maintaining a negative induced electric field at the front of the cavity. This is also the region at the front of the cavity that gave a suspiciously large value of $T_e \sim 10$ eV in Fig. 4.8. It is especially clear now that those large values of T_e are erroneous because the magnetic field is not even collapsing! Full-collapse of the cavity is evident by $t = 320$ ns with characteristic induced electric field magnitudes of about $10 - 12$ V/cm.

From $\boldsymbol{V} \times \boldsymbol{B}$ estimates and using the initial radial velocity of the LPP, the maximum induced electric field in the diamagnetic cavity should be on the order of 110 V/cm. There are three reasons why this maximal field strength is not be observed in the present case.

First, the maximum field is located at the outer radius of the equator of the diamagnetic cavity where the mass velocity has its largest value across the ambient magnetic field. From estimates of the speed with which the equator reaches the diagnostic plane, the equator is visible for times $t > 120$ ns $= \tau_D/2$. This is precisely the period of time in which the magnitude of the induced electric field from the Rayleigh model begins to drop dramatically (see Fig. 2.5) due to the deceleration of the cavity edge, that is $\partial_t R < V_{r0}$.

Second lies in the field profiles. Both $\boldsymbol{V}$ and $\boldsymbol{B}$ must necessarily have variations in r and z where there is a fall-off in the magnitudes of both as one moves away from the equator and closer to the axis. In fact, only ideal models suggest that $\boldsymbol{V}$ acquires its maximum value at $r = R(t)$ which requires that the ions stop in an infinitesimally small space since the force slowing it down is 0 at $r = R(t)$. Thus, the maximum value of $\boldsymbol{V}$ in a realistic profile occur for $r < R(t)$ where the

magnetic field is reduced. Therefore, most of the volume of the diamagnetic cavity has $\boldsymbol{V} \times \boldsymbol{B} < V_{r0}B_0$ and likely substantially less. Combined with the inability to measure closer to the target than $z = 1$ cm where $\partial_t R = V_{r0}$, these reasons ensure that the peak value of 110 V/cm is never actually measured.

4.4.2—Coupling from $\boldsymbol{E}_{ind}$

The observed behavior of the induced electric field within a diamagnetic cavity suggests a rather different model of coupling of these fields to ambient plasma. Attempts to analyze the coupling of a rapidly expanding plasma into a magnetized environment have been done by making quite a few approximations; understandably so. The most common approximation has been to assert that the coupling is mostly due to the induced electric field [59, 60, 61], observe from simulations that such is the case [62,63], or apply a model such as MHD that limits the electrostatic field to those with translational mass flows through $\boldsymbol{E} = \boldsymbol{V}_m \times \boldsymbol{B}$ [64]. In such models, the ambient ions are swept up by performing $\boldsymbol{E} \times \boldsymbol{B}$ drift in the induced electric field which eventually causes an ion outflow. Three problems exist with this model.

First, with large gradients in the magnetic field, the ions do not necessarily perform any standard drift motion. Those drifts require the field to be sufficiently uniform and steady. For the uniformity requirement, note that the parameter R_B^3/R_m^3 (see end of §2.3) can be rewritten as

$$\frac{R_B^3}{R_m^3} = M_A^2 = \frac{Z_a^2 e^2 n_{ai}}{\epsilon_0 m_{ai} c^2} \frac{m_{ai}^2 V_{r0}^2}{Z_a^2 e^2 B^2} \approx \frac{\rho_{ai}^2}{R_B^2} \frac{R_B^2 \left(\omega_{pi}^a\right)^2}{c^2}$$

where $\rho_{ai} = V_{r0}/\omega_{ci}^a$ is the directed Larmor radius of an ambient ion if it were swept up by the expansion and c/ω_{pi}^a is the ambient ion skin depth. The magnetic field scale length is much smaller than R_B, but R_B is used as a proxy for its order of magnitude. This suggests that in the spatially

non-uniform fields, $R_B \gg c/\omega_{pi}^a M_A$ is necessary to apply drift motion since then $\rho_{ai} \ll R_B$. This condition implies highly magnetized, dense, and slowly expanding cavities have more drift-like response of the ambient ions. Two of these three conditions are characteristics of a low-β expansion. The steady field requirement simply leads to $\tau_D \omega_{ci}^a \gg 1$. This, too, implies that slow, highly magnetized expansions, or low-β, have more drift-like response of the ambient ions.

The calculations made by [59, 60, 61] and those that cite them and their "Larmor coupling" model, as the drift models have been named in the literature, take some form of the limits $1 \ll \rho_{ai}/R_B, \tau_D \omega_{ci}^d, \tau_D \omega_{ci}^a \to \infty$. For most magnetized LPP expansions and diamagnetic cavities in space (AMPTE had $\omega_{ci}^d \tau_D \approx 1$), $\tau_D \omega_{ci}^d$ was less than or on the order of 1. This implies the ambient ions would have to be orders of magnitude larger in charge to mass ratio than the debris to approach a drift-like response. Essentially, the Larmor and induced electric field coupling models apply to a very limited class of expansions that have not been produced experimentally.

Second, the diamagnetic cavity necessarily collapses for $t > \tau_D$ and a large portion of the electromagnetic energy never escapes farther than R_B across the magnetic field from the source. This limits the amount of time the fields can accelerate ions and even more severely limits the number of ions it can accelerate since this number is proportional to the volume covered during the expansion of the cavity. The collapse also implies that the induced electric field reverses sign as is quite evident in Fig. 4.9. Ions that are accelerated by $\boldsymbol{E}_{ind}$ also get partially decelerated by it if they do not also escape the diamagnetic cavity prior to collapse.

This also leads to the third problem with coupling from the induced electric field, namely the fact that the compression itself is observed in Fig. 4.9 to correspond to a reversal in the sign of the induced electric field. Thus, ions that are accelerated outward by the induced electric field of

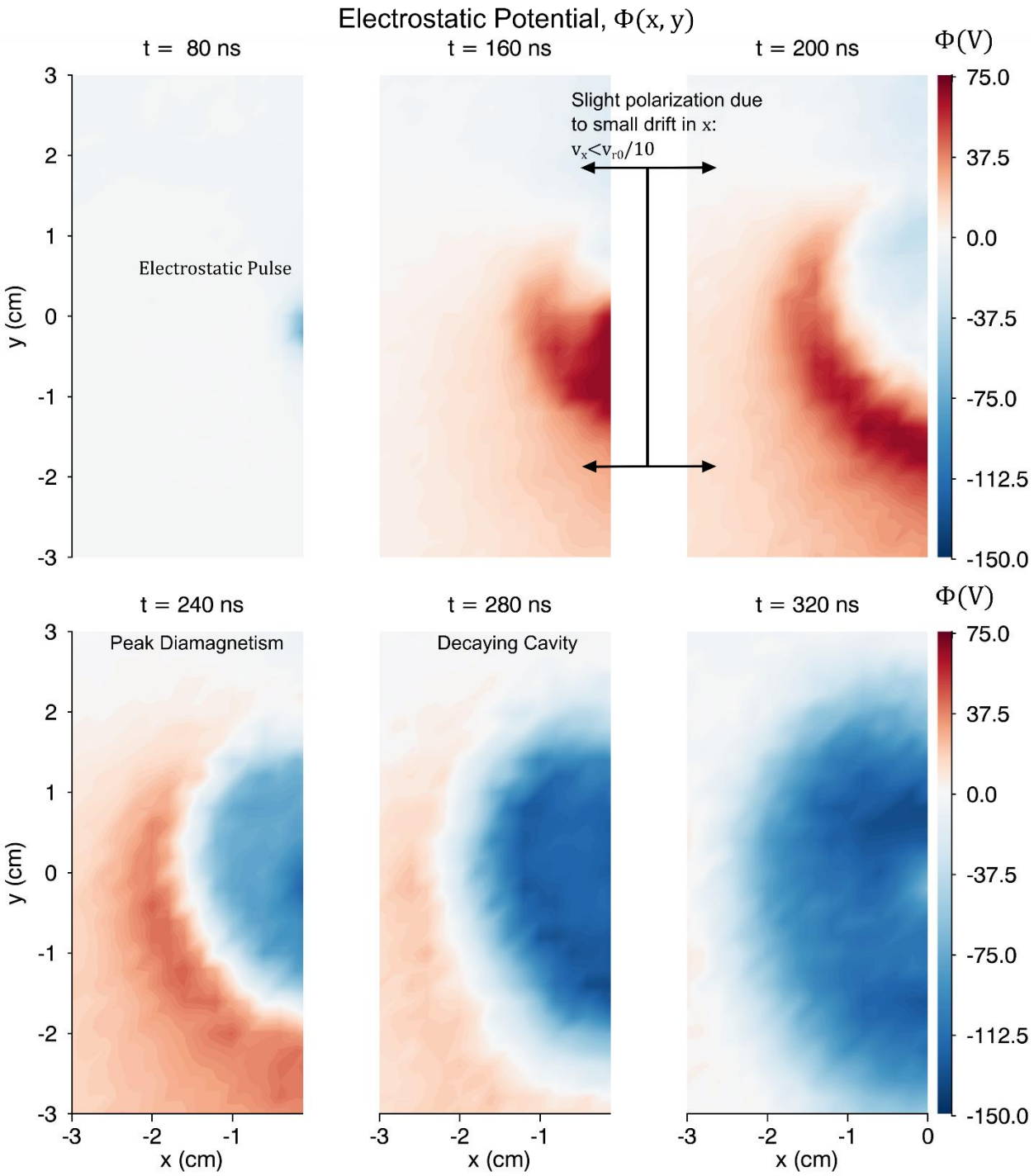

Figure 4.10: Electrostatic potential measurements in $x - y$ plane at $z = 2$ cm for times corresponding to Fig. 4.4

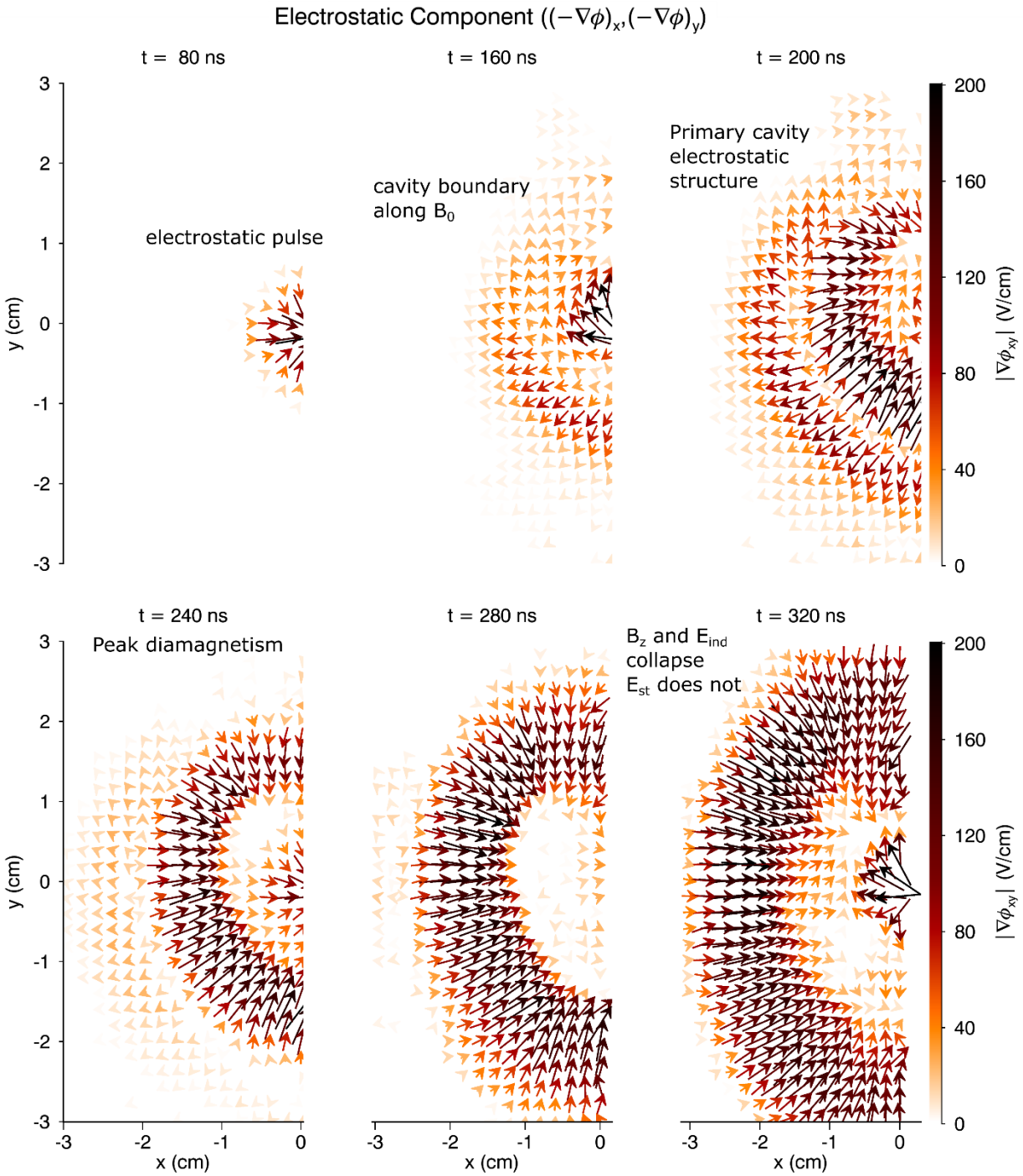

Figure 4.11: Electrostatic field data in an $x-y$ plane located at $z = 2$ cm for the times corresponding to that of Fig. 4.4.

the cavity are decelerated by the compression's induced electric field. For shocks this effect is actually desirable as it transports the energy to the front of a shock and keeps it moving outward. The problem lies more in the small spatial scales over which this change occurs. This limits the ability to generate an outward mass flow since orbital motion does not have time to build up during the passage of the narrow compression and sheath layers. Models that assume a drift motion overestimate the efficiency of the coupling. That being said, the reversals in the induced electric field may in some limit become of negligible concern and the most obvious limit available and implied by Larmor coupling models is $\tau_D \omega_{ci} \rightarrow \infty$. This is also the limit where the electrostatic field may be neglected in the Rayleigh model. As will now be shown, this is far from the present case.

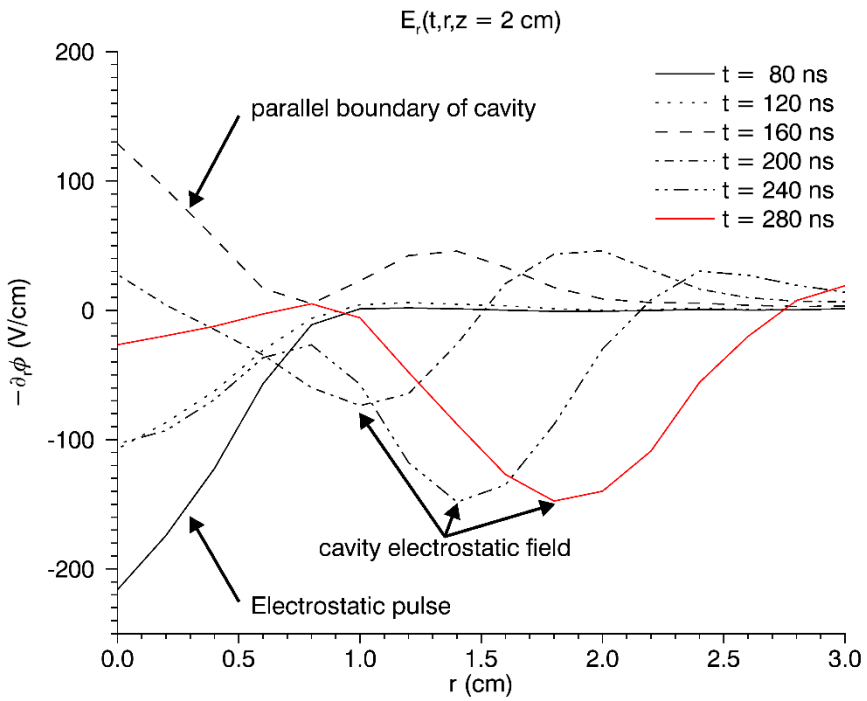

Figure 4.12: Radial variation of the electrostatic field as taken from Fig. 4.11 along $y = 0$ cm.

4.4.3—Electrostatic Field

Based on the model described in §2.3, the expected maximum magnitude of the electrostatic field in the diamagnetic cavity is 390 V/cm for $Z_d = 2$ and 240 V/cm from an estimation of the Hall term using magnetic field measurements and electron density estimates. This would be a substantially larger electric field in $\boldsymbol{E}_{st}$ than $\boldsymbol{E}_{ind}$. The emissive probe provides us with a direct measure of the electrostatic potential, ϕ_{meas}, from which $\boldsymbol{E}_{st} = -\nabla\phi_{meas}$. Figures 4.10 and 4.11 show the electrostatic potential and field in an $x - y$ plane in positions identical to the magnetic field measurements of Fig. 4.4 and the induced electric field in Fig. 4.9.

The salient features of Fig. 4.11 are that structures similar to those observed in the magnetic field of Fig. 4.4 exist in the electrostatic field. The diamagnetic cavity indeed has a strong, inwardly directed electrostatic field but there is also a field reversal during the expansion phase ($t \leq 240$ ns) that corresponds to the region of magnetic field compression. Both of these fields decay along with the diamagnetic cavity and the field compression for $t > \tau_D$. To clearly show the radial variation of the electrostatic field, a sample of radial profiles at different times for $z = 2$ cm are shown in Fig. 4.12. The inward field peaks in strength at $t = \tau_D = 240$ ns with 180 V/cm at about $r = 1.3$ cm. This strength is slightly smaller than the estimated Hall term and much smaller than the scale value of the electrostatic field in the Rayleigh model (Appendix §B.2). Accounting for the experimental profile, the Rayleigh model predicts 270 V/cm at $r/R_B = 0.6$ where the measured field peaks. This measured field is stronger than the maximum possible induced electric field and 6-20 times larger than those measured in Fig. 4.9. The outward component of the electrostatic field is significantly weaker but still strong in comparison to the corresponding induced electric field located at the magnetic compression. Its peak value is almost 60 V/cm around $t = 200$ ns but begins to fall as the cavity rapidly decelerates. As the cavity begins to

collapse, the outward field becomes smaller and is all but gone at $t = 280$ ns. The region where the electric field switches sign along the magnetic equator corresponds well to the point of peak magnetic compression to within error of the measurement grid.

In addition to the estimates of electron density from unmagnetized LPP expansion models in Appendix A and the rough estimate of Abel-inverted imaging in §4.2.1, the proportionality constant between the $\boldsymbol{J} \times \boldsymbol{B}$ force and the electrostatic field should predict the electron density which makes them fully consistent. Their ratio yields an electron density of 7×10^{13} cm^{-3}. This is just within the 50% error margin assumed in the LPP expansion model and used to get 5×10^{13} cm^{-3} in §4.2.1. The estimates from the unmagnetized expansion model yield values closer to $3 - 4 \times 10^{13}$ cm^{-3} with the initial assumption of 8×10^{15} electrons. It is clear from Fig. 4.1b that there is a density peak behind the cavity edge that is about a factor 2 higher than at the cavity edge. This pile-up is a reasonable explanation for small difference between the calculation of the Hall term and $\boldsymbol{E}_{st}$. This is what was described by Fabre [27] as the recompression of plasma. Furthermore, it is frequently noted in experiments that have density measurements, which has thus far only been possible in highly magnetized, $\beta < 10^3$, expansions, a region of compressed density forms behind the outer edge of the expansion [22, 65, 66].

For the outward electrostatic field, the ratio of $\boldsymbol{J} \times \boldsymbol{B}$ to $\boldsymbol{E}$ yields a density of about 4×10^{13} cm^{-3}. No model exists for how the outward electrostatic field is related to the $\boldsymbol{J} \times \boldsymbol{B}$ force in the compression, especially since it is often attributed to finite electron pressure effects [67]. This result suggests that the electrons in the LPP itself are responsible for the formation of the compression since the ambient plasma density is almost 10 times smaller. If the finite electron pressure contribution to $\nabla\phi$ is accounted for, its contribution is also outward. This means an even higher electron density is needed to account for the magnitude of the outward electrostatic field.

An important connection to the discussion of the magnetic field structure is the electrostatic field for the collapse phase of the cavity, that is $t \geq \tau_D$. For these times, the magnetic field structure is diminishing in strength through some combination of convection and diffusion of the magnetic field. The diffusion properties were discussed and shown to be consistent with an electron temperature on the order of 1 eV while the convection component of the collapse could not be ruled out. The electrostatic field remains on the order of 100 V/cm and continues to expand outward after peak diamagnetism, and eventually reaching 150% the largest size of the cavity. Since the electrostatic field acts against the outward momentum of the carbon ions, it stands to reason that if it is still present after peak diamagnetism when $\partial_t R = 0$, the carbon ions are accelerated inward. If the collapse of the diamagnetic cavity is influenced by material convection, then the electrostatic field is the clear source. Further, since the field maintains its strength, the carbon could regain a large portion of its initial energy. That is, the energy that went from the carbon to the field goes largely back to the carbon. The asymmetric decay of the cavity in time ensures that this processes is far from fully reversible and energy will be converted so some form other than kinetic energy of the ions. Assuming a simple linear decay of the electrostatic field from peak diamagnetism and noting the strength drops below 25 V/cm at $t = 600$ ns, a carbon ion could collapse onto the axis with a speed of $V_r = -5.7 \times 10^6$ cm/s. That is, it can recoup about 1/4 of its energy in directed motion. Note that this speed is also consistent with the observed recompression of the plasma in Fig. 4.3.

4.4.4—The Electrostatic Pulse, Parallel Boundary, and Charge neutrality

The field structure indicated at the times $t = 80{,}160$ ns of Fig. 4.11, do not conform to a simple Hall field, i.e. $\boldsymbol{E}_{st} = \boldsymbol{J} \times \boldsymbol{B}/en_e$, of the diamagnetic cavity. About 50-60 ns after the laser generating the LPP fires, a sharp drop in potential is observed. This potential well is highly

localized in space with a full-width half-max of only about 0.8 cm centered on the axis of the expansion. The potential drops on a time scale of about 5 ns and remains until the front of the LPP reaches the probe tip. At this point, there is a large swing in the electrostatic potential which goes back to zero, overshoots and eventually gives way to the diamagnetic cavity.

This potential structure which gives rise to the electrostatic field seen at $t = 80$ ns in Fig. 4.11 is coincident with the appearance of the small, on-axis diamagnetism of about 50 G that seemed to precede the LPP in Fig. 4.4. Not very many ions are expected to be at this position and if they are, their pitch angle would be so small that their perpendicular velocity could not account for a diamagnetic effect in the same way that the primary diamagnetic cavity forms in the bulk LPP. In the bulk LPP, the cavity formation process can be succinctly described as the series of steps: (1) ion outflow leads to charge separation, (2) with net charge, an electrostatic field appears, and (3) electron current within the electric field expels magnetic field. The presumed state of the ions at the furthest reaches of the LPP is such that (1) does not occur, but if an electrostatic field already exists, the ions need not have an outflow to generate a significant drop in magnetic field. The electrostatic field shown in the $t = 80$ ns frame becomes as large as 100 V/cm. This is on the same order of magnitude as the electrostatic field of the diamagnetic cavity. Within the diamagnetic cavity, the electric field sets the drift velocity of the electrons and therefore the current is simply this drift times the density. The small perturbation in the magnetic field associated with this electrostatic structure could simply be a result of the reduced electron population in front of the LPP. A field of 180 V/cm is enough to remove 80% of the background field but in front of the LPP, the density is just that of the ambient plasma, which is about 5 times less dense at $t = \tau_D$. A field half as strong as that inside the LPP would cause about 1/10th of the diamagnetic effect in the background plasma which would be approximately 60 G. It therefore seems that the diamagnetism

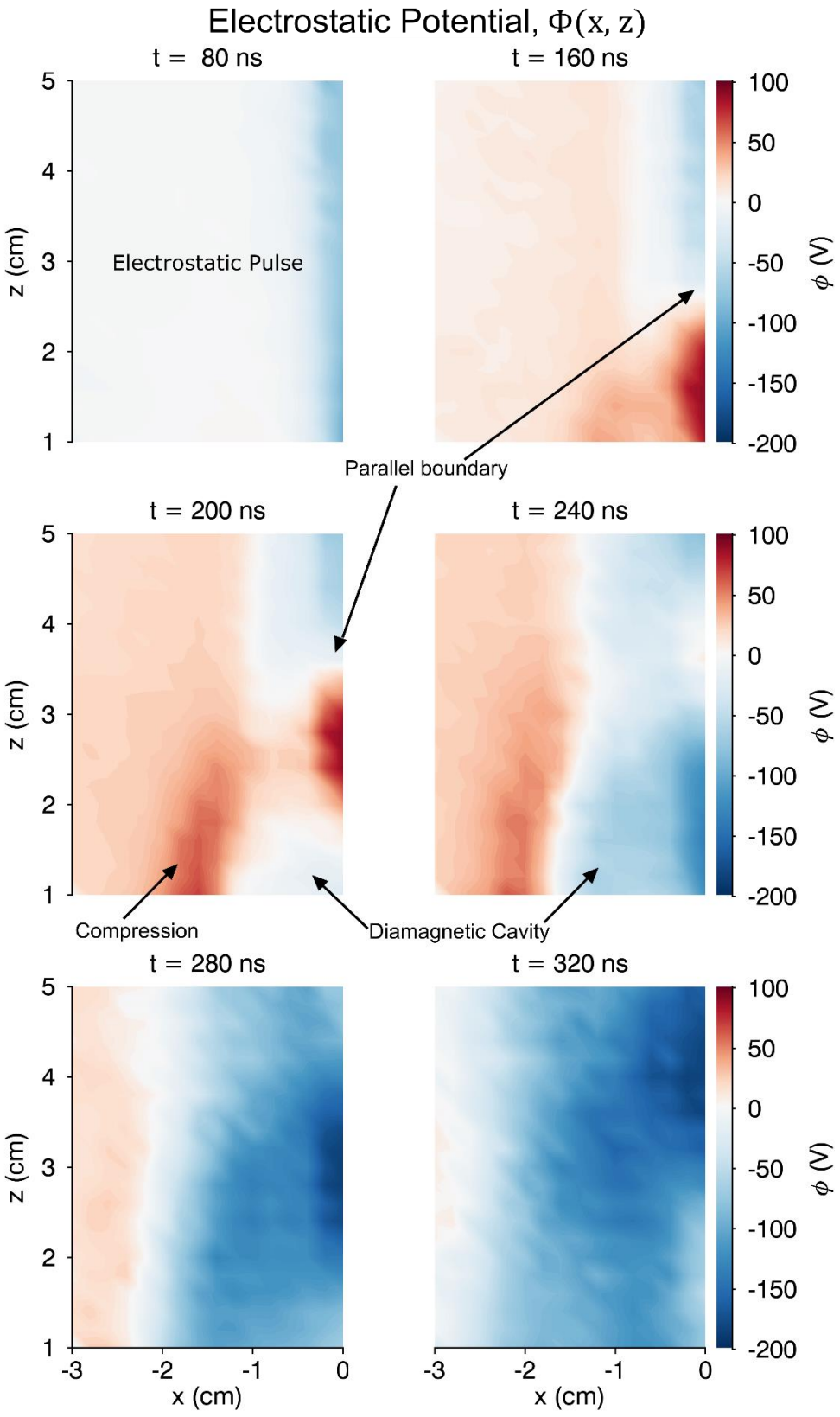

Figure 4.13:

Electrostatic potential measurements in the $x - z$ plane.

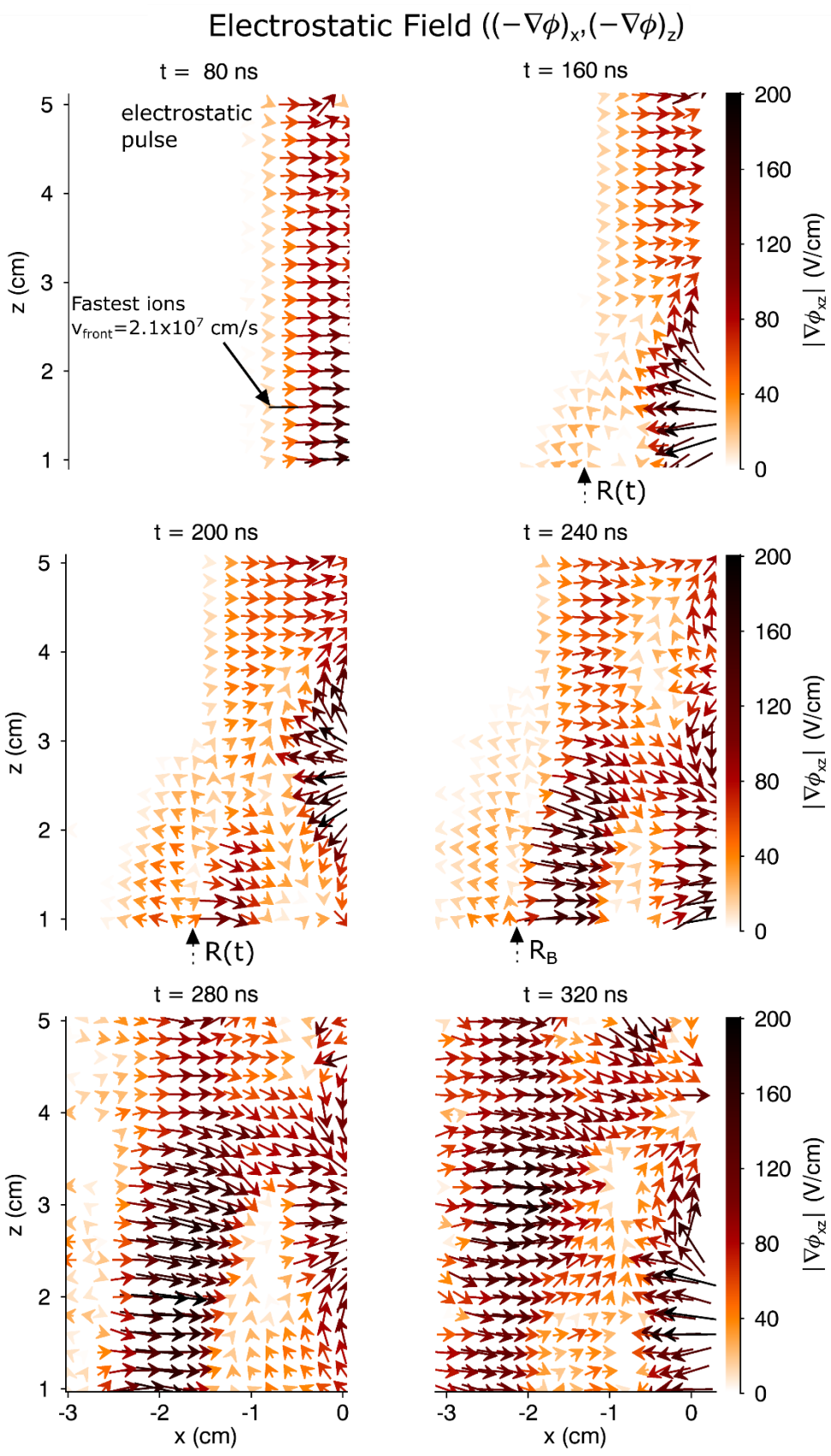

Figure 4.14:

Electrostatic field measurements in the $x-z$ plane at times corresponding to that of Fig. 4.5.

that appeared ahead of the LPP can be explained by electron currents similar to those within the bulk LPP and diamagnetic cavity but within this new electrostatic structure. What cannot yet be explained is the source of the electrostatic field and the boundary between it and the diamagnetic cavity in the bulk LPP represented by the structure of $t = 160$ ns in Fig. 4.11. To aid in understanding the origin of this electrostatic structure, one must understand the distribution of charge within the LPP. This requires knowing how the electrostatic field behaves along the background magnetic field.

The electrostatic potential and field measurements in the $x - z$ plane are shown in Figs. 4.13 and 4.14. At $t = 80$ ns, the extent of the initial electrostatic pulse is quite clear. The frame also shows how tightly bound the structure of the electrostatic pulse is to the magnetic field line. Within the time it crosses the $x - z$ plane, there is almost no angular spread along the field and no observable component of $\boldsymbol{E}$ parallel to $\boldsymbol{B}$. The frame for $t = 160$ ns shows the boundary between the electrostatic pulse and the bulk LPP and diamagnetic cavity. This "parallel boundary" has a far more complicated structure in the electric field. This has strong components along and across the ambient magnetic field which are highly confined to the axis of the LPP. These fields rapidly diminish in strength and become comparable to but still distinguishable from the cavity fields by $t = \tau_D$. Complicated fluctuations that do not resemble coherent behavior continue along the axis of the LPP but remain highly localized. As the probe moves closer to the axis towards positive x values, the disturbance due to the finite size of the probe cannot be neglected and behavior for $|x| \leq 0.5$ cm and $z < 3$ cm, essentially those deep within the bulk LPP, should be treated with some skepticism.

The laminar components of the electrostatic fields of the diamagnetic cavity near its edge seem relatively unaffected when they come into view for $t \geq 200$ ns. The boundary defined by

the reversal between the radially inward and outward fields is seen to grow in time and encapsulate the ovular LPP as would be expected from the discussion around Fig. 4.11. Despite the clear z dependence of the electrostatic structures near the parallel boundary of the LPP, the electric field parallel to $\boldsymbol{B}_0$ is very small. That is, away from the parallel boundary, $\boldsymbol{E}_{st} \cdot \boldsymbol{B}_0 \approx 0$. For $t > \tau_D$, the entirety of the LPP is dominated by the lingering, radially inward electrostatic field of the collapsing diamagnetic cavity.

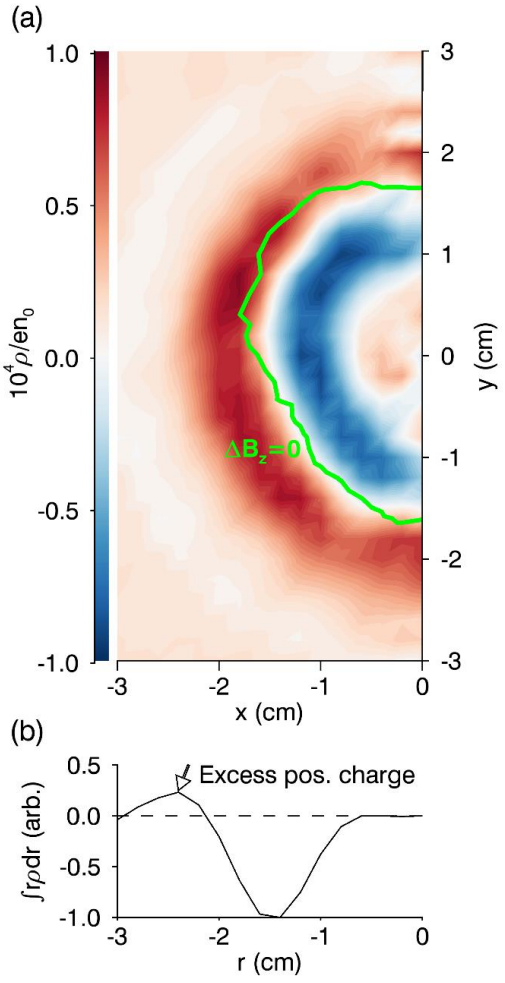

Figure 4.15: Charge distribution within the diamagnetic cavity for $t = \tau_D$ normalized to the ambient plasma density. A contour of $B_z = B_0$ within the diamagnetic cavity is also shown to emphasize the location of the charge layers.

With this data and the relatively good assumption of cylindrical symmetry, as evidenced by Fig. 4.11 for $t \leq \tau_D$, the charge distribution within the diamagnetic cavity can be calculated. The distribution is calculated at $t = \tau_D$ and $z = 2$ cm near the diamagnetic equator and shown in Fig. 4.15. The double-layer-like structure corresponding to the dominant inward electrostatic field is quite evident in the $x - y$ plane of Fig. 15a. By superimposing a contour where the magnetic field is equal to the ambient field, it is easy to see that the charge layering is such that positive charge is built up in the compression while the negative charge layer is well within the diamagnetic cavity. The magnitudes of each of the charge layers are comparable to each other and peak at about 1 part in 10,000 of the ambient plasma density. Such a normalization merely emphasizes that the strong electrostatic fields that have been measured are consistent with a quasi-neutral description of the fields. The comparable size of the charge layers and their cylindrical geometry actually suggests a charge *imbalance* between the layers since the positive layer is distributed over a larger volume than the inner, negative layer. Such an imbalance would explain the radially outward field and thus how a magnetized expansion can control its own magnetic field compression. This is in contrast to the common superconducting dipole expansion model [20], which requires a compression of about 50% in a region free of current. Such a compression is hardly ever observed in LPPs.

By integrating over an element $\int dr\, r$, the charge density per unit length along z is obtained and such a calculation is shown in Fig. 4.15b. This shows quite clearly the possibility of charge imbalance as the positive charge layer is in fact larger than the negative charge layer. This could have been anticipated by considering the radially outward electrostatic field of Fig. 4.11 and 4.14. If one were to take an envelope encapsulating the bulk LPP electric fields of Fig. 4.11 and

4.14, one would see that the radial boundary has a net electric flux. An application of Gauss's Law to this envelope would then suggest the LPP has a net positive charge. Global charge neutrality suggests that the balancing negative charge must be either at the parallel boundary of the LPP or be carried off with the electrostatic pulse. This provides a reasonable explanation for the observed electrostatic pulse and the complicated parallel boundary exhibited by the electrostatic field.

Fast electrons have been observed previously in LPP experiments on the LAPD which have also been associated with whistler wave and Alfvén wave radiation [68, 69]. These electrons moved at speeds many times that of the LPP with energies on the order of 100 V, which is coincidentally the scale temperature of the initial LPP and the depth of the electrostatic pulse. The electrostatic pulse also moves close to these speeds and so it seems reasonable to associate this structure with at least some of these fast electrons. These electrons are not neutralized locally by the LPP ions and are moving at speeds much faster than the ambient electron thermal speed. They could thus constitute the bulk of "lost" negative charge that balances the net positive charge of the LPP. More speculatively, the complicated electrostatic field at the parallel boundary of the diamagnetic cavity could then be explained as a non-linear electrostatic structure such as a double-layer, shock, sheath or what the space community has quite prosaically termed a time-domain structure [70]. The ability to distinguish between these structures is beyond the ability of the current diagnostic arsenal but the purely electrostatic nature is apparent in that no similar structure appears at the parallel boundary in the magnetic field data of Fig. 4.5. It is clear that whatever it is, it is evanescent and of a very small spatial and temporal scale limiting its ability to play a role in coupling energy and momentum between the LPP and the ambient plasma.

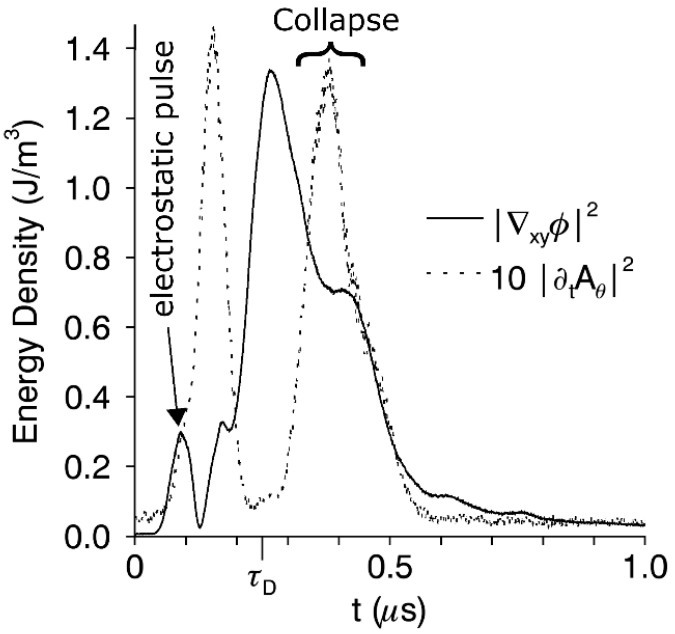

Figure 4.16: Energy density of the measured radial electrostatic field and azimuthal, induced electric fields over time.

4.4.5—Electrostatic Field Coupling

Now that the whole electromagnetic structure and its evolution has been described, one can discuss the momentum coupling. From simple comparison of peak magnitudes, the electrostatic field will have a stronger effect than the induced electric field on the coupling between the LPP and ambient plasma. A fair measure of their ability to couple energy and momentum volumetrically and independent of their profiles or a model is to consider their average energy density. Applying cylindrical symmetry to the measured induced and electrostatic fields, the average energy density of the $\boldsymbol{e}_\phi \cdot \boldsymbol{E}_{ind}$ and $\boldsymbol{e}_r \cdot \boldsymbol{E}_{st} = \nabla_{xy}\phi$ fields are shown in Fig. 4.16. Figure 4.16 shows quite clearly that the strength of the electrostatic interaction is dominated in space and time by the electrostatic field and not the induced electric field. It is necessary to emphasize that these data do not include the fields for $z < 1$ cm. The probes could not safely be positioned so

close without risking serious damage to the probe and interference with the measurements. This is precisely where the induced field should be its strongest and the electrostatic field negligible for $t < \tau_D/2$. This missing volume accounts for less than 10% of the interaction volume is likely of little consequence to the overall interaction.

The prevalence of the inward electrostatic field throughout Figs. 4.11 and 4.14 indicate that the effect of a collisionless interaction between the LPP and an ambient argon plasma is to pull the argon ions inward, against the flow of the expanding LPP. As is shown in Appendix §B.4, the idealized Rayleigh model limits the maximum obtainable velocity from these fields to a fraction of the initial expansion velocity. For a C^{2+}, $\beta \sim 10^6$ expansion moving at $V_{r0} = 1.28 \times 10^7$ cm/s through argon, an ion can only attain a radial speed of $\Delta V_r \approx 8 \times 10^5$ cm/s at most ($\Delta V_r/V_{r0} = 0.06$). The expansion profile used in the Rayleigh model for the field also shows that a large portion of the argon ions will be moving slower than this speed. The corresponding energy transferred to the argon ions is about $E_c \approx 0.5$ mJ ($E_c/E_{tot} \sim 0.002$).

The idealized model, however, does not take into account 3 facets of the measured electrostatic fields:

(1) The electrostatic pulse that appears before the diamagnetic cavity. This field will tend to accelerate more of the ions near $r \sim 0$ where the other fields would not. The strength of this field is comparable in strength to the inward electrostatic field of the diamagnetic cavity. Ions within it would reach comparable speeds and thus smooth out the ion velocity profile.

(2) The measured profile for E_{st}, which has the field peaking at around $r/R(t) \sim 0.6$ within the sheath structure and behind the cavity edge. This will decrease the maximum velocity and shift it further from $r = R(t)$ than that calculated in Appendix §B.4.

(3) The radially outward electrostatic field associated with the field compression. Argon ions that enter the LPP at $r = R(t)$ receive the kick ΔV_r after a slight outward push. This will also tend to decrease the final inward velocity of the argon ions.

Shot-to-shot variation of the fields will also tend to smooth out the velocity profiles. This along with (2) and (3) ensure no argon ions will actually reach 8×10^5 cm/s.

In the azimuthal direction, the 100 V/cm fields of E_{ind} exist in such a small volume that the diagnostics employed could not observe them. For the regions relevant for the LIF diagnostic, E_{ind} peaked at about 1/6 the strength of E_{st} and reverses sign. The LIF reveals these features and shows that E_{ind} couples very little momentum and energy in the argon background.

4.5—LIF Data

The LIF data were taken at various times during the LPP expansion with the same camera as used in §4.2. The LIF beam passed through the LPP along the x-direction, as in Fig. 3.10, at $z = 2$ cm with a width of 0.5 cm in z and 10 cm in y. The camera was mounted 2.1 m in z away from the target region. A mirror was positioned within the LAPD vacuum vessel offset in x by 20 cm and angled so as to project the light from the target region into the camera. At that distance, the angle between the projected image and the magnetic field was about 5° and a maximum spatial resolution of $\delta x_{max} = \delta y_{max} = 0.048$ cm.

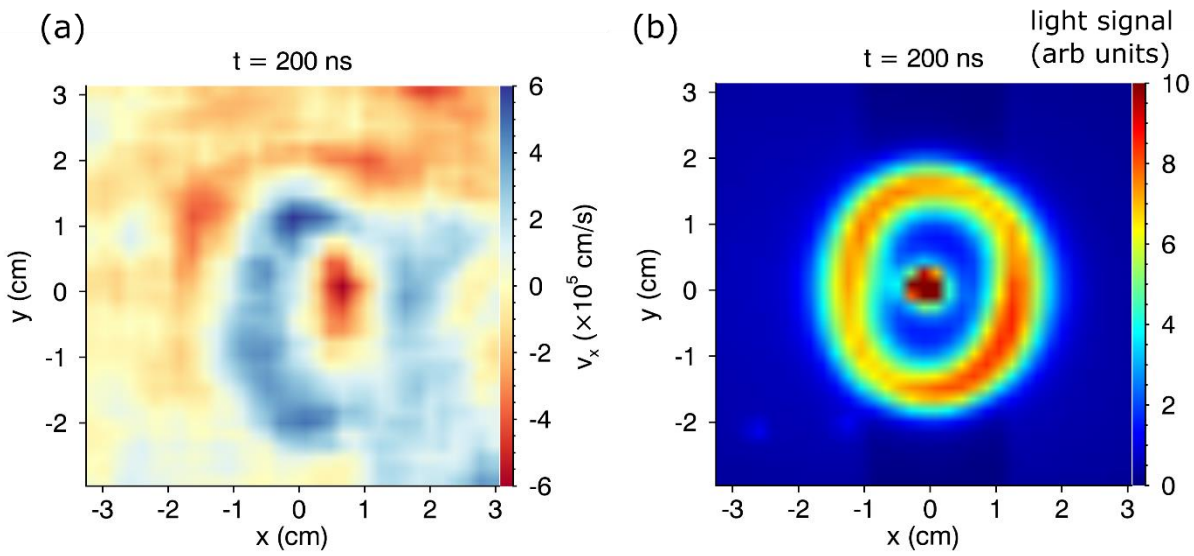

Figure 4.17: (a) LIF signal at $t = 200$ ns just before peak diamagnetism. (b) Corresponding background emission through the 1-nm filter.

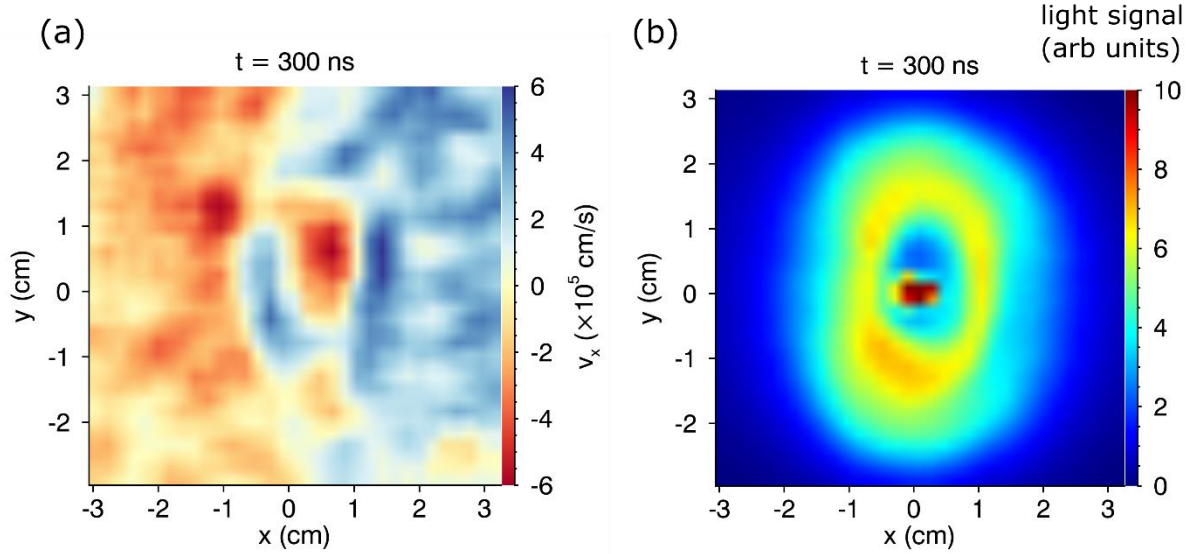

Figure 4.18: (a) LIF signal at $t = 300$ ns, soon after the onset of cavity decay. (b) Corresponding background emission through the 1-nm filter.

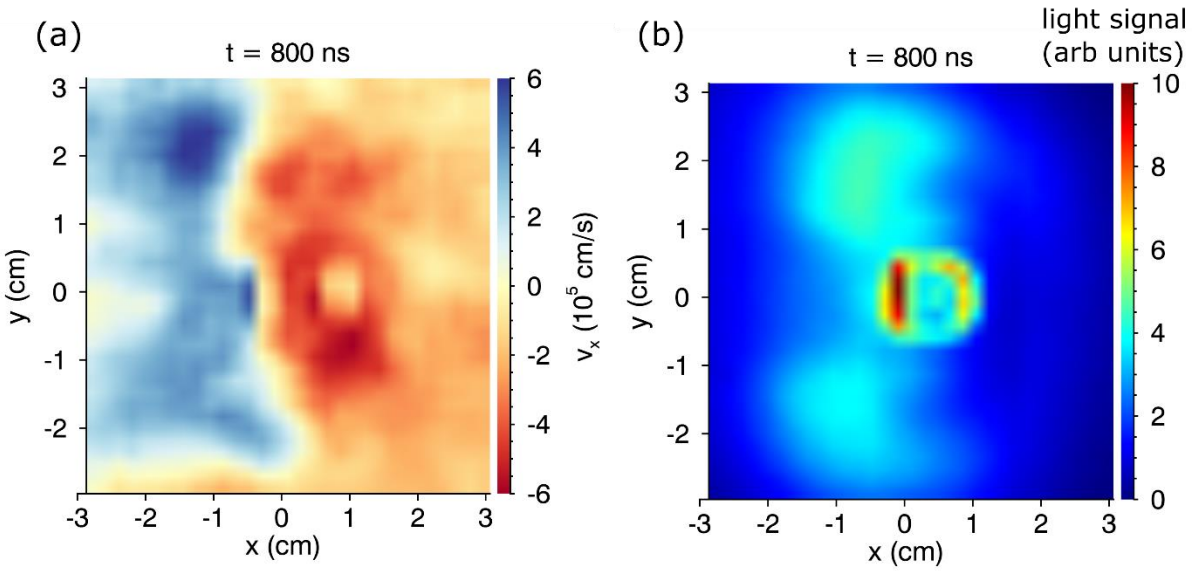

Figure 4.19: (a) LIF signal at $t = 800$ ns after both the magnetic field and electrostatic field structure have essentially disappeared. (b) Corresponding background emission through the 1-nm filter.

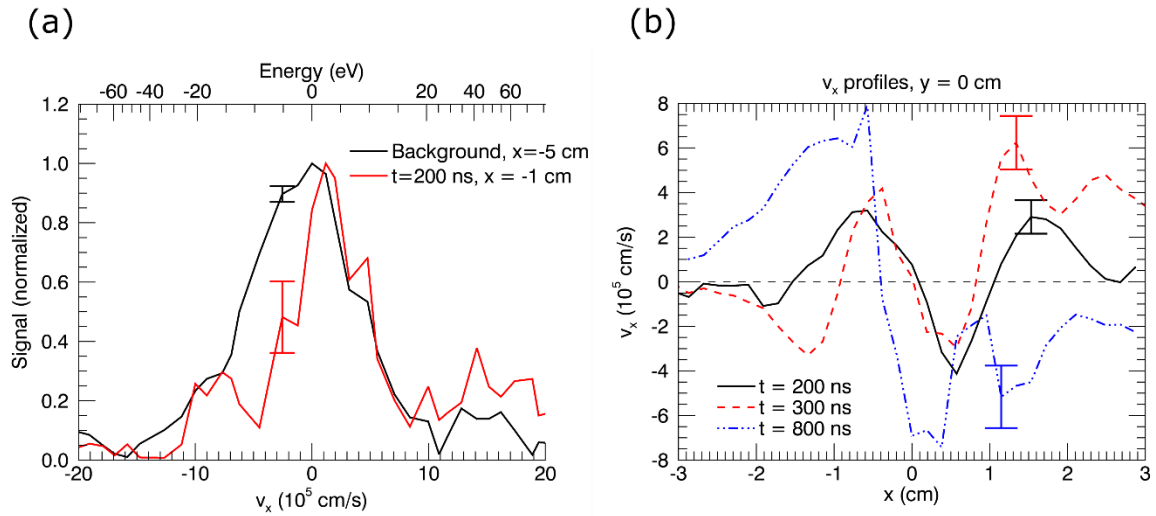

Figure 4.20: (a) LIF sample distributions taken from $t = 200$ ns, $y = 0$ cm in the background ($x = -5$ cm) and within the cavity ($x = -1$ cm). (b) Average v_x profiles at $y = 0$ cm from Figs. 4.17-4.19.

At each time, LIF scans comprised a set of images at each of a series of wavelengths about the central wavelength $\lambda_0 = 611.4922$ nm. Typical wavelength ranges were set such that they

would span the velocities $v \in [-2,2] \times 10^6$ cm/s in order to ensure the full distribution was covered. From each set of images, each pixel was analyzed and "cosmic" outliers with signals 5σ above the mean signal removed. Additionally, spurious images from camera or laser misfires were removed entirely. Three scans at $t = 200, 300,$ and 800 ns were complete and reliable enough to have Maxwellian distributions fit to the signals versus Doppler broadened velocity. The shift of the argon velocity distribution within LPP compared to one at $x = -5$ cm, far from LPP influence, gives an accurate measure of the average argon ion velocity in the x-direction, v_x. The resulting flow field of argon ions from this measure at the times mentioned are shown in parts (a) of Figs. 4.17-4.19. Sample velocity distributions showing a background ion distribution and an ion distribution within the diamagnetic cavity are shown in Fig. 4.20a while profiles of the flow field at $y = 0$ cm over time are shown in Fig. 4.20b.

Signal to noise ratios of spectroscopic techniques in systems that emit light as copiously as dense LPPs are generally poor. Additionally, changing surface conditions of the target shifts the motion of the LPP subtly from shot to shot which exacerbates the problem by introducing an element of non-reproducibility. For argon LIF in the LPP system, the raw signal to noise ratio through the 1-nm filter of Fig. 3.5 was $SNR_{raw} \sim 1.07$ for a single shot. This was improved by background subtraction and averaging over a multitude of images at each wavelength. Background subtraction was accomplished by staggering shots with and without an LIF laser pulse—about 250 of each. The set of signal and background images were averaged and subtracted. Finally, pixels were binned in 4x4 groups and their signals averaged. This gives a signal to noise ratio of about 5 for $t = 200, 300$ ns and ~ 10 for $t = 800$ ns. It is higher at 800 ns owing to the decreased background level seen in Fig. 4.19b. The final spatial resolution for the images in Figs. 4.17-4.20 is $\delta x = \delta y = 0.19$ cm or almost exactly that of electromagnetic field diagnostics.

At $t = 200$ ns, the electric fields in the probing volume of the LIF are near their strongest and their effect on the argon ions is nearing their peak. The maximum velocities in Figs. 4.17a and 4.20b at this time are near 3×10^5 cm/s with a clear asymmetry across the line $x = 0$ cutting through the LPP. This gives a clear indication of a radial symmetry in the causative force. A force in the azimuthal direction would have produced a symmetry across the axis $y = 0$ in the v_x. The velocities near $x = 0$ are oriented such that argon is being transported back to the axis of the LPP which is also in accord with the electrostatic field that was measured earlier. Also visible is the effect of the radially outward electrostatic field.

At the outer edge of the LPP expansion, indicated by the bright ring in Fig. 4.17b, there is a clear reversal in the sign of v_x which peaks at the smaller value of about 1×10^5 cm/s or about 1/3 of the inward velocity. This ratio is also approximately the ratio of the outward to inward electrostatic fields. The difference between the velocities, rather the net effect of the inward electrostatic field is the difference between the two or about $\Delta v_x = 4 \times 10^5$ cm/s or about 1/2 of the maximum value predicted from the ideal Rayleigh model.

At $t = 300$ ns in Fig. 4.18a, corresponding to the onset of cavity collapse, the effect of the electric fields has the same general shape as that of Fig. 4.17a. The weaker electrostatic fields that exist outside of the LPP and associated with the compression have had time to push the argon at the far reaches of the LPP. In comparing Fig. 4.18a to Fig. 4.17a it may be noted that it seems as if the LPP has shrunk in size over time and one would rather expect the effect of the inward electrostatic field would move further outward rather than collapse. To explain this behavior, note that it is clear in Fig. 4.18b that the LPP itself appears smaller than that of Fig. 4.17b. Time variation of the LPP as shown in Fig. 4.3 has no evidence of LPP collapse in this time range. The major difference between these three data sets is the target. This is because the LIF scans require

so much time that a scan at one particular time is all that can be done on a single carbon target. A simple explanation then is that between the LIF scans of Fig. 4.17 and Fig. 4.18, the target change altered the initial conditions, likely the laser energy coupling, and indeed the LPP for $t = 300$ ns was smaller than that of $t = 200$ ns. The $t = 200$ ns and $t = 300$ ns datasets are consistent with each other and qualitatively with the electric fields if the size of the LPPs are accounted for by referring to parts (b) in Figs. 4.17 and 4.18.

The LIF data for $t = 800$ ns in Figs. 4.19a and 4.20b shows the net effect of the LPP on the argon ions after the diamagnetic cavity has fully decayed. Slow expansion of the inward electrostatic field across the magnetic field (Fig. 4.11, $t \geq 280$ ns) is shown clearly here as the majority of the argon ions in view are drifting back toward the LPP axis with approximately $v_r = -6 \times 10^5$ cm/s, or twice the inward velocity that was observed earlier at $t = 200,\ 300$ ns, near peak diamagnetism. In this time, the induced electric field switches sign to correspond to the filling in of the cavity while the electrostatic field remains strong throughout the collapse. This shows quite clearly that the sum effect of the total electric field over the passage of the LPP and the expansion and collapse of the diamagnetic cavity is that the electrostatic field pulls the argon ions inward and the effect of the induced field is entirely negligible.

It was mentioned in the discussion of the Rayleigh model in §2.3 and Appendix §B.4 that the predicted velocity of 8×10^5 cm/s was more of an upper on the velocity and most argon ion velocities would be smaller. To check if the measured velocities from LIF are indeed consistent with the measured electric fields, a particle orbit solver was implemented to trace the motion of ions through the total electromagnetic fields.

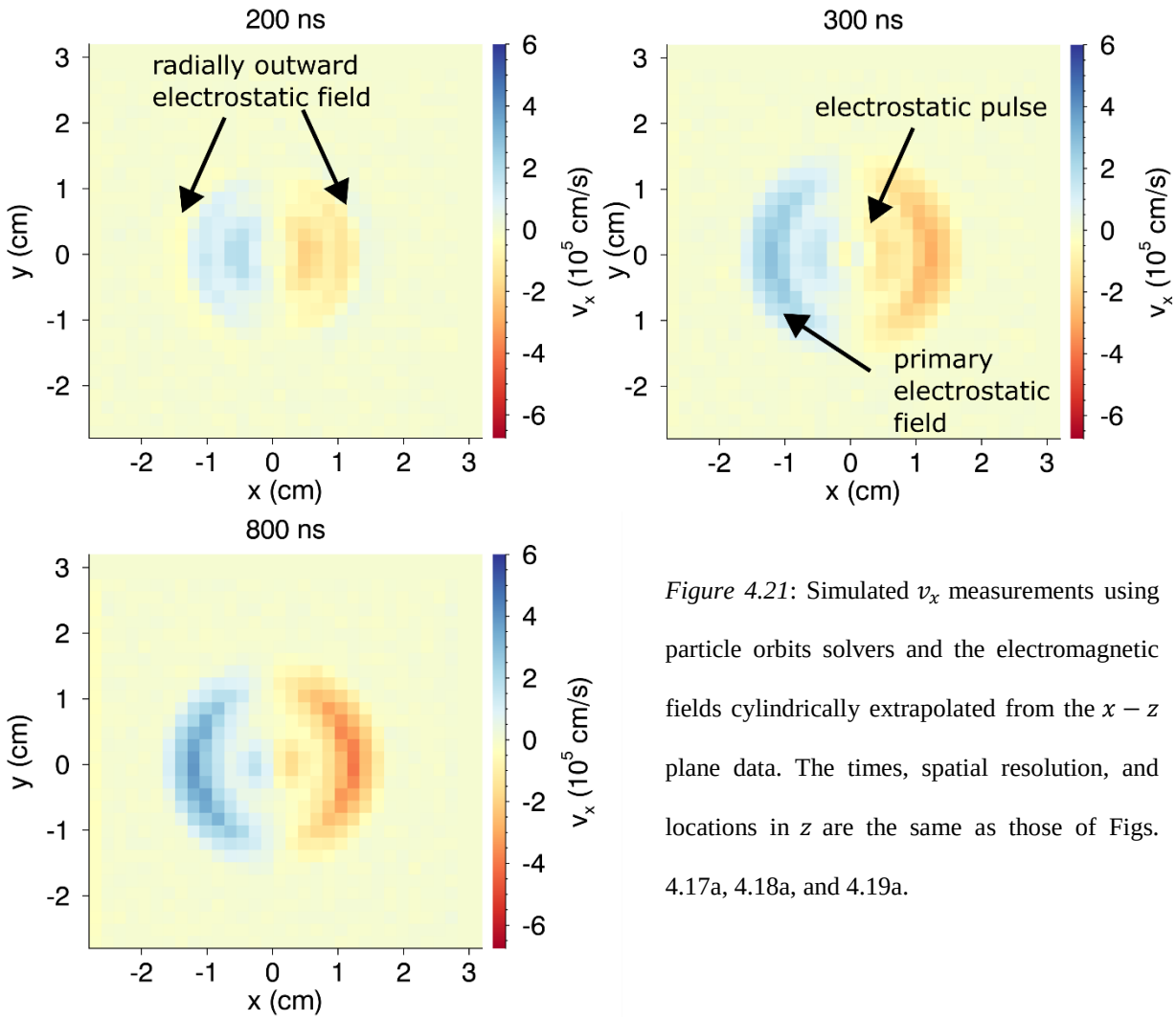

Figure 4.21: Simulated v_x measurements using particle orbits solvers and the electromagnetic fields cylindrically extrapolated from the $x-z$ plane data. The times, spatial resolution, and locations in z are the same as those of Figs. 4.17a, 4.18a, and 4.19a.

4.6—Orbit Solvers

Though fully volumetric measurements of the electromagnetic fields were not made, the LPP exhibited, on the average, good cylindrical symmetry. The fields as measured in the $x-z$ planes, corresponding to Figs. 4.5,4.9, and 4.14, were used by filling a 3D volume with their values rotated about the azimuthal direction. Ten million particle trajectories were evolved with random initial position and velocities (1 eV initial temperature) within these fields. At the three points in time for which LIF data was collected, the distribution functions were mapped onto spatial grids with the same 2 mm resolution of the field data. The average velocity in the x-direction was

calculated thus simulating the effect of an LIF scan. The results are shown for the three times in Fig. 4.21.

The orbit solvers show quite clearly through the symmetry across $x = 0$ that the electrostatic field dominates the coupling of momentum to the ambient argon. Also visible in the orbit solvers is that the effect of the electrostatic pulse is visible as the increased velocity near the axis of the LPP. The Rayleigh model as well as the measured fields within the cavity suggested that a gradient should exist in v_x such that particles closest to $x = 0$ should not be moving. The presence of the field from the electrostatic pulse accelerates those ions to a comparable velocity and effectively smooths out the velocity gradient. The scale size of the velocity, $|v_x| = 3 \times 10^5$ cm/s, is identical to that of the LIF. The ability to reproduce the magnitude of the momentum coupled with an orbit solver in the measured electromagnetic fields brings together two important facts which I intended to show:

(1) The orbit solver did not include collisions so that the signal measured by the LIF is indeed indicative of an interaction dominated by a collisionless mechanism.

(2) The measured electric fields, which are well-predicted by a laminar model of the LPP evolution, are sufficient to explain the measured momentum coupling. All other sources of coupling via turbulent wave-particle interaction or high-frequency waves or oscillations beyond the resolution of the diagnostics are at most perturbations that on average do not produce a coherent flow in the ions of the ambient plasma.

Chapter 5 – Parameter Variation

5.1—Variable parameters

In the previous chapter, it was shown that the total electric field in a high β expansion includes a substantial electrostatic component. The features of this electrostatic field dominate the collisionless coupling of momentum and energy from the expanding plasma to the ambient plasma for the present case of weak coupling. The goal of this chapter is to examine how those results vary under parameter changes. Based on the Rayleigh model and general plasma expansion characteristics, there are 5 crucial, independent parameters:

(1) $\beta = (R_B/R_0)^3$

(2) $\omega_{ci}^d \tau_D$

(3) $(R_m/R_0)^3$

(4) $\left(R_q/R_0\right)^3$

(5) $\boldsymbol{V}_n \times \boldsymbol{B}_0/|\boldsymbol{V}_n \times \boldsymbol{B}_0|$: angle between the target normal and the ambient magnetic field.

There are of course many other parameters that can be varied such as target geometries and ambient plasma equilibria, but these would be features of optimization experiments rather than general to a magnetized expansion.

Practical considerations of the LAPD device and LPP generation limit the ways in which the parameters above can be changed. For instance, the very weak scaling of parameters of the LPP with laser energy and power mean the LPP characteristics can only really be changed by changing the target composition. Materials other than carbon are either difficult to apply to the target geometry used here or has the potential to react chemically with the BaO source within the

LAPD. This means that parameters (1) and (2) can only be changed through the magnetic field and not independently of each other. Similarly, (3) and (4) cannot generally change independent of each other but rather both must change by changing the ambient plasma. Ideally, changes in each of these parameters would be accompanied by full electromagnetic field measurements to show how they change the structures in the induced and electrostatic fields. This is especially true of parameter (5) for which $\boldsymbol{V}_n \times \boldsymbol{B}_0 \neq 0$ destroys the cylindrical symmetry and limits the calculation of $\boldsymbol{E}_{ind}$ to the axis of the flow, i.e. along $\boldsymbol{V}_n$, unless global measurements of the current are obtained. Measurements presented herein are for the parameters that could be changed and attempts are made, speculative as they may be, to put them into the context of the model of §2.3 and the extension towards the strong coupling limit.

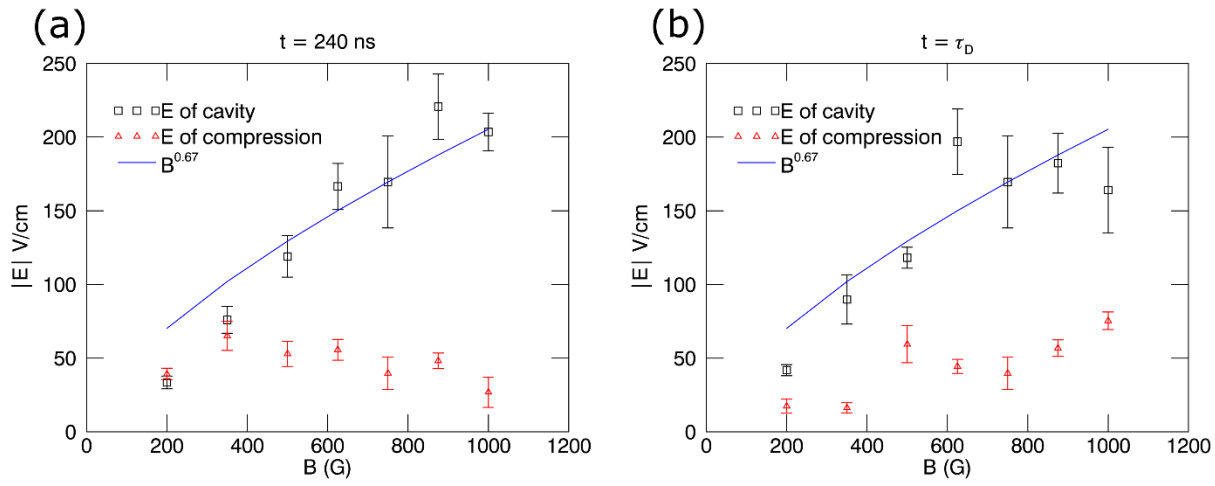

Figure 5.1: Variation of the inward (black) and outward (red) electrostatic field strength with ambient magnetic field for (a) $t = 240$ ns and (b) their respective peak diamagnetism times, $t = \tau_D \sim B^{-2/3}$. Solid line shows $B^{2/3}$ scaling of the fields normalized to the case of 750 G.

5.2—Variation of $\boldsymbol{B}$

The induced electric field, being predominantly in the azimuthal direction is affected by two terms in Ohm's law: $\boldsymbol{V} \times \boldsymbol{B}$ and $\eta \boldsymbol{J}$. The latter is weak during the expansion phase and the

former can only be linear in the magnetic field. The more interesting variation with $\boldsymbol{B}_0$ is in the electrostatic field. Plasma potential measurements were made along the line $y = 0$ in the same geometry and ambient plasma as Fig. 4.11 for magnetic field strengths from 200 G to 1000 G. The electrostatic fields in the radial direction were calculated from these data and characteristics of the inward field of the diamagnetic cavity, the outward field from charge imbalance, and the electrostatic pulse were taken for each of the magnetic fields.

Figure 5.1 shows the variation of the outward and inward electrostatic fields for different magnetic fields. The connection between the electrostatic field and the Hall effect means that this field is affected by the magnitude of the magnetic field, its gradient, and the local electron density. The latter two depend on time for the same LPP conditions. Viewing the variation of these field strengths at the same time, as in Fig. 5.1a, shows the magnetic rather than the density variation. The particular time $t = 240$ ns is chosen as τ_D for the 750 G case and is such that the equator of the diamagnetic cavity is near the diagnostic for all the magnetic field cases. Figure 5.1b shows the field strengths at the scaled peak diamagnetism time, $\tau_D \sim B_0^{-2/3}$. Looking at such a scaled laboratory time is like looking at the LPP in the same stage of its evolution. For $B_0 < 750$, this accounts for the depletion of electrons due to further expansion that affects the Hall term. Conversely for high magnetic fields, it accounts for more compressed electron densities.

For the inward electrostatic field, both times exhibit a strong dependence on the background magnetic field. The scaling for the maximum field in the Rayleigh model is given by $R = R_B$ in Eq. 2.4 so that $E_{st} \sim B^{2/3}$ and this line is shown in Fig. 5.1a&b to show that this estimate is quite close. However, if the error estimates are accounted for and a power law scaling is applied, $E_{st} \sim B^n$, one finds that $n = 1.05 \pm 0.1$. As for the time dependence, note that the difference between τ_D and 240 ns for $600 < B < 1000$ G is less than 40 ns so that the times $t =$

240 ns and $t = \tau_D$ are separated by less than $\tau_D/5$. The Rayleigh model, specifically Figs. 2.4 & 2.5, suggest the electrostatic field does not change significantly during this period of time. The cases of 200, 375, and 500 G all increase slightly but no more than 10% from $t = 240$ ns to $t = \tau_D$. This means that the electrostatic field almost reaches its peak strength for times $t > \tau_D/2$ and does not seem to be strongly affected by the further depletion of plasma density.

The outward electrostatic field exhibits a weaker dependence on the magnetic field than does the inward electrostatic field. At $t = 240$ ns, the outward electrostatic field is about 50 V/cm and does not seem to exhibit any dependence on magnetic field at all. and at $B = 200$ G, it is in the same strength as the inward electrostatic field. This means that for the low magnetic field cases, it is no longer necessarily true that the LPP couples energy into the ambient plasma by pulling in the ambient ions. For the cases where the inward and the outward fields are approximately the same, the field structure can leave the ambient ions relatively unaffected. The interesting point here being that for $B < 200$ G, the outward coupling may become the strongest since $\boldsymbol{V} \times \boldsymbol{B} < 25$ V/cm. Further, this coupling might be independent of B. Looking at $t = \tau_D$ the outward field in the $B = 200, 350$ G cases drops in strength. The lack of change for the other measurements suggests that the observed drop for the low field cases is more a reflection of the fact that the diamagnetic equator has moved farther from the probe at the later times. Far from the equator in Fig. 4.14, the radial field drops off as well as the compression it is associated with in Fig. 4.5. The interpretation that the outward electrostatic field is caused by a global charge imbalance within the LPP is consistent with a weak dependence on the magnetic field. It also suggests that the outward field strength has more to do with the dynamics of the parallel boundary and how electrons escape along the magnetic field.

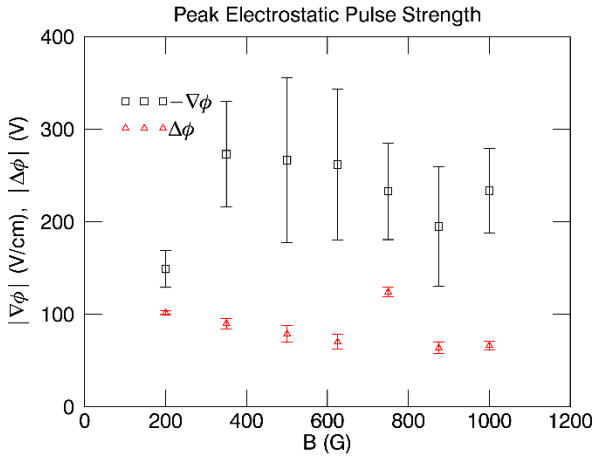

Figure 5.2: Electrostatic pulse strength versus magnetic field. Red triangles are potential well depths and black squares are peak electrostatic field strengths in the well.

Not many features of the electrostatic pulse change with the magnetic field. For all magnetic field cases, the pulse is observed to arrive at $z = 2$ cm between $t = 50$ and 60 ns as a potential well. It appeared to traverse the plane in the dataset of Fig. 4.14 in this time corresponding to a speed of about 4×10^8 cm/s or about 100 eV for an electron. After it appears, the well slowly deepens until the bulk ions of the LPP make it to the probe which happens around $t = 160$ ns. The peak electrostatic field from this potential well occurs between 130 and 140 ns after the laser pulse. The peak electrostatic field and the depth of the potential well at these times are shown in Fig. 5.2. Note the maximum potential drop is on the same order as the energy corresponding to an electron moving at the speed of the pulse. All the fields for $B > 200$ G are within error bars of each other and are essentially independent of B. The 200 G case has a lower peak field strength but not a significantly different voltage. This corresponds to a stronger widening of this well with time compared to the other cases though it is unclear why this occurred. The measured electric field strength is comparatively large for these low-field cases that its effect cannot be ignored. The

effect of this field is essentially to prime the ambient ions by delivering an inward impulse before the diamagnetic cavity reaches them. This effect will be spatially limited, though, as the full-width half-max of the pulses, $\Delta x_{FWHM} \sim 1$ cm, are generally much smaller than the diamagnetic cavity.

5.3—Perpendicular Expansion

When the preferred expansion direction, represented by $\boldsymbol{V}_n$ or the direction of the surface normal, is turned across the magnetic field, the mechanisms at play forming the diamagnetic cavity do not necessarily change. The similarity of the processes between the parallel and perpendicular allows the identification of similar structures but it should not be mistaken that they are the same. Rules of physical similarity are strict about changes in geometry being essentially different [26] and can lead to qualitatively different behavior. The angle between $\boldsymbol{V}_n$ and $\boldsymbol{B}_0$ introduces asymmetries into the induced and electrostatic fields. In the electrostatic field, this amounts to an additional polarization of the cavity and LPP in the direction perpendicular to both $\boldsymbol{V}_n$ and $\boldsymbol{B}_0$. This will be identified as the translational polarization, or $\boldsymbol{E}_{pol}$, to contrast it with the parallel polarization that results in the outward electrostatic field and parallel boundary structure and that of the radial polarization that forms the diamagnetic cavity. The three dimensional and transient nature of the diamagnetic cavity prevents this additional polarization and its electric field structure from being a simple matter of superposition of a uniform field. The translational polarization itself depends on the spatial profile of the magnetic field and flow field. With the diamagnetic cavity present, this gives $\boldsymbol{E}_{st}$ a far more complicated and harder to interpret appearance were it not for the consideration of the case $\boldsymbol{V}_n \times \boldsymbol{B}_0 = 0$ in Chapter 4.

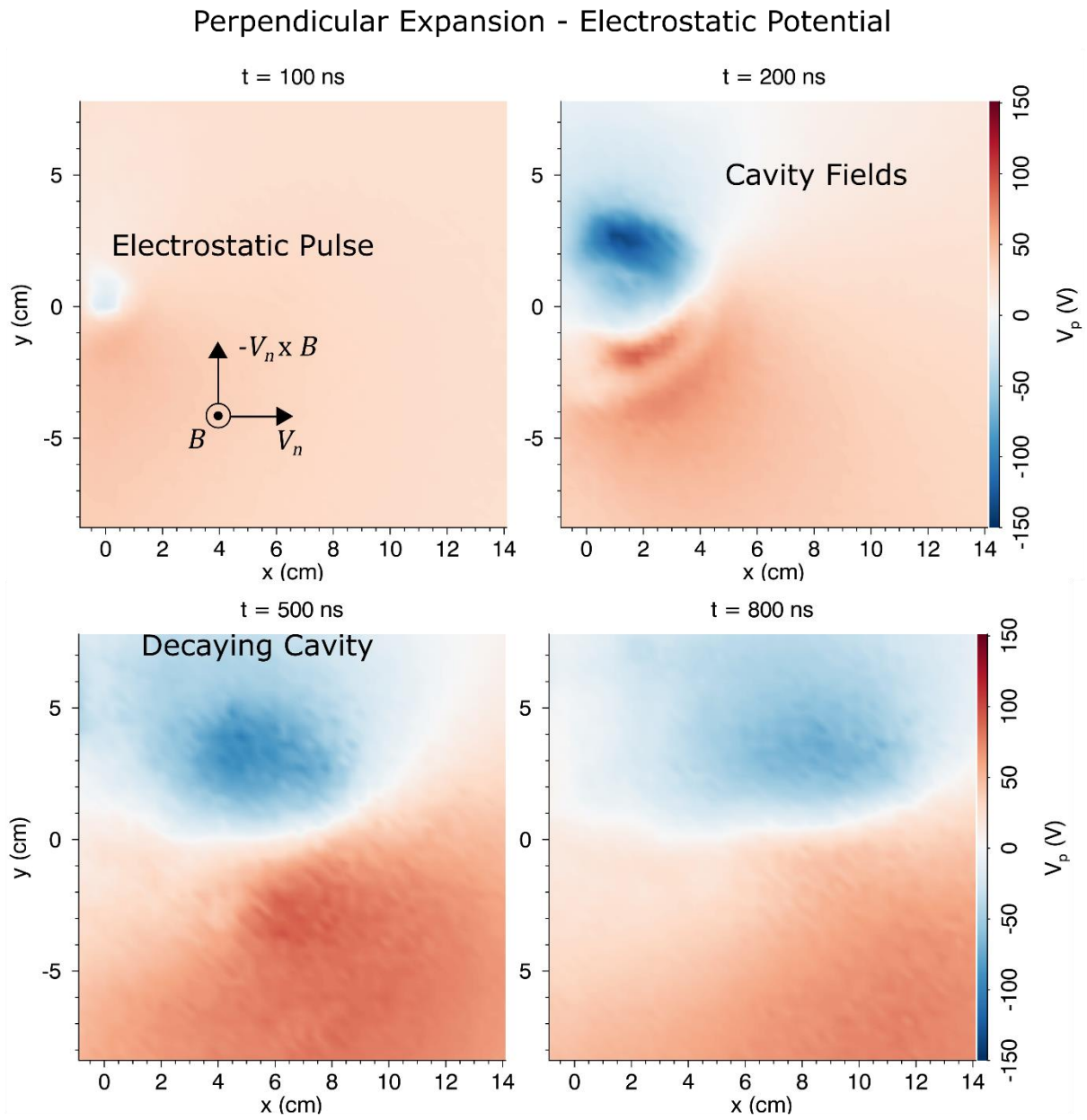

Figure 5.3: Electrostatic potential of the LPP and diamagnetic cavity for the case of an expansion directed across the magnetic field, $\boldsymbol{V}_n \cdot \boldsymbol{B} = 0$. See Fig. 3.3b for location of diagnostic plane.

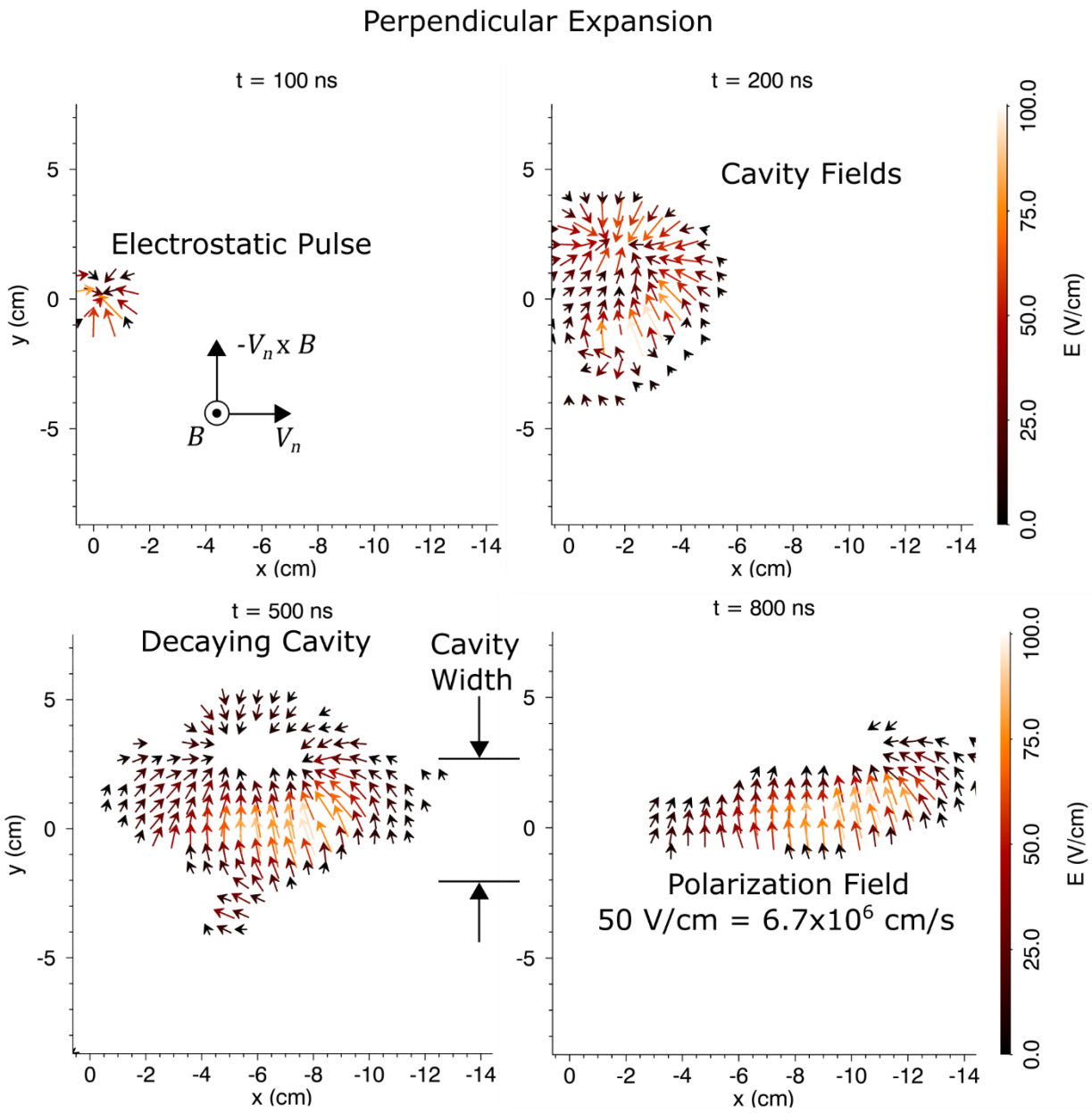

Figure 5.4: Electrostatic field evolution for perpendicular expansion of an LPP across a uniform magnetic field, $\boldsymbol{B} = -750\,\hat{z}$. The $x-y$ plane is offset in z by 3 cm from the plane containing the focal point and magnetic equator. Times chosen to clearly exhibit the structures and their contrast to the parallel case in Fig. 4.11. To emphasize the structures, fields of magnitude less than 15 V/cm have been suppressed.

The evolution of the electrostatic potential and field for the case $\boldsymbol{V}_n \cdot \boldsymbol{B}_0 = 0$ are shown in Figs. 5.3 and 5.4 for $B_0 = 750$ G. The $x - y$ plane shown is taken in a manner identical to that of Fig. 4.11 but with the laser-target geometry of Fig. 3.3b. The plane is therefore offset in z by 3 cm from one that contains the magnetic equator of the diamagnetic cavity and focal point of the laser on the target. This does mean that the cavity takes longer to reach the diagnostic plane and that the radially inward electrostatic field never reaches the full strength as seen in Fig. 4.11 but the present laser beam geometry prevents the probe from fully accessing this region. Consistent with the work of Van Zeeland [29] in a very similar setup, the laser-solid coupling in the perpendicular blow-off geometry yields a cavity that reaches peak diamagnetism later in time and with a larger size, $\tau_D > 400$ ns and $R_B \sim 3$ cm, allowing the cavity structure to reach $z > 3$ cm before the cavity begins to collapse.

The times chosen for display in Fig. 5.4 are to show the differences in the structures that were noted in Fig. 4.11. At $t = 100$ ns, the electrostatic pulse, which still shows up as early as $t = 50$ ns, is still centered near the focal point, but the strength of the field from the pulse (~ 60 V/cm) does not get nearly as strong as it did in the $\boldsymbol{V}_n \times \boldsymbol{B}_0 = 0$ case. It exhibits a small polarization of 20 V/cm ($v_x \sim 2.4 \times 10^6$ cm/s) suggesting that it is at least partially influenced by the cross field motion of the LPP. It does not move more than 0.5 cm away from the target before the parallel boundary of the cavity disrupts it. Thus it appears as though the source of this pulse is not attached to the LPP or diamagnetic cavity and is launched exclusively in the early stages of the expansion. The speed with which it appears to travel along the field in the parallel case, $v_{pulse} \sim 4 \times 10^8$ cm/s, suggests that whatever generates it occurs within 0.5 cm of the target or before $t = 40$ ns. This would explain its characteristic size from the focal point for both the $\boldsymbol{V}_n \cdot \boldsymbol{B}_0 = 0$ and $\boldsymbol{V}_n \cdot \boldsymbol{B}_0 = 0$ case. At $t = 200$ ns, the diamagnetic cavity comes into view. Again, the

fields of the cavity are weaker and no outward fields are present because the diagnostic plane did not pass through the magnetic equator of the cavity. It is clear that the cavity electrostatic field has obtained a strong up-down asymmetry. This asymmetry worsens as the cavity begins to collapse at $t = 500$ ns. Note that here, the apparent whole in the field at $(x, y) = (-6\text{ cm}, 3\text{ cm})$ is actually the top of the LPP and diamagnetic cavity. The center of the expansion lies near $y = 0$, but it does drift very slowly in the $+\hat{y}$ direction at a rate slower than 10^6 cm/s. The patch of strong electrostatic field near $y = 0$ is actually the translational polarization field becoming more uniform as the magnetic field fills in. At $t = 800$ ns, the magnetic cavity structure is mostly gone and the polarization takes on the simpler form corresponding to a uniform magnetic field.

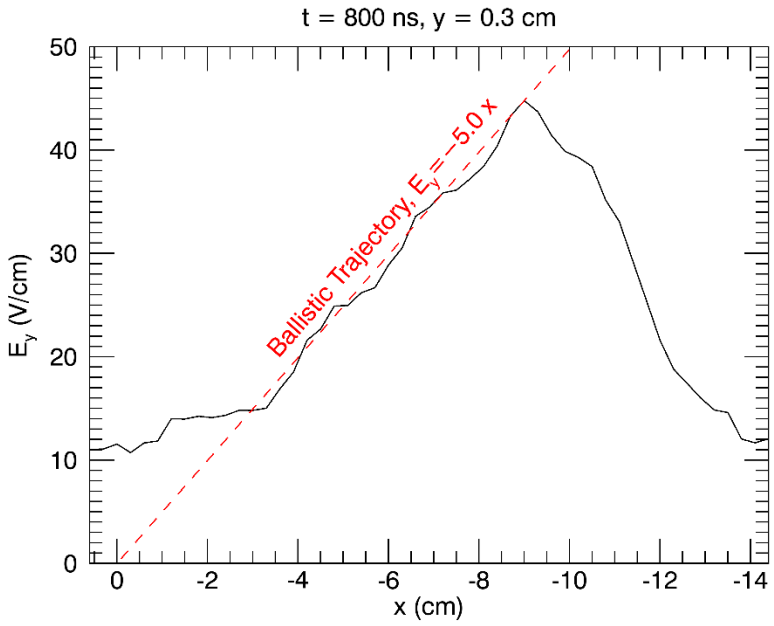

Figure 5.5: Trace (solid black) of the electrostatic field through $(y, z) = (0.3, 3)$ cm at $t = 800$ ns. A ballistic trajectory from a point source at $x = 0$ cm with peak speed $v_x = 6 \times 10^6$ cm/s across $B_0 = 750$ G produces the dashed, red line.

A profile of the polarization field, E_y, at $t = 800$ ns is shown in Fig. 5.5. The center of the expansion drifts upward slightly over time so that $y = 0.3$ cm is approximately the axis of the flow at the leading edge. If the whole mass of the LPP were moving uniformly across a uniform magnetic field, E_y would be independent of x in Fig. 5.5. If, however, the mass flow follow a ballistic trajectory from a point source, i.e. $V_n = V_{n0}x/X(t)$ in a similar manner to the Rayleigh model where $V_r = V_{r0}r/R(t)$, the profile of E_y would be linear. This behavior is captured extremely well in the region $x \in [-3.5, -9]$ cm and fits with a peak speed of 6×10^6 cm/s.

The speed calculated from the profile should not be interpreted as the speed of any particles within the LPP. From an Ohm's law perspective, the term responsible for the polarization was already included in Eq. 4.1. Ohm's law for the LPP as it was found in Chapter 4 is

$$\boldsymbol{E} = \frac{\boldsymbol{J} \times \boldsymbol{B}}{en_e} - \boldsymbol{V} \times \boldsymbol{B}.$$

For $\boldsymbol{V}_n \times \boldsymbol{B}_0 = 0$, the Lorentz term, $\boldsymbol{V} \times \boldsymbol{B}$, was mostly in the azimuthal direction and hence contributed mostly to the induced electric field. For $\boldsymbol{V}_n \cdot \boldsymbol{B}_0 = 0$, the Lorentz term has an asymmetry in the x and y directions. Noting that LPPs generally have $V_{n0} > V_{r0}$, the contributions to the induced field and electrostatic field at the front of the expansion can be approximated by

$$\boldsymbol{V} \times \boldsymbol{B} \approx \boldsymbol{V}_{exp} \times \boldsymbol{B}_0 + \boldsymbol{V}_m \times \boldsymbol{B}_0$$

where $\boldsymbol{V}_{exp} = V_r\hat{r}$ is the expansion velocity vector in the center of mass frame (see Fig. 2.1b) and $\boldsymbol{V}_m$ is the center of mass velocity. Since the cross-product of two irrotational vectors is solenoidal, $\nabla \cdot (\boldsymbol{V}_{exp} \times \boldsymbol{B}_0) = 0$, it represents an induced electric field. Since $\boldsymbol{V}$ in Ohm's law is the mass-weighted velocity, so long as ions are moving in a direction perpendicular to both the target normal and the ambient magnetic field, the polarization field is weaker than simply the ion motion in the

normal direction. When the diamagnetic cavity has dissipated, only the electrostatic term remains. By the time this happens, though, one must now account for deceleration of particles from the forces in the diamagnetic cavity and the mass loading of ambient ions. If LPP particles of mass density, ρ_m^d are moving at $\boldsymbol{V}_d$ through a stationary plasma of mass density, ρ_m^a, the polarization field is $\boldsymbol{E}_{pol} = \rho_m^d \boldsymbol{V}_d \times \boldsymbol{B}/(\rho_m^d + \rho_m^a)$.This means that the only time the polarization field after the diamagnetic cavity has collapsed is indicative of the local velocity of the particles is if ambient ions and the LPP are moving at the same speed. Otherwise, slower ambient plasma or even the overlapping presence of decelerated and ballistic LPP ions will reduce the polarization field. As long as the polarization field is present, some amount of the flow can almost freely move across the field or accelerate ambient ions. The dynamics of the perpendicular case after the cavity is rich but reduced to the problem of plasmoid propagation across the field. Some of the earliest work was done by Bostick [71], a good review of relevant physics of how these plasmoids decay is given by Borovsky [72], and the process by which polarized plasma flows sweep up ambient ions is known as "mass loading" in the space physics community.

As a final note, the nature of the translational polarization field should not be mistaken. It is an electrostatic field. Specifically, it has no directly associated $\partial_t \boldsymbol{B}$. It will exist for the case of a plasma moving across a magnetic field whether there is a diamagnetic cavity or compressional field or not as is clear from Fig. 5.4. It is also the measured in experiments such as Brenning [74] for the case of plasmas penetrating a magnetic barrier. It has been misinterpreted in studies such as Shaikhislamov [74] where they claimed to observe Larmor coupling and mass motion of the ambient plasma for a super-Alfvénic LPP expansion. The Larmor coupling mechanism is that described by [59] which is due to the induced electric field, $\boldsymbol{E}_{ind}$, of the cavity and magnetic compression. In [74], they observed an increased mass flow, which they interpreted as ambient

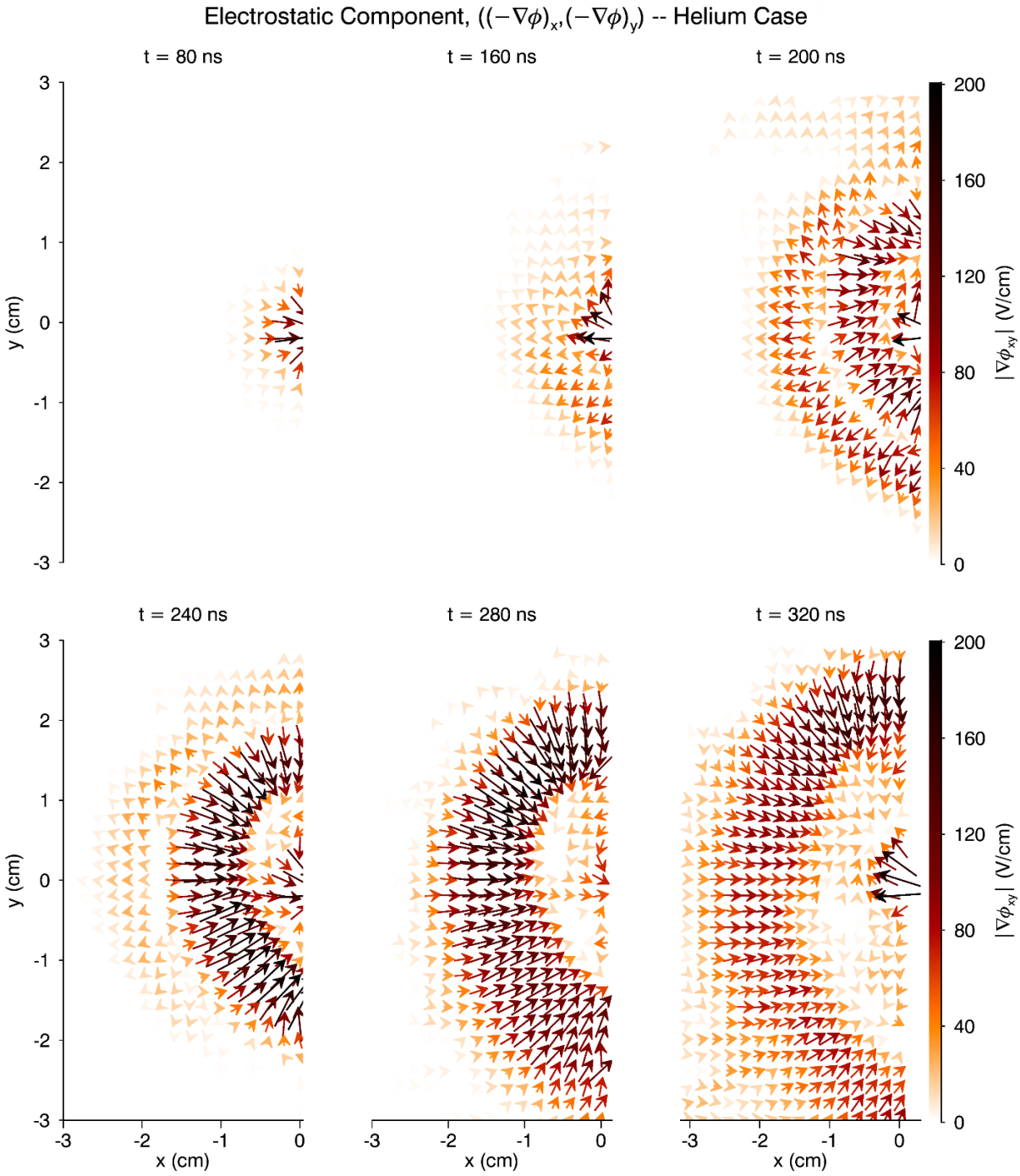

Figure 5.6: Electrostatic field data in an x–y plane located at $z = 2$ cm. The background gas is helium but otherwise conditions are identical to Fig. 4.11.

ions being swept up and an electric field consistent with the estimated $\boldsymbol{V} \times \boldsymbol{B}$. The field they measured, however, was with an electrostatic probe across the direction normal to the LPP source target. That is, they measured $\boldsymbol{E}_{pol}$, not $\boldsymbol{E}_{ind}$! Their coupling may not have had much to do with Larmor coupling or the magnetic field at all.

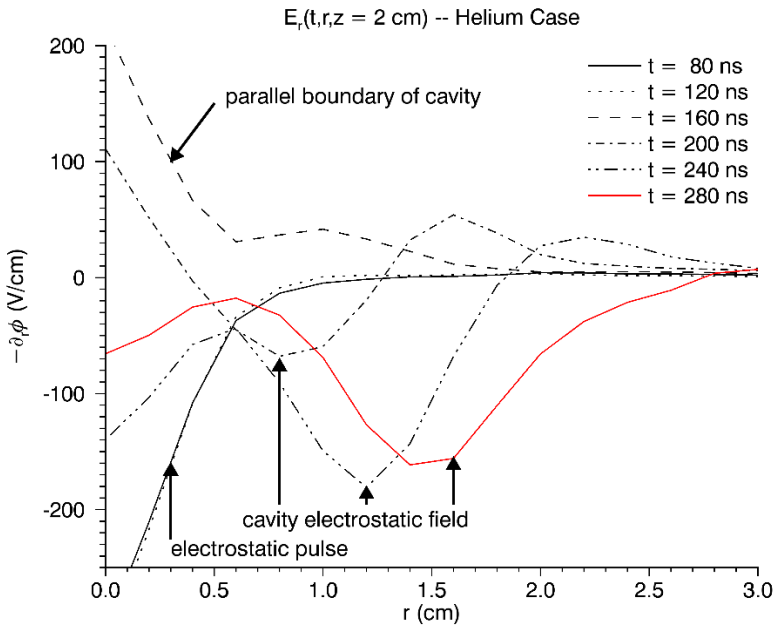

Figure 5.7: Radial variation of the electrostatic field as taken from Fig. 10 along y=0 cm. Compare to Fig. 4.12 for Argon under otherwise identical conditions.

5.4—Different gases

The final change in parameters available is the change in the ambient gas composition. This changes the parameters $(R_m/R_0)^3$ and, much more weakly due to ionization differences, $\left(R_q/R_0\right)^3$, which, as briefly explained in §2.3, are related to how the ambient plasma affects the field structure and thus is relevant to the case of strong coupling. It can certainly be said, at least

from the point of view of MHD, that the case studied in chapter 4 where $M_A \approx 1$, which corresponds to $R_m \approx R_B$, should be a case where the ambient plasma affects the electromagnetic fields. A change from argon to helium under otherwise identical conditions drops the M_A by a factor 3.2 and the parameter $(R_m/R_0)^3$ by a factor 10. This would certainly take it more toward the regime of weakly coupling or at least assume the ambient ions have not significantly affected the fields.

The exchange of argon for helium was made and a data plane identical to that of Fig. 4.11 was taken and is shown in Fig. 5.6. Radial cuts extracted along the line $y = 0$ cm are shown in Fig. 5.7. Comparing these two figures to Fig. 4.10 and Fig. 4.11 show that the electrostatic fields are qualitatively identical and quantitatively in good agreement. This shows that the electrostatic fields are not sensitive to M_A as it approaches 1 and that the nature of the momentum and energy coupling are not qualitatively changed by this fact. Since the electric fields did not significantly change, the amount of coupling does change. If the helium is stationary during the acceleration process just as the argon essentially is, the helium ions can gain up to 10 times the velocity of the argon ions or 10 times the energy based on their mass ratio. So a decrease in M_A leads to a larger exchange of energy. Two explanations exist for this but they are not mutually exclusive. First, the condition $M_A = 1$ is not a critical parameter for the case of a high-β expansion and the appropriate critical value of M_A depends on some other parameter. The second is that the electrostatic field and coupling depend more on $\left(R_q/R_0\right)^3$ than on $(R_m/R_0)^3$. In the case of chapter 4 and the helium case, $\left(R_q/R_B\right)^3 \gg 1$ so that the presence of the background plasma is a small perturbation in the distribution of charge. Reaching the condition $\left(R_q/R_B\right)^3 \sim 1$ to see if this is the case is not realistic for the laser in this experiment and LAPD's discharge parameters.

Chapter 6 – Discussion and Conclusion

6.1—The Weak Coupling Case

The Rayleigh model as presented in §2.3 is a very simplistic view of a high-β expansion. It nevertheless yields the characteristics that have been repeatedly observed in similar experimental setups such as those in Figs. 2.3 & and 2.4. It also yields the correct scale for the electrostatic field which was crucial in this experiment and in understanding the transfer of energy between the LPP and an ambient plasma. This should not be so surprising as it is effectively a statement of energy conservation. Its success is dependent on its most basic assumption that the primary mode of energy exchange is between the kinetic motion of the ion across the magnetic field and the magnetic field itself. Thus, it only works well in the weak-coupling case because we have assumed from the outset that the energy transferred to the ambient plasma is small compared to both the LPP ions kinetic energy and the magnetic field.

Its major fault lies in its inability to fully characterize the spatial distribution of the fields. As explained in Appendix B, this is due to the combined assumption of 0 ion pressure and a velocity field that varies linearly with the radius. This results in an unrealistically linear magnetic field profile in order to satisfy momentum conservation. From Chapter 4, the profiles are monotonic with radius out to $r = R(t)$, but its derivative is clearly not. To get the correct profile for the magnetic, velocity, and electric fields would require a model or measurement of the ion pressure including all the ion species. Since the ions are not in thermal or mechanical equilibrium and in fields with large gradients, a model for this likely anisotropic term must come from a kinetic analysis that does not assume gyromotion. This incompleteness is still better than alternative models such as the superconducting expanding sphere [20], which is not energy conserving and

therefore cannot replicate the interrelationships between τ_D, β, and R_B, or MHD models which utilize $\boldsymbol{E} = -\boldsymbol{V} \times \boldsymbol{B}$ and thermalized ions; effectively ignore the electrostatic field and its role in energy transfer. A better model than even the Rayleigh model must account for those relationships the Rayleigh model succeeds in characterizing—in particular the Hall term in Ohm's law—as well as the clear gap in momentum conservation via the ion pressure term if the general interaction between a magnetized expansion and an ambient plasma is to be understood outside of a weak-coupling limit.

The weak-coupling assumption will break down as soon as any other energy loss or storage mechanism becomes comparable to the ion kinetic energy or magnetic field energy. This is at the heart of the high-β assumption since $\beta < 10^3$ must account for the thermal energy in the ions and electrons. Similarly, when the coupling to the ambient plasma becomes large enough, it must also be accounted for. Appendix B shows, however, that an observable change in $R(t)$ due to the coupling would imply an energy sink comparable to the expulsions of the magnetic field itself. Since the collisionless coupling between the high-β expansion and the ambient plasma is a secondary effect mediated by the fields generated during the magnetic field expulsion, this would have to be an impressively efficient process and was not observed here. The relationship between the parameters R_q/R_0 and R_m/R_0 and the sources of the electric fields at the end of §2.3 suggests the way in which the field is modified in the strong-coupling limit.

6.2—From Weak to Strong Coupling

The mechanism for the formation of the diamagnetic cavity and the inter-relationships for the electromagnetic fields is well-established by the CM model of Fig. 2.2. Measured field profiles reflect that the LPP is 3D with at best azimuthal symmetry rather than planar symmetry, the flow

is from a point explosion rather than a continuous flow, and finite electron resistivity is present. Nevertheless, the electrostatic field within the diamagnetic cavity is connected to the magnetic field profiles through the Hall effect, which is dependent on the charge density and thus R_q.

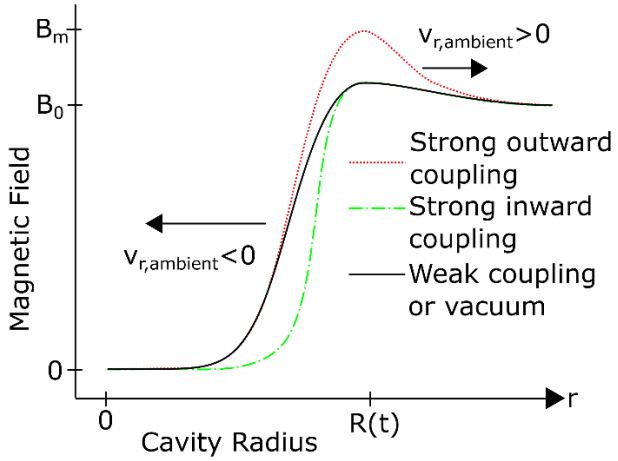

Figure 6.1: Schematics of the magnetic field profile changes from weak to strong coupling. B_m is an arbitrary peak magnetic field and $V_{r,ambient}$ depends on the electric field from the Hall effect and therefore the value of R_q.

The strong inward electrostatic field is the one responsible for removing kinetic energy from the ions and transferring it to the magnetic fields. This reflects on the motion of the LPP and diamagnetic cavity through a deceleration of the cavity expansion, $\partial_t^2 R(t)$. So if additional energy is to be lost from the expanding ions and gained by the ambient plasma, the fields must respond in such a way as to increase the strength of the inward electrostatic field. There are two changes in the magnetic profile that achieve this and they are shown schematically in Fig. 6.1. The black line is the weak coupling or vacuum profile that reflects the features observed in Fig. 4.7. The diamagnetism then leads to an inward electrostatic field which pulls ions inwards and the

compression leads to an outward electrostatic field. In the first case of strong inward coupling, the presence of additional charge from the ambient plasma creates a narrower magnetic sheath with no increase in magnetic field compression. This would further increase the rate at which ambient ions are pulled in against the LPP expansion but produce no additional outflow. The second case of strong outward coupling is when the magnetic field becomes further compressed. Here, no additional electrons from the ambient plasma make it into the diamagnetic cavity but rather ambient ions begin to be pushed outward. The behavior of the electrostatic fields in this outward coupling case, specifically the ratio of the outward to inward approaching 1, is essentially what was observed in Fig. 5.1 at low B since the outward field strength and R_q are independent of B. Both cases of strong coupling lead to extraction of energy from the LPP ions and transferring it to the ambient ions. If sufficiently strong, both would be accompanied by a decrease in the curve $R(t)$ below that of the Rayleigh model. The dependence of the Hall effect on electron density means the strong coupling scenarios would appear as R_q approaches R_B. If $R_q \ll R_B$, the strong outward coupling case would have the magnetic field and electrostatic field being carried by the ambient plasma and escaping the ions that initially made up the bulk LPP. Such a regime allows for the possibility of launching a cylindrical magnetosonic shock for which there are decades worth of theoretical work in the planar case (see works such as Tidman and Krall 1973 [75]).

Magnetosonic shocks are mediated by the electrostatic Hall field rather than the induced field from the Lorentz term in Ohm's law. The opposite is true for MHD or Alfvénic shocks where the electrostatic field is generally ignored. Both require super-Aflvénic speeds. The condition $M_A > 1$ corresponding to $R_m/R_B < 1$ is reduced to a necessary but not sufficient condition to observe strong collisionless coupling leading to a shock. The limits of the LAPD discharge,

however, mean that to access this regime, a higher charge density in the ambient plasma or a far larger expansion velocity is needed than the cases presented in Chapters 4 and 5.

6.3—Summary of Physics

Experimental measurements were made of the electromagnetic fields including the first measurements of the electrostatic field generated by a high-β LPP ($\beta \sim 10^6, \omega_{ci}^d \tau_D \approx 0.3$) embedded within a uniform, 750-Gauss magnetic field and ambient argon plasma. They showed the detailed structure of the expansion phase of a diamagnetic cavity as well as the qualitative effects of the collapse phase. The induced electric field was calculated from the measured magnetic field utilizing the azimuthal symmetry of the expansion. The largest component of the induced electric field was found to be less than its predicted value, $E_{ind}(\text{exp}) \leq 30$ V/cm $< E_{ind}(\text{theor}) \leq 100$ V/cm. This was attributed to the essentially late-time observation of the cavity since the field strength decreases monotonically with time and also the neglect of resistive effects which became increasingly important with time. The peak, inwardly directed electrostatic field strength, $E_{st} \sim 180$ V/cm, was found to be consistent with the Hall effect in the diamagnetic cavity for the LPP expansion conditions and an average carbon charge state of $\langle Z \rangle = 2$. The large ratio of E_{st}/E_{ind} and their directions suggest that collisionless coupling between the LPP and the ambient plasma is mediated by the electrostatic field and directed inward against the expansion.

The electrostatic field measurements also revealed the presence of a radially outward directed field exterior to the diamagnetic cavity and a highly collimated electrostatic pulse that precedes the LPP and diamagnetic cavity which follows the background magnetic field. The outward electrostatic field was about 1/3 of the magnitude of the inward electrostatic field but rapidly diminished in strength after peak diamagnetism. The estimated Hall effect from the

observed compression and LPP electrons at the furthest radial extent was consistent with the strength of this field suggesting the compression was generated by a mechanism internal to the LPP. The source of the outward field was deduced to be an imbalance in the ion and electron charge layers within the diamagnetic cavity that neutralizes at the boundary along the background magnetic field. This implied a close relationship between this cross-field structure and the electrostatic pulse, which was also connected to previous observations of field-aligned, fast electrons, $v > 10^8$ cm/s.

Using detailed experimental results of high-β LPP expansions, a Rayleigh model was developed based on energy exchange between the ions in the expansion and the magnetic field. From it were derived scaling laws for the laminar electrostatic and induced electric fields as well as a description of their time evolution. This model only captures the dynamics of the primary electric fields, $\partial_r \phi$ and $\partial_t A_\phi$, in the diamagnetic cavity but is consistent with those that were measured. The salient features of this model showed that two regimes exist that separate the ways ambient plasma ions react to a high-β expansions in the absence of collisions:

(1) $\omega_{ci}^d \tau_D \gg 1$, the ambient ions spin up in a direction opposite to the diamagnetic current under the influence of the sustained induced electric field. This regime may also allow for gyromotion if the fields are sufficiently stationary and uniform.

(2) $\omega_{ci}^d \tau_D \ll 1$, the dominant electric field is electrostatic in nature and acts primarily to pull in the ambient ions against the expansion direction.

Historically, experiments that have examined diamagnetic cavities of LPPs have been closer to the second regime. Since $\omega_{ci}^d \tau_D \sim B_0^{1/3} V_{r0}^{2/3}$, only the fastest, most magnetized, smallest, and therefore hardest to diagnose expansions have approached the former condition. Under the assumption of

weak-coupling, these electric fields allow the calculation of the amount of energy and momentum injected into the ambient plasma.

The combined effect for the measured fields was estimated from the Rayleigh model to produce an inflow of argon ions moving at $v_r \sim -8 \times 10^5$ cm/s with essentially no azimuthal flow. Using an LIF diagnostic, which directly probed the argon ion velocities, the observed motion of the ambient argon ions was indeed radial during and after the expansion although the drift speeds were about 40% of the expected value. Even the effect of the outward electrostatic field was detectable by a small outward drift near the radial edge of the LPP and of an appropriate magnitude relative to the inward drift, $v_{out} \approx v_{in}/3$. This drift was too small to be maintained and eventually the inward electrostatic field and its corresponding drift dominated. The total amount of energy that this represents as a fraction of the initial expansion energy is about 1/2000.

Under variation of the ambient magnetic field, the inward electrostatic field appeared to drop in magnitude faster than the expected scaling from the Rayleigh model, $E_{st} \sim B^{2/3}$, and was almost linear in B. The outward electrostatic field and the field from the electrostatic pulse exhibited very little variation with magnetic field. This suggested that low-field expansions may be dominated by an outward flow of argon ions mediated by the outward electric field since both the inward field and induced electric field go to zero with B. Dropping B without changing the LPP or ambient plasma amounted to reducing the parameters R_q/R_B and R_m/R_B toward the strong-coupling limit.

With a change in ambient plasma to helium, the electrostatic structure and diamagnetic cavity did not exhibit significant, observable differences. Under these circumstances, the electric field could have produced an inflow of helium ions with up to 10 times the speed of the argon ions

or 10 times the energy. This upper bound is under the assumption that helium, like argon, remains stationary during the acceleration and receive an instantaneous impulse. This further showed that the Alfvén Mach number, $M_A = 1$ or equivalently $R_m/R_B = 1$, which was the case in argon, is not indicative of a significant change in qualitative behavior nor does it imply strong-coupling. In helium, $M_A < 1/3$ but the field structure is such that more energy is transferred from the LPP to the helium ions.

When the expansion was directed across the magnetic field, an additional component to the electrostatic field appeared in the form of a translational polarization. This complicates the qualitative picture of the diamagnetic cavity and the azimuthal symmetry is destroyed. Further, this field survives the collapse of the diamagnetic cavity as the plasma continues to move across the magnetic field. In this manner, it is essentially distinct from the other fields associated with the expansion. The effect this field has on the ambient ions is not easily distinguished from the induced electric field of the diamagnetic cavity since they both have their origin in cross-field motion and they work synergistically at the front edge of the expansion. The lack of symmetry means that barring 3D current measurements, the two can only be compared along the ray connecting the expansion's origin to the front edge and must otherwise be considered together.

Finally, the structure of the cavity fields is used to construct a qualitative picture of how the strong-coupling limit associated with the parameters regime $R_q \ll R_B$, $R_m \ll R_B$ affects the diamagnetic cavity fields and mediates the exchange of energy between the LPP and ambient plasma.

6.4—Future Work

The Rayleigh model provides a good context for which further scaling studies could be pursued. In particular, the regime in which R_q/R_B and R_m/R_B both drop well below 1, i.e. the strong-coupling regime, has not been systematically studied. In the limits $R_q/R_B, R_m/R_B \to 0$ there is the possibility of observing the electromagnetic analog of a blast wave for which the equivalent requirement is that $M_s \to \infty$ where M_s is the sonic Mach number. Variation of these parameters would require a great deal of control over the ambient plasma and adjustment for any changes in magnetic field. The best way to reach this regime is with the use of a massive neutral gas. If control of the average ionization is possible or at least accounted for, this would allow R_q/R_B and R_m/R_B to be separately varied with values below 1 in a lower magnetic field environment and lower ambient density than more traditional gases such as hydrogen or helium. The increase in R_B due to the lower B would make spatial resolution of the fields easier while the reduced density may allow for a smaller, simpler emissive probe design that would be less intrusive. The low field would also give further room for varying $\omega_{ci}^d \tau_D$ and possibly reaching the regime where $\omega_{ci}^d \tau_D \gg 1$. It is here that the expansion energy might be more efficiently transferred to an azimuthal motion of the ambient plasma. Xenon would work well for making field measurements in these regimes. It also has several, well-established LIF schemes though its high mass would make detecting the ion motion difficult without also observing a strong, long-lived electric field.

A further experiment, which is also implied by the Rayleigh model, is to study the motion of the cavity after the collapse. In fluid cavities, the boundary, $R(t)$, exhibits oscillatory motion. This is due to the very efficient recapture of energy as the cavity collapses. Specifically, the losses from radiation of sound waves or viscous damping are generally small. These losses can, however,

affect the amplitude and even the frequency of the oscillations [76]. For plasmas, Bhadra [77] predicted that the diamagnetic cavity from an expansion such as an LPP should undergo a similar oscillatory motion. His theory was highly dependent on a choice model of the magnetic field profile and assumed the diamagnetic cavity arose out of the thermal pressure of the electrons, β_{th}. Here, the electrostatic field slows down the carbon ions which eventually leads to stagnation of the diamagnetic cavity. But the electrostatic fields persist as long as $2\tau_D$, during which time, the LPP ions as well as entrained ambient ions are accelerated back inward. Thus, the ions recapture some energy, collapse back onto the axis, and can potentially start the whole process over again, albeit with a reduced β due to energy losses. These oscillations were reportedly observed by Tuckfield [78] and Fabre [27] through limited visible emission measurements and a measurement of the magnetic field at a point. No one, to my knowledge, has observed more than 1 subsequent, large oscillation of the cavity, LPP, or the change in their internal structures. Both those experiments utilized very strong magnetic fields and had slow center of mass motion such that the LPP remained near the target region long enough to observe the formation of a second cavity; the time between cavity oscillations being roughly approximated by $2\tau_D$. The LAPD has good diagnostic access along the axial direction so that this phenomena could be re-examined experimentally in the context of the results of this dissertation. Since the fluid cavity is an equilibrium gas in an isotropic pressure field while the high-β plasma expansion is driven by ion particle motion in an anisotropic pressure field, there are sure to be interesting differences.

Appendix A – Unmagnetized Expansion

There are a number of physical processes involved in the expansion phase of the LPP. To account for them all accurately would require a 3D, multiscale simulation of either an unbounded system or a grid that adapts to the growing system. Such a simulation would probably be a thesis on its own. Instead, by considering the physics separately, we can qualitatively combine their results and reconcile them with the well-tested, experimental scaling laws. This will not give us very accurate but rather is meant to give a sense of scale and behavior of the thermodynamic quantities. The first process is generating the expanding flow.

A.1—Initiating the Expansion

The seed plasma (see Fig. 2.1a) is a high density plasma wherein collisions prevent the electromagnetic fields internal to the plasma from dominating the particle behavior. In this description, the plasma is effectively a fluid and the expansion flow proceeds in a manner similar to that of a gas expanding into vacuum. There is one significant difference though. The initial thermal equilibrium between the ions and electrons means that electrons will make larger excursions into the vacuum than the ions. This motion of the electrons sets up an electric field which mediates energy transfer to the ions. This exchange of energy from an internal thermal source to motion of the plasma is described by

$$\partial_t E_{tot} = 0 = \partial_t \left(\frac{1}{2} m_i n_i V_i^2 + \frac{3}{2} n_i T_i + \frac{3}{2} \langle Z \rangle n_i T_e \right) \approx m_i n_i V_i \partial_t V_i + n_i \partial_t (\langle Z \rangle + 1) T_e,$$

where E_{tot} is the total energy in the expansion; $m_i, n_i, T_i, V_i, \langle Z \rangle$ are the ion mass, density, temperature, velocity, and average charge; and T_e is the electron temperature. The right-hand-most

form is arrived at by applying quasi-neutrality of the plasma and maintaining thermal equilibrium between the ions and electrons. The above equation is also that of an adiabatic gas expansion where the effective gas temperature is $(\langle Z \rangle + 1)T_e$ and the gas velocity is that of the ions alone since the electrons do not provide inertia. The main feature is that acceleration of the ions comes at the expense of electron thermal pressure.

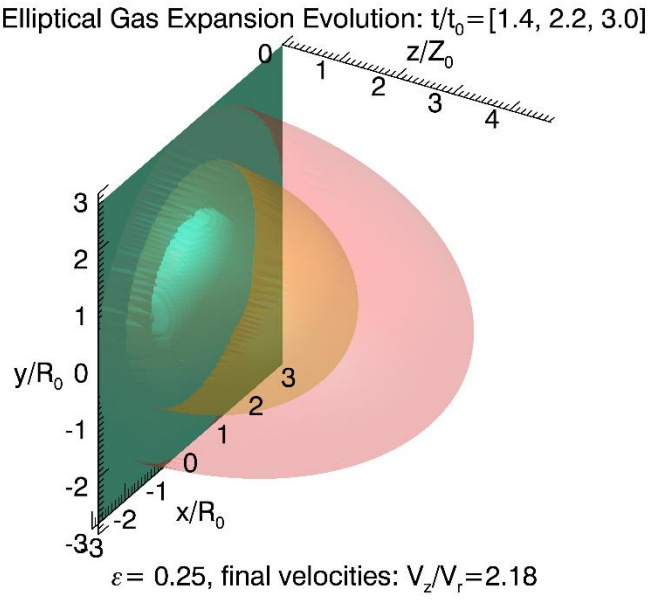

Figure A.1: Half-plane visual of oblate spheroid expansion. An extreme value of ϵ was chosen to more clearly show the asymmetry that develops.

A lot of work was done in analyzing such expansions in the 1950s and 1960s by those concerned with extremely high pressure explosions. One technique was to consider different regular geometries and simply ignore the fine structural details. Such a model reduces the amount of information that needs to be considered and allows for easily calculable solutions.

Nemchinov [14] used this technique to analyze the expansion of regular ellipsoids of gas into vacuum.

In his 1965 paper, Nemchinov found that the smallest dimension initially becomes the largest and fastest expanding dimension as $t \to \infty$ as shown in Fig. A.1. The characteristic speed of such an expansion is the initial sound speed of the gas, C_{s0} and the characteristic time evolution of the variables is the hydrodynamic time defined as

$$t_0 \equiv \frac{R_0}{C_{s0}}.$$

The expansions he characterized are inherently self-similar and for times much longer than the hydrodynamic time (actually as will be seen $t \sim 5t_0$ is enough), they become essentially free expansions. That is no force further drives the ions.

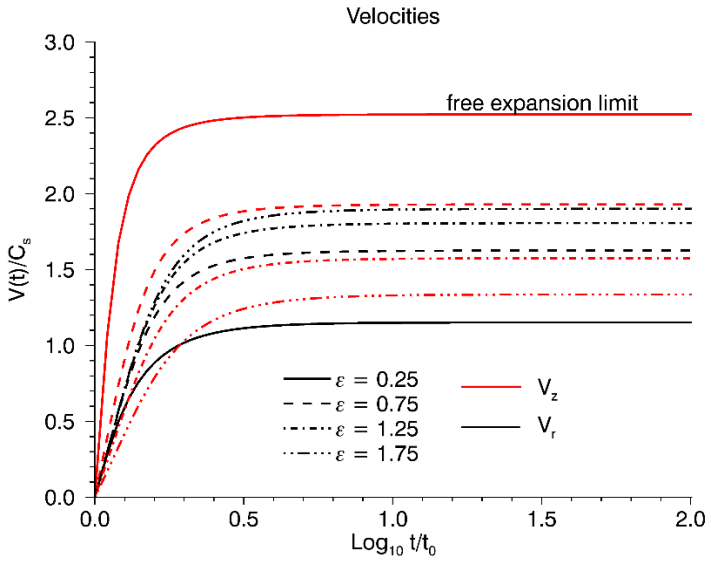

Figure A.2: Variation of velocities of ellipsoids, V_z and V_r, time.

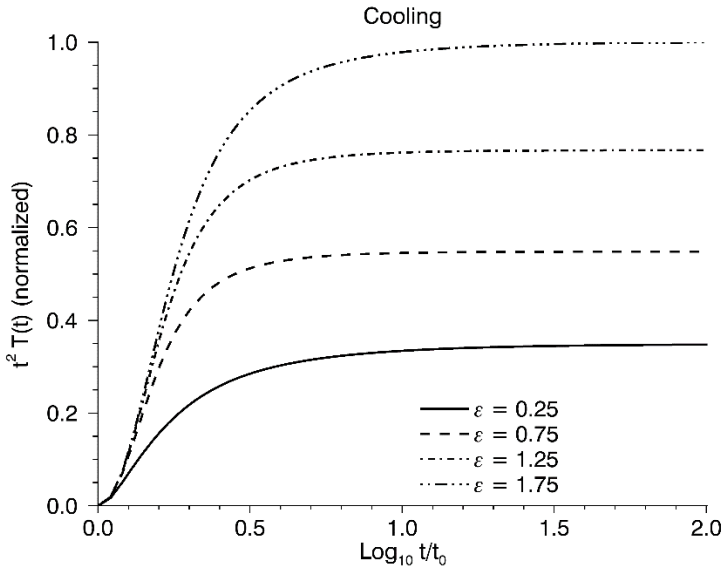

Figure A.3: Time variation of temperature of ellipsoid.

Asymptote is free expansion limit, $T_e \sim t^{-2}$.

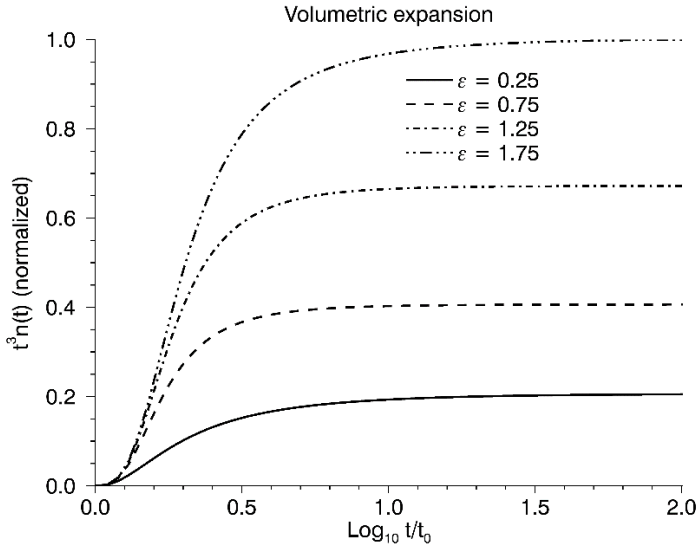

Figure A.4: Time variation of average density in ellipsoid.

Asymptote is free expansion limit, $n \sim t^{-3}$.

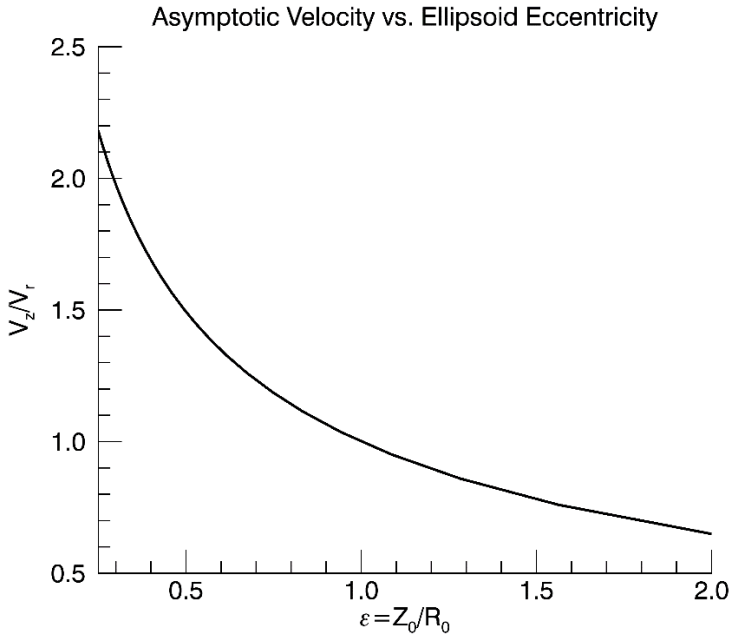

Figure A.5: Asymptotic ratio of V_z/V_r versus the eccentricity of the seed plasma geometry.

For an eccentricity of the seed plasma, $\epsilon \equiv Z_0/R_0 < 1$, the long-time behavior of the fluid variables can be summarized with

$$V_r \sim \alpha C_{s0}.$$

$$V_z \sim \frac{C_{s0}}{\zeta},$$

$$n_i \sim n_{i0}\left(\frac{t_0}{t}\right)^3,$$

and

$$T_e \sim T_{e0}\left(\frac{t_0}{t}\right)^2,$$

where α and ζ are constants less than 1. The latter two relations being consistent with a pure adiabatic expansion of a gas with $\gamma = 5/3$. Example plots of the approach of these quantities to their asymptotic values are shown for a reasonable values of ϵ in Figs. A.2-A.4. As can be seen in these figures, the asymptotic behavior for the fluid variables are all reached on time scales $t_{asym} < 10t_0$. This is the primary motivation for restricting the Rayleigh model of §2.2 and this thesis to $\beta = (\tau_D/t_0 1.402)^3 > 10^3$. For $\beta < 10^3$, ∇p_e can be as large as ∇B^2 conflating the electric fields of the diamagnetic cavity with those that are accelerating the expansion. Figure A.5 shows the variation of the asymptotic values of V_z/V_r as a function of ϵ.

The results of Fig. A.5 show that by increasing the radius of the LPP or laser focus, one can speed up the expansion normal to the target or slow its lateral expansion. The value Z_0 itself is not entirely independent of R_0 and is set by the laser-solid interaction—a far harder problem that in fact depends on R_0. The variation of the target-normal speed with beam radius was noted as early as 1981 [35, Fig. 2] and is qualitatively consistent with the above description. No connection was made to this model of high temperature gas expansions despite [14] and other results of gas expansions coming at least 2 decades earlier. Unfortunately, due to the parameters Grun and colleagues focused on at the time, neither the penetration depth nor the lateral expansion were noted and so a direct comparison is not possible. This effect of increasing the normal velocity by shrinking the normal scale is essentially what is observed in thin target, high-power, ultra-short laser experiments but is amplified due to the presence of non-thermal electrons. In that context it is called target-normal sheath acceleration [3]. The resulting asymmetry in the expansion and the presence of the solid target leads to the geometry of Fig. 2.1b. There is now a distinct difference between the velocities in the target-normal, V_n, and the target-tangential, or radial, directions, V_r. From Fig. A.5, this difference is generally of order unity unless ϵ is very far from

1. The presence of the targets acts as a boundary to half the expansion and so a net mass flow away from the target is generated with a characteristic velocity, V_m. This may give the plasma a shape that looks like an intermediate case between a hemi-spherical expansion from the surface and a pure translation of an elliptical mass. When the magnetic field is considered, it is the presence of this third velocity that limits the available symmetries. That is, if $\boldsymbol{V}_n$ and $\boldsymbol{V}_m$ are aligned with $\boldsymbol{B}_0$, $\boldsymbol{V}_n \times \boldsymbol{B}_0 = \boldsymbol{V}_m \times \boldsymbol{B}_0 = 0$, there is a cylindrical symmetry, but if $\boldsymbol{V}_n \cdot \boldsymbol{B}_0 = 0$, then so is $\boldsymbol{V}_m \cdot \boldsymbol{B}_0$ and the only possible symmetry is that along the direction $\boldsymbol{V}_m \times \boldsymbol{B}_0$ in the frame of the moving mass. In studies conducted by Collette [31] where $\boldsymbol{V}_m \cdot \boldsymbol{B}_0 = 0$, the magnetic fields maintained a spherical shape and appeared to translate itself across the magnetic field. The rather short lifetime of the expansion and apparently small V_m prevented clear separation from the target.

The variation in the electron temperature and density very early in time was confirmed in experiments by Puell [79] with Thompson scattering and Boland [80] with spectroscopic measurements; both concluding that the $\gamma = 5/3$ adiabatic expansion was roughly followed for $t < 10t_0$ and Puell even adopting Nemchinov's model [13]. However, temperature measurements later in time proved more difficult as a volume element of plasma could not easily be followed with the diagnostics. Rumsby [53] using a different technique found that later in time, the density still followed $n_i \sim t^{-3}$ but the temperature followed $T_e \sim t^{-1}$. This suggested an energy input in the system to break away from the adiabatic behavior with the most likely candidate being 3-body recombination.

A.2—Three-body Recombination

At the initial densities and temperatures, the LPP is very highly ionized and the electron-ion collision time, τ_{ei}, usually satisfies $\tau_{ei} \ll t_0$. Furthermore, in an adiabatic expansion with $\gamma =$

$5/3$, τ_{ei} is independent of time. This fantastic amount of collisionality combined with cooling implies rapid recombination. Dielectric recombination and radiative recombination results in photons which either immediately escape or diffuse to the surface and radiate as blackbody emission. These two types of recombination do not significantly affect the plasma temperature, but the rapid drop in temperature allows for 3-body recombination to eventually take over. This is due to the strong scaling with density and temperature of 3-body, $\partial_t n_{e,3body} \sim n_e^3 T_e^{-9/2}$, compared to the two-body mechanisms, $\partial_t n_{e,2body} \sim n_e^2 T_e^{-3/4}$ [81].

Three body-recombination acts as a heat source because the excess momentum and energy that would have been carried off by the photon is instead returned to a free electron. This effect keeps the electrons slightly hotter than the purely adiabatic case, reduces τ_{ei} over time, and allows the electrons and ions to thermally decouple. Further, 3-body recombination also leads to the phenomenon seen in plasma expansions of "frozen-in" ionization. This is roughly defined as an anomalously slow rate of change of average ionization on the time scale of the expansion, $\partial_{\ln t}\langle Z\rangle \to 0$. A good, semi-classical explanation of how this works can be found in a [82] or [83, pg. 406]. Experiments by Roudskoy [84] showed, however, that the original semi-classical models predicted too high of an ionization stage late in time for an LPP expansion and an improved model was derived. Their model included the result that all initial conditions of $(\langle Z\rangle, T_e)$ lead asymptotically to $\partial_{\ln t}\langle Z\rangle = 0$ and $T_e \sim t^{-1}$. Figure A.6 shows the flow field of $(\partial_{\ln t} \ln\langle Z\rangle, 2 + \partial_{\ln t} \ln T_e)$ where the derivative of a quantity, Q, that has a power-law variation, $\partial_t Q = t^{p-1}$ where $p = p(t)$, can be succinctly described by $p = \partial_{\ln t} Q$. Thus the x and y axes in Fig. A.6 are, respectively, the time-dependent exponents for $\ln\langle Z\rangle$ and $T_e t^2$. All solution trajectories in Fig. A.6 fall towards $\ln\langle Z\rangle = \text{const}$ and $T_e \sim t^{-1}$. Figures A.7 and A.8 show the explicit time dependence of T_e and $\langle Z\rangle$ respectively for realistic LPP parameters. Accounting for 3-body recombination, the

scale time for the temperature and charge state is still t_0 but they no longer reach their asymptotic behavior in a time comparable to t_0 and a calculation must be performed for each initial condition. For the LPP parameters given in §3.1 and the time scales that will be of interest to the diamagnetic cavity, $t > 100$ ns, $T_e \sim 1$ eV $\sim t^{-1}$ and $\langle Z \rangle \simeq 2 \approx$ const.

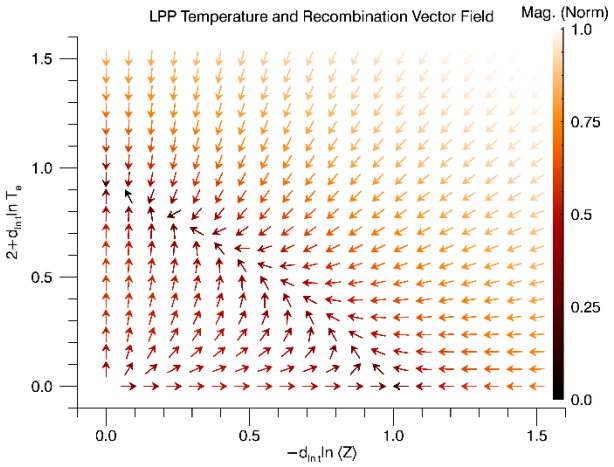

Figure A.6: Flow field of time of electron temperature vs. time rate of average ionization.

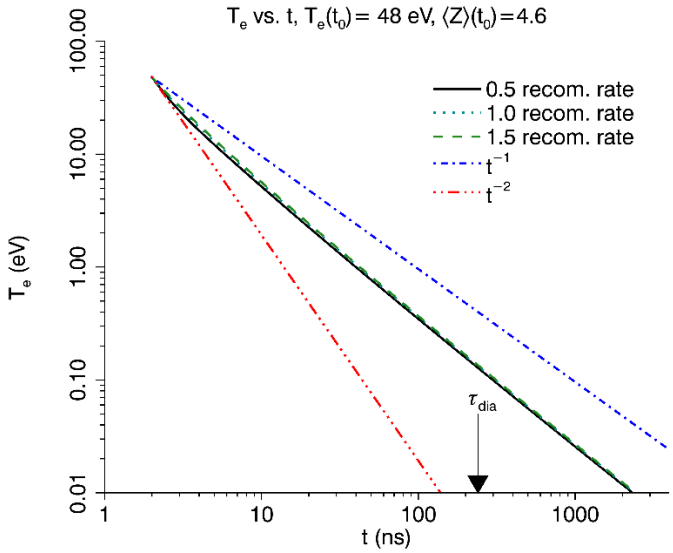

Figure A.7: Variation in time of electron temperature for hydrodynamic parameters $(t_0, T_{e0}, \langle Z \rangle_0) = (2\text{ ns}, 48\text{ eV}, 4.6)$. Also shown, curves with 50% error in recombination rate, t^{-1} variation, and t^{-2} variation.

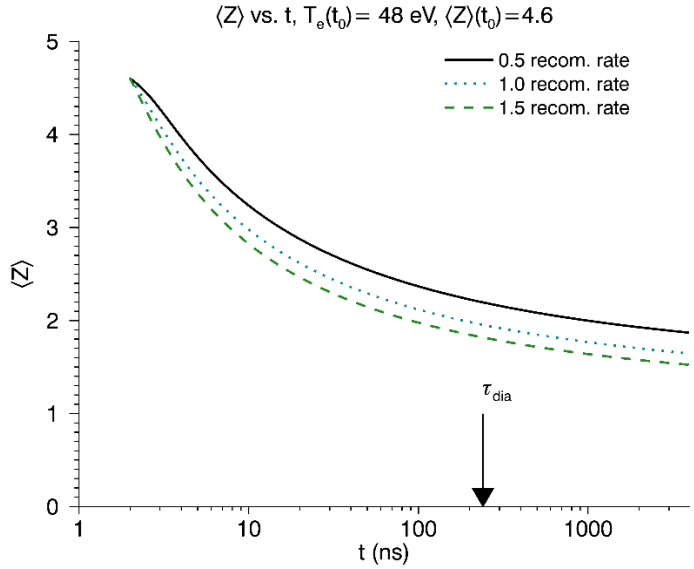

Figure A.8: Variation in time of ⟨Z⟩ for same parameters as Fig. A.7.

A.3 –A note on free expansion

It is often quoted that an ideal gas in free expansion does no work and so remains isothermal unless there is a heat loss. Joule's famous experiment, upon which this statement is based, had a number of issues (his thermometer had a much higher thermal capacitance than his working gas!), but the big assumption that is made is that the gas remains in thermal equilibrium and is ideal. This is a good approximation so long as the expansion remains subsonic, but the LPP attains an expansion velocity comparable to the initial sound speed at the expense of its thermal energy. Thus, the expansion is always supersonic and thermal equilibrium is not guaranteed. T_e can still be considered as a good thermodynamic quantity because the electron thermal speed is always greater than C_{s0} and electron collisions remain high. The ions, on the other hand, are always superthermal and are only in good thermal contact with the electrons so long as $\tau_{ei} \ll t_0$.

Accounting for the relativity minor heating from 3-body recombination can easily make $\tau_{ei} > t_0$. The ions are not guaranteed to be in any thermal equilibrium.

Nemchinov's results show that the free-expansion is an asymptotic state of the carriers of inertia (ions) of the adiabatic expansion of the plasma (ions + electrons). Even at late times, T_e is still changing and the LPP is still accelerating, just at a vanishingly small rate. Compare this to the ideal isothermal and free expansion where strictly neither T_e nor the LPP velocity change at all in an ideal gas. The distinction becomes entirely academic. This state of ambiguity between the isothermal free expansion and adiabatic expansion is achieved on time scales of $t \sim 10\ t_0$ and the interactions with which this thesis is concerned occur for $t > 10\ t_0$ or generally later. This is why the expansion during the diamagnetic cavity can be characterized as isothermal, free, and adiabatic without making a significant mistake in description of the physics. To be more exact in the description, the ions at late times are free, the electrons are approximately isothermal, and the whole plasma is approximately adiabatic.

Taking the extreme interpretation of these different types of expansions can have serious consequences—the worst coming from the isothermal characterization. Even though the free expansion stage can be effectively modelled as isothermal in certain circumstances, the "correct" temperature is dramatically lower than the initial temperature of the LPP. The residual, small time variation can lead to qualitatively different results. Koopman 1976 [57] quoted temperatures of 1 eV (no field) and $40 - 80$ eV (700 G field) for an LPP with only slightly more energy than the one in this dissertation ($\sim 6\ J$ laser pulse). This amounts to almost 3 orders of magnitude difference in electrical resistivity. Using a temperature of 4 eV (still an order of magnitude different resistivity from a 1 eV plasma), they calculated that anomalous resistivity was needed to explain the collapse of the diamagnetic cavity in an LPP. This was the first paper, as far as I have been able to find,

that claimed to have observed the dominance of anomalous resistivity. This concept subsequently found its way into many papers on diamagnetic cavities. Koopman's calculation neglected the manner in which the LPP decelerates, neglected the possibility of convective collapse, and missed the strong effect the time-dependence of the electron temperature has on resistive effects. All of these are shown in Chapter 4 of this dissertation to be important features in the structure and behavior of the LPP and diamagnetic cavity.

Appendix B—

Coupling in the Rayleigh Model

B.1—Additional Losses of Energy

To account for the addition of an ambient plasma with which the LPP can interact, we can add another term that accounts for energy loss to the ambient plasma. Since the energy loss would be proportional to the volume of ambient plasma that the LPP has displaced, the effect will be similar to an effective pressure on the system. This will in general reduce the value of τ_D and the corresponding maximum diamagnetic cavity size from R_B to some other value R_D. It must be reminded that this effective pressure is not a pressure in the sense of a force acting on a volume element of a fluid—we are only considering energy loss or storage mechanisms. Rather in the collisionless case, the electric field would be altered by the presence of the ambient plasma and react to exert the necessary force on both the LPP and ambient plasma simultaneously and not necessarily in a linear manner. If we neglect at first the time and spatial dependencies of this effective pressure, p_{ext}, the same analysis that gave Eq. 2.2 yields,

$$d_\tau \tilde{R} = \sqrt{1 - \frac{1 + p_{ext}/p_B}{\beta}(\tilde{R}^3 - 1)}, \tag{B.1}$$

and we can define a third characteristic length scale,

$$R_p \equiv \left(\frac{p_B}{p_{ext}}\right)^{\frac{1}{3}} R_B = \left(\frac{\frac{C}{2} m_i N_i V_{r0}^2}{p_{ext}}\right)^{\frac{1}{3}}.$$

The cavity now reaches the radius

$$R_D = \frac{R_B R_p}{\left(R_B^3 + R_p^3\right)^{1/3}} = \frac{R_B}{\left(1 + \left(\frac{R_B}{R_p}\right)^3\right)^{1/3}}$$

Where R_B now refers to the radius of the diamagnetic cavity under vacuum or weak coupling conditions. The condition for strong coupling, $R_p < R_B$, is difficult to reach without collisions since it implies the diamagnetic fields transfer energy away more efficiently than they receive it.

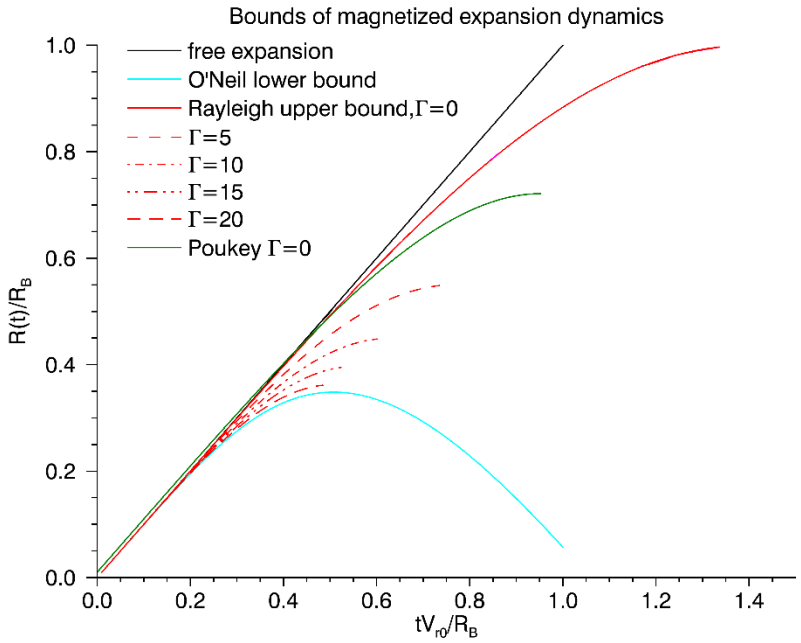

Figure B.1:LPP/diamagnetic cavity trajectories for various external pressures, $\Gamma \equiv p_{ext}/p_B$, according to a Rayleigh gaseous bubble model. Poukey [86] accounted for the effect of losses along the field (elliptical expansion rather than spherical) and O'Neil [85] calculated the minimum boundary from a Virial Theorem analysis.

To see how the cavity grows in time, we numerically solve Eq. (B.1) and allow for various external energy loss mechanisms. Figure B.1 shows the solutions for varying external energy sinks

relative to the magnetic field energy, $\Gamma = p_{ext}/p_B$. Also shown are the free expansion, a Virial theorem analysis of this problem [85] in blue, and an asymptotic expansion derived from a Lagrangian fluid approach [86] in green. As stated in [cite O'Neil], the curve from the virial theorem is an absolute minimum and as such represents an expansion impeded by a strong shock or instability. This is also the curve that the Rayleigh model is approaching in the limit that $\Gamma \rightarrow \infty$. Note however, that for a drop of a factor 2 in radius, the additional, external pressure has to be 5 times stronger than that due to the magnetic field which may suggest that there is already a shock.

B.2—Scaling for p_{ext} in the Weak Coupling Limit

The electric fields from the Rayleigh model were described in §2.3. Using them, the effective impulse an ion would receive from them can be calculated and an estimate for the scaling of p_{ext} with the expansion parameters can be obtained. Repeating Eqs. 2.3, 2.4,

$$|\boldsymbol{E}_{ind}| = \partial_t R\, B \approx \frac{m_{di} V_{r0}^2}{Z_d e R_B}\left(\frac{\omega_{ci}^d \tau_D}{1.402}\right) d_{\tilde{t}} \tilde{R} \tag{2.3}$$

and

$$|\boldsymbol{E}_{st}| = \frac{m_{di}}{Z_d e}|\partial_t^2 R| = \frac{3}{2}\frac{m_{di} V_{r0}^2}{Z_d e R_B}\frac{\tilde{R}^2}{\beta^{2/3}}. \tag{2.4}$$

It will be more convenient to work with these fields in dimensionless quantities and using the peak diamagnetism spatial scales. With the transformations $R' = R(t)/R_B$, $r' = r/R_B$, and $t' = t/\tau_D$ and normalizing the electric fields to $E_0 \equiv m_{di} V_{r0}^2/Z_d e R_B$, we have

$$\boldsymbol{E}' = \frac{\boldsymbol{E}}{E_0} = \alpha_\phi \partial_{t'} R' f\left(\frac{r'}{R'}\right)\hat{\phi} - \frac{3}{2} R'^2 g\left(\frac{r'}{R'}\right)\hat{r}$$

where f and g represent the profiles of the induced and electrostatic fields, respectively—assuming such self-similar profiles can exist—and $\alpha_\phi = \omega_{ci}^d \tau_D/(1.402)^2$. If we assume the ions do not move significantly during the acceleration process, we can neglect $\boldsymbol{V} \times \boldsymbol{B}$ in the Lorentz force and the ambient ions at position r, which are initially at rest, end up with the velocity

$$\Delta \boldsymbol{V}(r,t) \approx \frac{Z_a e}{m_{ai}} \int_{R(t)=r}^{t} dt \boldsymbol{E} = 1.402 \frac{Z_a m_{di}}{Z_d m_{ai}} V_{r0} \int_{R'(t')=r'}^{t'} dt' \boldsymbol{E}'(r',t'). \tag{B.2}$$

Such an approximation is only good if $|\Delta \boldsymbol{V}| \ll \partial_t R \sim V_{r0}$. If the peak electric field values are less than E_0, this condition is satisfied for ambient plasmas with smaller charge to mass ratios than those in the expanding plasma. If the electric field profiles are mostly below E_0 and for most of the lifetime of the cavity, the integral itself will be small and the charge to mass ratio requirement is relaxed.

The total energy transferred to a sphere of a uniform, ambient plasma is

$$E_c(t) = 4\pi m_{ai} n_{ai} \int_0^{R(t)} dr r^2 \left(\Delta \boldsymbol{V}(r,t)\right)^2$$

$$= 4\pi m_{ai} n_{ai} \left(1.402 \frac{Z_a m_{di}}{Z_d m_{ai}} V_{r0}\right)^2 R_B^3 \int_0^{R'} dr' r'^2 \left(\int_{R'(t')=r'}^{t'} dt' \boldsymbol{E}'(r',t')\right)^2.$$

Substituting $I(t')$ for the whole integral on the right-hand side, a more convenient form to consider will be

$$E_c(t) = \frac{6(1.402)^2}{C} \left(\frac{Z_a m_{di}}{Z_d m_{ai}}\right) \left(\frac{4\pi}{3} \frac{Z_a n_{ai}}{Z_d N_d}\right) \left(\frac{3}{4\pi} \frac{C m_{di} N_d V_{r0}^2}{2}\right) \frac{4\pi R_B^3}{3} I(t'). \tag{B.3}$$

These are in general very complicated equations assuming even that the profile for the electric fields represent realistic profiles and that they satisfy momentum conservation for the system. To

get an idea of the scaling of this coupling, we next assume that the coupling is so weak that the total energy transferred to the ambient plasma is proportional to the volume. We then have that

$$p_{ext} = \frac{3E_c(t)}{4\pi R^3(t)} \approx \frac{3E_c(\tau_D)}{4\pi R_B^3}$$

or after inserting Eq. B.3 and normalizing to p_B

$$\frac{p_{ext}}{p_B} = \frac{6(1.402)^2 D}{C}\left(\frac{Z_a m_{di}}{Z_d m_{ai}}\right)\left(\frac{4\pi}{3}\frac{Z_a n_{ai}}{Z_d N_d}\right)\left(\frac{3}{4\pi}\frac{C m_{di} N_d V_{r0}^2}{2Dp_B}\right) I(t'),$$

or simply

$$\frac{p_{ext}}{p_B} = \frac{6(1.402)^2 D}{C}\frac{\omega_{ci}^a}{\omega_{ci}^d}\left(\frac{R_B}{R_q}\right)^3 I(t'). \tag{B.4}$$

That is, regardless of the profiles or whether one component of the electric field dominates the other, the critical parameters determining how much energy is transferred to the ambient plasma are the cyclotron frequency ratio and the ratio of the equal charge radius to the diamagnetic cavity radius. For $R_q > R_B$, weak coupling, i.e. $\Gamma \ll 1$, is guaranteed under the same assumptions as those that lead to Eq. B.2. That is, unless the ambient plasma is orders of magnitude lighter than the expanding plasma.

B.3—The Problem with Momentum Coupling

No calculation of the expected $\Delta \boldsymbol{V}$ nor E_c can be made without some model for the electric field profiles. This is where the Rayleigh model loses its usefulness. In the traditional Rayleigh models for gaseous cavities, one of two profiles is used:

$$V_r = \partial_t R \frac{r}{R}, (\text{expansion})$$

$$V_r = \partial_t R \left(\frac{R(t)}{r}\right)^{d-1}, \text{(collapse)}$$

where d is the dimension of the symmetric expansion ($d = 3$ for spherical, 2 for cylindrical). They are used because of the solutions they represent for the continuity equation. The expansion form automatically results in a self-similar density that varies in magnitude as $n(r,t) = t^{-d}h(r/R)$, i.e. uniform ballistic expansion, where h is an *arbitrary* function. The collapse form represents an incompressible fluid in *d*-dimensions,

$$d_t n = (\partial_t + \boldsymbol{V} \cdot \nabla)n = 0.$$

Unfortunately, when the expansion form is put into the single-fluid momentum equation,

$$\rho_m d_t \boldsymbol{V} = \rho_m(\partial_t \boldsymbol{V} + \boldsymbol{V} \cdot \nabla \boldsymbol{V}) = \rho_m \frac{r}{R} \partial_t^2 R = \rho_c \boldsymbol{E} + \boldsymbol{J} \times \boldsymbol{B} - \nabla \cdot P_i.$$

The acceleration must be non-zero at $r = R(t)$. Barring the allowance of an infinite shear in $\boldsymbol{J}$, $\boldsymbol{J} \times \boldsymbol{B}$ (as well as $\boldsymbol{E}$) must go to zero. Also, if there is a magnetic compression, then $\boldsymbol{J} \times \boldsymbol{B}$ does go to zero. This just means that the expansion form is not a realistic solution but any other velocity profile does not satisfy the self-similar ballistic expansion that is commonly found or used in LPP experiments. The only way this problem may be saved is if an ion pressure term develops a strong gradient that smooths the region from where $\boldsymbol{J} \times \boldsymbol{B}$ reaches its peak to $r = R(t)$. The presence of the strong $\boldsymbol{J} \times \boldsymbol{B}$ force means that this is likely a kinetic term and probably anisotropic.

B.4—Estimating the Coupling

Using simply as an estimate the expansion form of V_r, the profiles for the induced field and electrostatic field are $f(x) = x^2$ and $g(x) = x$ if we assume a uniform density. Equation B.2 becomes

$$\Delta \boldsymbol{V} = 1.402 \frac{\omega_{ci}^{a}}{\omega_{ci}^{d}} V_{r0} \int_{R'(t')=r'}^{t'} dt' \left(-\alpha_{\phi} \partial_{t'} \left(\frac{1}{R'} \right) r'^{2} \hat{\phi} - \frac{3}{2} R' r' \hat{r} \right)$$

$$1.402 \frac{\omega_{ci}^{a}}{\omega_{ci}^{d}} V_{r0} \left(\alpha_{\phi} (r' - r'^{2}) \hat{\phi} - \frac{3}{2} r' \hat{r} \int_{R'(t')=r'}^{t'} dt' R' \right).$$

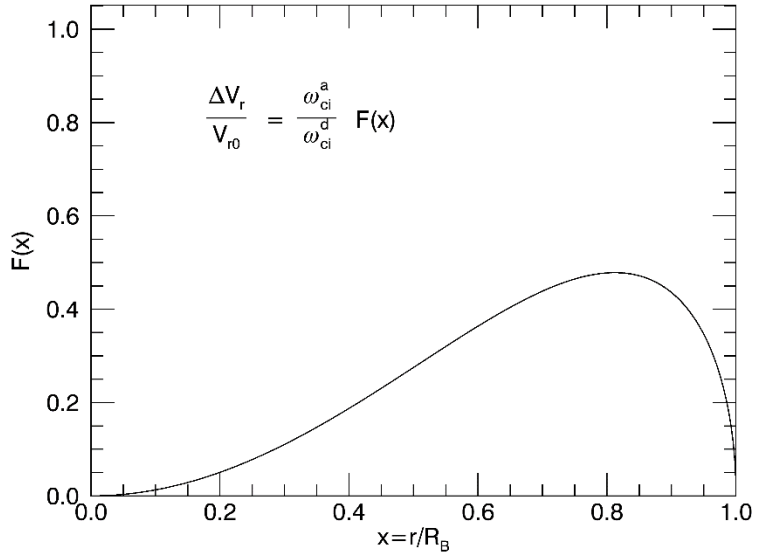

Figure B.2: Radial coupling function for calculating the impulse in the radial direction for a linear electrostatic field profile, $E_{st} \sim x$.

The function

$$F(x) = 1.402 \frac{3}{2} r' \int_{R'(t')=r'}^{1} dt' R',$$

which we'll call the radial coupling function, is plotted in Fig. B.2. For argon ions and $Z_d = 2$ carbon ions, the expected radial velocity is $V_r = -8 \times 10^5$ cm/s. But this value depends crucially on the linear form of the electrostatic potential profile. The fastest ions are near the front of the

expansion right where there is a problem with the expansion profile $V_r \propto r$. If the $\boldsymbol{J} \times \boldsymbol{B}$ force falls of as $r \to R_B$, then all of these ions will be moving slower due to a reduced electrostatic field. The value quoted above should only be taken as an extreme maximum or the characteristic size of the resulting velocity. A factor 2 error would not be unrealistic. The velocity from the azimuthal field is easy to calculate and is $V_\phi = 10^5$ cm/s for an expansion with $\omega_{ci}^d \tau_D = 0.3$. This is far smaller than the radial velocity under the same approximation and the case of a dominant electrostatic field will generally be true if $\omega_{ci}^d \tau_D < 1$.

For the energy coupled, we look at the integral in Eq. B.3 or B.4,

$$I(t') = \int_0^{R'} dr' r'^2 \left(\int_{R'(t')=r'}^{t'} dt' \boldsymbol{E}'(r', t') \right)^2 .$$

Since by design all the variables and the electric field are less than 1, $I(t') < 1 \forall t'$. This expression can be simplified by completely inverting the integrals. First, note that

$$\left(\int_a^b dx\, f(x) \right)^2 = 2 \int_a^b dx f(x) \int_a^x dx' f(x').$$

Then, note that the area integral

$$\int_0^{f(y)} dx \int_{f(y')=x}^{b} dy'$$

can be reversed to

$$\int_0^b dy' \int_0^{f(y')} dx$$

if $f(0) = 0$. Breaking up the integral into its azimuthal and radial contributions, $I = I_\phi + I_r$,

$$I_\phi(t') = \alpha_\phi^2 \int_0^{t'} du \partial_u R'(u) \int_0^u dv\, \partial_v R'(v) \int_0^{R'(v)} dr' r'^2 f\left(\frac{r'}{R'(v)}\right) f\left(\frac{r'}{R'(u)}\right)$$

and

$$I_r(t') = \frac{9}{4} \int_0^{t'} du R'^2(u) \int_0^u dv\, R'^2(v) \int_0^{R'(v)} dr' r'^2 g\left(\frac{r'}{R'(u)}\right) g\left(\frac{r'}{R'(v)}\right).$$

Inserting the expansion profiles

$$I_\phi(t') = \frac{\alpha_\phi^2}{5 \cdot 6 \cdot 7} R'^5(t') \ll 1 \text{ for } \omega_{ci}^d \tau_D < 1$$

and

$$I_r(t') = \frac{9}{4 \cdot 5} \int_0^{t'} du \int_0^u dv R'^5(v).$$

For $\omega_{ci}^d \tau_D = 0.3$, we have

$$I_\phi = 0.0001 \text{ and } I_r = 0.029.$$

For an argon plasma density of $n_i = 4 \times 10^{12}$, singly ionized in 750 G, and an LPP with 1.5×10^{15} doubly-ionized carbon ions, $R_q \sim 5$ cm. Using this value, and the above values, $E_c(\tau_D) =$ 0.5 mJ or $E_c/E_{tot} \sim 2 \times 10^{-3}$.

B.5—LPP Spin-up

In the foregoing conclusions, the possibility of the rotation of the LPP was excluded. Would the LPP begin to rotate as it expands, this would constitute an additional loss of momentum from the radial expansion of the diamagnetic cavity. This means our energy analysis would have to look like

$$E = \frac{C}{2} m_{di} N_{di} \left((\partial_t R)^2 + V_\phi^2(t) \right) + \frac{4\pi D}{3} (R^3 - R_0^3) \frac{B_0^2}{2\mu_0}.$$

The presence of an azimuthal rotation of the LPP would also mean that some of the electrostatic field in the radial direction is due to this rotational mass flow since $\boldsymbol{V} \times \boldsymbol{B}$ acquires a radial component. A simple argument, however, shows that for the LPPs of interest, this term can be ignored and the treatment of the LPP as rotationless is a good approximation.

For the assumed form of Ohm's law and isotropic pressures for the electrons and ions, p_e and p_i, momentum conservation is

$$\rho_m d_t \boldsymbol{V} = \rho_c \boldsymbol{E} + \boldsymbol{J} \times \boldsymbol{B} - \nabla(p_e + p_i)$$

and

$$\boldsymbol{E} = -\boldsymbol{V} \times \boldsymbol{B} + \frac{\boldsymbol{J} \times \boldsymbol{B}}{e n_e},$$

where $\rho_m = \sum m_\alpha n_\alpha$ and $\rho_c = \sum Z_\alpha n_\alpha$ are sums over all species in the system. These equations can be combined by eliminating $\boldsymbol{J} \times \boldsymbol{B}$ to get

$$\rho_m d_t \boldsymbol{V} = \rho_c \boldsymbol{E} + e n_e (\boldsymbol{E} + \boldsymbol{V} \times \boldsymbol{B}) - \nabla(p_e + p_i)$$

$$\rightarrow m_{di} n_i d_t \boldsymbol{V} = \langle Z \rangle e n_i \boldsymbol{E} + \langle Z \rangle e n_i \boldsymbol{V} \times \boldsymbol{B} - \nabla(p_e + p_i)$$

for $\rho_m \approx m_{di} n_i$ and $\langle Z \rangle = n_e / n_i$. If the pressure is only dependent on space through the density, e.g. in an ideal gas, and the temperature is constant or depends at most on time, then the momentum equation is identical to a single particle equation of motion with the associated Lagrangian

$$L = \frac{1}{2} m_{di} \boldsymbol{V}^2 + \langle Z \rangle e \left(\phi + \boldsymbol{V} \cdot \boldsymbol{A} + \frac{p_e}{e n_e} + \frac{p_i}{\langle Z \rangle e n_i} \right).$$

In cylindrical symmetry, the azimuthal momentum is conserved

$$m_i V_\phi + \langle Z \rangle e A_\phi = const.$$

Note that this is directly related to the conservation of circulation or vorticity [87] in Hall MHD where the quantity

$$\Gamma \equiv \oint_C d\ell \cdot (m_{di} \boldsymbol{V} + \langle Z \rangle e \boldsymbol{A})$$

is independent of time for a contour C that follows an element of fluid. Note that that result is far more general and applies to plasmas that lack azimuthal symmetry. The induced field in the expansion gives us at $r = R(t)$

$$-\partial_t A_\phi\big(r = R(t)\big) = \partial_t R(t) B\big(r = R(t)\big).$$

If we take $B\big(r = R(t)\big)$ as a constant, then

$$A_\phi = -R(t)B + D$$

where D is an arbitrary integration constant. If we take as an initial condition that the plasma is not spinning at R_0, then the azimuthal flow of the LPP is

$$V_\phi(t) = \frac{\langle Z \rangle B}{m_{di}} R(t),$$

or as a fraction of V_{r0},

$$\frac{V_\phi}{V_{r0}} = \frac{\langle Z \rangle B}{m_{di}} \frac{R(t)}{V_{r0}} \leq \frac{\langle Z \rangle B}{m_{di}} \frac{R_B}{V_{r0}} = \frac{\omega_{ci}^d \tau_D}{1.402},$$

which appeared before in the ratio of the characteristic strength of the induced field to that of the electrostatic field. This means that the regime in which the induced field is stronger than the

electrostatic field also corresponds to one in which the coupling to the diamagnetic cavity is reduced and the LPP ions will lose radial momentum to azimuthal spin-up.

Various term were neglected to get this result and so like other facets of the Rayleigh model, it should be taken only as a guide-line. Specifically, due to the large field gradients in the diamagnetic cavity, the ion pressure term is most certainly not isotropic. Furthermore, resistive effects are in the azimuthal direction as well as some portion of ion viscosity. These tend to reduce the spin-up of the LPP by reducing the induced electric field. The condition $\omega_{ci}^{d}\tau_D > 1$ only means that there is not a good reason to neglect the spin of the LPP. For the case presented in Chapter 4 and this dissertation, most of the lifetime of the cavity has $|\boldsymbol{E}_{ind}|/|\boldsymbol{E}_{st}|$ less than the predicted ratio $\omega_{di}^{d}\tau_D/1.402 \approx 0.2$.

REFERENCES

[1] Dawson, J.M., *Physics of Fluids* **7** (7), 981 (1964)

[2] Villeneuv, D.M., Enright, G.D., Burgess, M.D.J., Fedosejevs, R., and Richardson, M.C., *Physical Review Letters* **47** (7), 515 (1981)

[3] Macchi, A., Borghesi, M., and Passoni, M., *Reviews of Modern Physics* **85**, 751 (2013)

[4] Nuckolls, J., Wood, L., Thiessen, A., and Zimmerman, G., *Nature* **239**, 139 (1972)

[5] Singh, R.K. and Narayan, J., *Physical Review B* **41**, 8843 (1990)

[6] Niemann, C., Constantin, C.G., Everson, E.T., Schaeffer, D.B., Bondarenko, A.S., Clark, S.E., Winske, D., and Vincena, S., *Geophysical Research Letters* **41** (21), 7413 (2014)

[7] Lada, C.J., *Annual Reviews of Astronomy and Astrophysics* **23**, 267 (1985)

[8] Carrasco-Gonzalez, C., Rodrizque, L.F., Anglade, G., Marti, J., Torrelles, J.M., and Osorio, M., *Science* **330**, 1209 (2010)

[9] Brown, W.L., Hess, W.N., and Van Allen, J.A., *Journal of Geophysical Research* **92**, 5777 (1963)

[10] Allen, J.A., Spatial Distribution and Time Decay of the Intensities of Geomagnetically Trapped Electrons from the High Altitude Nuclear Burst of July 1962. In McCormac, B.M. (Ed.), *Radiation Trapped in the Earth's Magnetic Field* New York: Gordon and Breach (1965)

[11] Bernhardt, P.A., Roussel-Dupre, R.A., and Pongratz, M.B. *Journal of Geophysical Research* **92** (A6), 57777 (1987)

[12] Huba, J.D., Bernhardt, P.A., and Lyon, J.G., *Journal of Geophysical Research* **97** (A1), 11 (1992)

[13] Puell, H., *Zeitschrift für Naturforschung A* **25**, 1807 (1970)

[14] Nemchinov, I.V., *Journal of Applied Mathematics and Mechanics* **29** (1), 134 (1965)

[15] Rosenbluth, M.N., Rosenbluth, A., and Garwin, R., *Plasma Physics and Thermonuclear Research* **2**, 271 (1963)

[16] Chapman, S. and Ferraro, V.C.A., *Terrestrial Magnetism and Atmospheric Electricity* **45** (3), 245 (1940)

[17] Ferraro, V.C.A., *Journal of Geophysical Research* **57** (1), 15 (1952)

[18] Dungey, J.W., *Cosmic Electrodynamics*. London: Cambridge University Press (1958)

[19] Harris, E.G., *Il Nuovo Cimento* **23** (1), 115 (1962)

[20] Raizer, Y.P., *Zhurnal Prikladnoy Mekhaniki I Teknicheskoy* **6**, 19 (1963)

[21] Colgate, S.A., *Journal of Geophysical Research* **70** (13), 3161 (1965)

[22] Sudo, S., Sato, K.N., and Sekiguchi, T. *Journal of Physics D: Applied Physics* **11** (3), 389 (1978)

[23] Rayleigh, L. *Philosophical Magazine, Series 6* **34** (200), 94 (1917)

[24] Fadre, W.J., *Physics of Fluids* **11**, 2200 (1968)

[25] Ripin, B.H., Huba, J.D., McLean, E.A., Manka, C.K., Peyser, T., and Burris, H.R., *Physics of Fluids B* **5** (10), 3491 (1993)

[26] Barenblatt, G.I., *Scaling, Self-similarity, and Intermediate Asymptotics*, London: Cambridge University Press (1996)

[27] Fabre, E., Stenz, C., and Colburn, S., *Journal de Physique* **34** (4), 323 (1973)

[28] Haught, A.F., Polk, D.H., and Fader, W.J., *Physics of Fluids* **13**, 2825 (1970)

[29] Van Zeeland, M. and Gekelman, W. *Physics of Plasmas* **11**, 320 (2004)

[30] Dimonte, G. and Wiley, L.G., *Physical Review Letters* **67** (13), 1755 (1991)

[31] Collette, A. *Structure of an Expanding Laser-Produced Plasma* (Doctoral dissertation), (2010)

[32] Gekelman, W. *et al, Review of Scientific Instruments* **67**, 025105 (2016)

[33] Leneman, D., Gekelman, W., and Maggs, J. *Review of Scientific Instruments* **77**, 015108 (2006)

[34] Van Zeeland, M., Gekelman, W., Vincena, S., and Dimonte, G., *Physical Review Letters* **87**, 105001 (2001)

[35] Grun, J., Decoste, R., Ripin, B.H., and Gardner, J., *Applied Physics Letters* **39** (7), 545 (1981)

[36] Grun, J., Obenschain, S.P., Ripin, B.H., Whitlock, R.R., McLean, E.A., Gardner, J., Herbst, M.J., and Stamper, J.A., *Physics of Fluids* **26** (2), 588 (1983)

[37] Meyer, B., and Thiell, G., *Physics of Fluids* **27**, 302 (1984)

[38] Forslund, D.W., Kindel, J.M., Lee, K., Lindman, E.L., and Morse, R.L., *Physical Review A* **11**, 679 (1975)

[39] Puell, H., Neusser, H.J., and Kaiser, W. *Zeitschrift für Naturforschung A* **25**, 1815 (1970)

[40] McWhirter, R.W.P., Spectral Intensities. In Huddlestone, R.H. and Leonard, S.L. (Ed.), *Plasma Diagnostic Techniques* New York: Academic Press (1965)

[41] Opower, H. and Press, W., *Zeitschrift für Naturforschung A* **21**, 344 (1966)

[42] Griem, H.R. *Plasma Spectroscopy* London: Cambridge University Press (2005)

[43] Karmida, A., Ralchenko, Yu., Reader, J., and NIST ASD Team. *NIST Atomic Spectra Database* (ver. 5.3) [ONLINE]. Available: http://physics.nist.gov/asd. National Institute of Standards and Technology, Gaithersburg, MD.

[44] Hobbs, G.D. and Wesson, J.A., *Plasma Physics* **9**, 85 (1967)

[45] Takamura, S., Ohno, N., Ye, M.Y., and Kuwabara, T., *Contributions to Plasma Physics* **44** (1), 126 (2004)

[46] Wang, X., Pilewskie, J., Hsu, H.-W., and Horanyi, M., *Geophysical Research Letters* **43** (2), 525 (2016)

[47] Sheehan, J.P. and Hershkowitz, N., *Plasma Sources Scient and Technology* **20**, 063001 (2011)

[48] Martin, M.J., Bonde, J., Gekelman, W., and Pribyl, P., *Review of Scientific Instruments* **86**, 053507 (2015)

[49] Varga, P., Hofer, W., and Winter, H., *Journal of Physics B: Atomic and Molecular Physics* **14**, 1341 (1981)

[50] Hagstrum, H.D. *Physical Review* **104** (2), 302 (1956)

[51] Goeckner, M.J., Goree, J., and Sheridan, T.E., *Physics of Fluids B* **3** (10), 2913 (1991)

[52] Krall, N.A. and Trivelpiece, A.W., *Principles of Plasma Physics*. New York: McGraw-Hill (1973)

[53] Rumsby, P.T. and Paul, J.W.M., *Plasma Physics* **16**, 247 (1974)

[54] Van Zeeland, M., Gekelman, W., Vincena, S., and Maggs, J. *Physics of Plasmas* **10** (5), 1243 (2003)

[55] Collette, A. and Gekelman, W., *Physical Review Letters* **105**, 195003 (2010)

[56] Collette, A. and Gekelman, W., *Physics of Plasmas* **18**, 055705 (2011)

[57] Koopman, D.W., *Physics of Fluids* **19**, 670 (1976)

[58] Zakharov, Y.P., Orishich, A.M., Ponomarenko, A.G., and Posukh, V.G., *Soviet Journal of Plasma Physics* **12** (10), 674 (1987)

[59] Longmire, C.L., *Notes on Debris-Air-Magnetic Interaction*. (RM-3386-PR) Santa Monica, CA: RAND Corporation (1963)

[60] Golubev, A.I., Solev'ev, A.A., and Terekhin, V.A., *Journal of Applied Mechanics and Technical Physics* **19** (5), 602 (1978)

[61] Bashurin, V.P., Golubev, A.I., and Terekhin, V.A., *Journal of Applied Mechanics and Technical Physics* **24** (5), 614 (1983)

[62] Hewett, D.W., Brecht, S.H., and Larson, D.J., *Journal of Geophysical Research* **116**, A11310 (2011)

[63] Clark, S.E., Winske, D., Schaeffer, D.B., Everson, E.T., Bondarenko, A.S., Constantin, C.G., and Niemann, C., *Physics of Plasmas* **20**, 082129 (2013)

[64] Plechaty, C. Presura, R., and Esaulov, A.A., Physical Review Letters **111**, 185002 (2013)

[65] Kasperczuk, A. and Pisarczyk, T., *Physica Scripta* **53**, 503 (1996)

[66] Pisarzyk, T. Farynski, A., Fiedorowicz, H., Gogolewski, P., Kusnierz, M., Makowski, J., Miklaszewski, R., Mroczkowski, M., Parys, P., and Szczurek, M. *Laser and Particle Beams* **10** (4), 767 (1992)

[67] Winske, D. and Gary, S.P., *Journal of Geophysical Research* **112**, A10303 (2007)

[68] Vincena, S.T., Gekelman, W., Van Zeeland, M.A., Maggs, J., and Collette, A., *Physics of Plasmas* **15**, 072114 (2008)

[69] Niemann, C. *et al*. *Physics of Plasmas* **20**, 012108 (2013)

[70] Mozer, F.S., Agapitov, O.A., Artemyev, A., Drake, J.F., Krasnoselskikh, V., Lejosne, S., and Vasko, I., *Geophysical Research Letters* **42** (10), 3627 (2015)

[71] Bostick, W.H., *Physical Review* **106**, 404

[72] Borovsky, J.E., *Physics of Fluids* **30** (8), 2518

[73] Brenning, N., Hurtig, T., and Raadu, M.A., *Physics of Plasmas* **12**, 012309

[74] Shaikhislamov, I.F., Zakharov, Yu. P., Posukh, V.G., Melekhov, A.V., Boyarintsev, E.L., Ponomarenko, A.G., and Terekhin, V.A., *Plasma Physics Reports* **20**, 102104

[75] Tidman, D.A. and Krall, N.A., *Shock Waves in Collisionless Plasmas*. New York: Wiley (1971)

[76] Keller, J.B. and Kolodner, I.I., *Journal of Applied Physics* **27**, 1152 (1956)

[77] Bhadra, D., *Physics of Fluids* **11** (1), 234 (1968)

[78] Tuckfield, R. and Schwirzke, F., *Plasma Physics* **11**, 11 (1969)

[79] Puell, H., Spengler, W., and Kaiser, W., *Physics Letters A* **37** (1), 35 (1971)

[80] Boland, B.C., Irons, F.E., and McWhirter, R.W.P., *Journal of Physics B* **1**, 1180 (1968)

[81] Hinnov, E. and Hirschberg, J.G., *Physical Review* **125** (3), 795 (1962)

[82] Pitaevskii, L.P., *Journal of Experimental and Theoretical Physics* **15** (5), 1326 (1962)

[83] Zel'dovich, Ya.B. and Raizer, Yu.P., *Physics of Shock Waves and High-Temperature Hydrodynamic Phenomena*. Mineola, New York: Dover (2002)

[84] Roudskoy, I.V., *Laser and Particle Beams* **14** (3), 369 (1996)

[85] O'Neil, T. and Fowler, T.K., *Physics of Fluids* **8**, 2255 (1965)

[86] Poukey, J.W., *Physics of Fluids* **12**, 1452 (1969)

[87] Banks, P.M., Edwards, W.F., Rasmussen, C., and Thompson, R.C., *Geophysical Research Letters* **8** (1), 95 (1981)